creative commons
COMMONS DEED

저작자표시-비영리-변경금지 2.0 대한민국

이용자는 아래의 조건을 따르는 경우에 한하여 자유롭게

- 이 저작물을 복제, 배포, 전송, 전시, 공연 및 방송할 수 있습니다.

다음과 같은 조건을 따라야 합니다:

저작자표시. 귀하는 원저작자를 표시하여야 합니다.

비영리. 귀하는 이 저작물을 영리 목적으로 이용할 수 없습니다.

변경금지. 귀하는 이 저작물을 개작, 변형 또는 가공할 수 없습니다.

- 귀하는, 이 저작물의 재이용이나 배포의 경우, 이 저작물에 적용된 이용허락조건을 명확하게 나타내어야 합니다.
- 저작권자로부터 별도의 허가를 받으면 이러한 조건들은 적용되지 않습니다.

저작권법에 따른 이용자의 권리는 위의 내용에 의하여 영향을 받지 않습니다.

이것은 이용허락규약(Legal Code)을 이해하기 쉽게 요약한 것입니다.

Disclaimer

dCollection

Doctor of Philosophy

MANUFACTURING PROCESSES ASSISTED BY ATHERMAL EFFECT OF ELECTRIC CURRENT: RAPID HEAT TREATMENT AND SOLID STATE JOINING

울산대학교
UNIVERSITY OF ULSAN

The Graduate School of the University of Ulsan

School of Mechanical Engineering

Shengwei Zhang

June 2022

MANUFACTURING PROCESSES ASSISTED BY ATHERMAL EFFECT OF ELECTRIC CURRENT: RAPID HEAT TREATMENT AND SOLID STATE JOINING

Advisor: **Sung-Tae Hong**

A Dissertation

Submitted to the Graduate School of the University of Ulsan

in Partial Fulfillment of the Requirements

for the Degree of

Doctor of Philosophy

by

Shengwei Zhang

School of Mechanical Engineering

University of Ulsan, Korea

June 2022

MANUFACTURING PROCESSES ASSISTED BY ATHERMAL EFFECT OF ELECTRIC CURRENT: RAPID HEAT TREATMENT AND SOLID STATE JOINING

This certifies that the dissertation of

Shengwei Zhang is approved by

Committee Chairman:	Prof. Doo-Man Chun	
Committee Member:	Prof. Sung-Tae Hong	
Committee Member:	Prof. Koo-Hyun Chung	
Committee Member:	Prof. Young-Tae Cho	
Committee Member:	Dr. Moon-Jo Kim	

School of Mechanical Engineering

University of Ulsan, Korea

June 2022

Shengwei Zhang 의

공학박사 학위 논문을 인준함

심사위원	천두만	
심사위원	홍성태	
심사위원	정구현	
심사위원	조영태	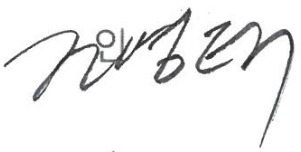
심사위원	김문조	

울 산 대 학 교 대 학 원

기계자동차공학과

2022 년 06월

Shengwei Zhang

© _____ 2022

All Rights Reserved

ABSTRACT

Recently, electric pulse has been used in electrically assisted manufacturing (EAM) due to its processing efficiency by a combined effect of rapid resistance heating and athermal effect (electroplasticity) of the electric current. During electropulsing treatment or electrically assisted (EA) heat treatment, in addition to the well-known thermal effect by resistance heating, the athermal effect of electric current can additionally weaken the atomic bonding by inducing a charge imbalance near defects. Consequently, the annealing, recrystallization, and aging during electropulsing treatment can be significantly enhanced in comparison to conventional furnace heat treatment. Therefore, electric pulse is widely used in altering the mechanical behavior of the metallic materials and various manufacturing applications such as electrically assisted pressure joining (EAPJ), EA assisted rapid annealing, EA assisted crack healing, and EA assisted residual stress release etc. In this dissertation, the EA assisted rapid heat treatment and EA assisted fatigue damage healing of the aluminum clad steel and the EAPJ of various metal alloys are systematically investigated.

First, laminated metal sheets, aluminum clad steel (ACS), are heat treated by electrically assisted rapid heat treatment (subsecond duration) to rapidly enhance the formability of the ACS sheet while adjusting the intermetallic evolution. The effect of the electric current density on the intermetallic evolution and mechanical properties was experimentally evaluated by scanning electron microscope (SEM) and tensile test, respectively. The present study proves that the electrically assisted rapid heat treatment is an efficient method to balance the strength and formability of the ACS sheet.

Next, the fatigue damage evolution and EA assisted prolonged fatigue life of the ACS sheet are systematically investigated by characterizing the microstructural change at different fatigue cycles. The results show that the pile-up of geometrically necessary dislocations (GNDs) due to the incompatible deformation at the interface between the steel substrate and the Al clad layers significantly improves the mechanical properties of the ACS sheet in the monotonic tension test. However, cracks are prone to initiate at Al grains of the interface and propagate toward the Al side in the fatigue test due to a preferred accumulation of GNDs in the soft Al grains near the interface. Particularly, the fatigue life was significantly prolonged by electropulsing treatment with only a subsecond duration, which is resulted from the diminished density of piled GNDs and the retardation of microcrack formation at the interface. The present study elucidates the failure mechanism of ACS and proves that electropulsing treatment is an efficient method to prolong the fatigue life of laminated metal composites by healing the accumulated damage during the fatigue test.

Finally, solid-state joints of various combinations of dissimilar metal alloys, S45C and Al661-T6, additively manufactured AMMS1 and conventional SUS410, and SUS316L and SUS410, are successfully fabricated by EAPJ technique. Lap joining of dissimilar steel S45C and aluminum 6061-T6 alloy sheets in the solid state is conducted by means of EAPJ. Moreover, for the material combination of SUS316L and SUS410, the fatigue behavior of the joints is evaluated by a P-S-N curve using two-parameter Weibull distribution. For the joining of additively manufactured maraging steel and conventional SUS410, the base sample of additively manufactured cylindrical maraging steel specimen is fabricated to have a porous layer on the joining end, while another end is printed as a perfectly solid matrix. The porous layer significantly increases the maximum joining temperature by the locally increased

electrical resistance and dramatically enhances the interfacial diffusion thickness. The effect of the porous layer on the microstructural evolution and mechanical properties is characterized by the electron back-scatter diffraction and quasi-static tensile test, respectively. The present study demonstrates that EAPJ is an efficient method in bulk and lap joining of dissimilar metal alloys combinations.

ACKNOWLEDGMENTS

First, I would like to express the most profound appreciation to my advisor, Professor Sung-Tae Hong, for his guidance, encouragement, suggestion, and very constructive criticism, which have contributed immensely to the evolution of my ideas on the papers and project work. Professor Sung-Tae Hong taught me how to think carefully and deeply in research to touch the level of a doctor. From my heart, he is an important person who gives me a chance to study abroad and conquer my dream. Without his support and guidance, this dissertation would not have been possible to compete on time.

I particularly want to thank Professor Heung Nam Han and his students in Seoul national university for their help and valuable discussions during my studies. Also, it is my pleasure to collaborate with Dr. Moon-Jo Kim from Korea Institute of Industrial Technology and Professor Hoon-Hwe Cho from Hanbat National University for a very valuable distribution of our papers. I wish to express my appreciation to all colleagues in the Advanced Engineering Materials Lab for their help on my research and experiments. I also thank all those who have helped me in one way or another during my Ph. D period.

Finally, I am incredibly grateful to my parents for their continuous encouragement, understanding and support.

Shengwei Zhang

TABLE OF CONTENT

ABSTRACT …… i

ACKNOWLEDGMENTS ……... iv

TABLE OF CONTENTS ……... v

LIST OF FIGURES …… viii

LIST OF TABLES ……... xv

CHAPTER I INTRODUCTION……... 1

References …… 7

CHAPTER II EFFECTS OF INTERMETALLIC EVOLUTION BY ELECTRICALLY ASSISTED RAPID HEAT TREATMENT ON THE MECHANICAL PERFORMANCE AND FORMABILITY OF ALUMINUM CLAD STEEL ……. 10

2.1 Introduction ..…….. 11

2.2 Experimental set-up ...……. 13

2.3 Results and discussion ..……... 17

2.4 Conclusions ….…… 32

References ..…….. 33

CHAPTER III PROLONGED FATIGUE LIFE IN ALUMINUM CLAD STEEL BY ELECTROPULSING TREATMENT: RETARDATION OF INTERFACE-MICROCRACK FORMATION……... 38

3.1 Introduction ..…….. 38

3.2 Experimental set-up ...……. 41

3.3 Results ..……..……... 45

3.4 Discussion ..…….…... 58

3.5 Conclusion ….…… 61

References ..……...…….. 62

CHAPTER IV ELECTRICALLY ASSISTED SOLID STATE LAP JOINING OF DISSIMILAR STEEL S45C AND ALUMINUM 6061-T6 ALLOY…..... 65

4.1 Introduction ..……...…….. 65

4.2 Experimental set-up ...……...……. 68

4.3 Results and discussion ..……..……... 72

4.4 Conclusion ….…… 85

References ..……...…….. 86

CHAPTER V EFFECTIVENESS OF AN ADDITIVELY MANUFACTURED POROUS LAYER IN DISSIMILAR SOLID-STATE BULK JOINING OF ADDITIVELY MANUFACTURED MARAGING STEEL AND CONVENTIONAL AISI410 STEEL…….. 91

5.1 Introduction ..……..... 91

5.2 Experimental set-up ...……..……. 94

5.3 Results and discussion ..……... 100

5.4 Conclusion ….……..…… 112

References ..…….…….. 114

CHAPTER VI MICROSTRUCTURE EVOLUTION AND FATIGU PERFORMANCE OF DISSIMILAR SOLID-STATE JOINTS OF SUS316L AND SUS410…….…….. 120

6.1 Introduction ..…….….. 120

6.2 Experimental set-up ...…….....…….…. 123

6.3 Results and discussion ..……... 129

6.4 Conclusions ….…….…….....…… 148

References ..…….…….. 149

CHAPTER VII CONCLUSIONS ……....…….…….…. 154

LIST OF FIGURES

Figure 2.1 Schematics of the experimental set-up: (a) manufacturing process of the aluminum clad steel sheet and (b) electrically assisted rapid heat treatment and subsequent mechanical testing 15

Fig. 2.2. Temperature histories during electrically assisted rapid heat treatment: (a) single pulse treatment and (b) four pulses treatment 20

Fig. 2.3. EBSD IPF maps: (a) BM-ACS sample and (b) 190-I sample 20

Fig. 2.4. SEM images and EDS line scan of the major elements: (a) BM sample, (b) 170-I sample, (c) 170-IV sample, and (d) 190-I sample 20

Fig. 2.5. Microhardness changes with the current density for all single pulsed samples 22

Fig. 2.6. Tensile test results of the single pulse treatment: (a) true stress-strain curves, (b) the change of yield strength and elongation with the current densities, (c) fracture appearance, and (d) the change of work hardening exponent with the current densities 24

Fig. 2.7. Comparison between single pulse and four pulses treatment for representative current densities of 150 A/mm^2 and 170 A/mm^2: (a) true stress-strain curves, (b) the change of yield strength and elongation with the current densities, (c) fracture appearance, and (d) the change of work hardening exponent with the current densities 25

Fig. 2.8. Strain distribution observed by DIC during tensile test: (a) BM sample, (b) 170-I sample, and (c) 190-I sample 26

Fig. 2.9. OM images: (a) BM sample, (b) 170-I sample, and (c) 190-I sample along loading direction; SEM images: (d) BM sample, (e) 170-I sample, and (f) 190-I sample perpendicular to the loading direction 28

Fig. 2.10. Schematics of the fracture mechanism: (a) matrix-dominated fracture and (b) interfacial IMC-dominated fracture 31

Fig. 2.11. U-shape forming tests: (a) BM sample, (b) 170-I sample, and (c) 170-IV sample 31

Fig. 3.1. Experimental process of the fatigue life enhancement 44

Fig. 3.2. Dimensions of the samples for (a) monotonic tension and (b) fatigue..... 45

Fig. 3.3. Microstructural observation of the BM ACS: (a) SEM morphology, (b) IPF map and the relevant grain size distribution, and (c) EDS-line scan across the interface 48

Fig. 3.4. Monotonic tensile results of the BM ACS: (a) tensile stress-strain curve, (b) loading-unloading-reloading curve, (c) the calculated back stress, and (d) strain distribution by DIC test 50

Fig. 3.5. Discrete fatigue life at different stress levels 52

Fig. 3.6. The fatigue failure process for maximum stress of 245 MPa: (a) SEM image of interface along the loading direction at different fatigue ratios and (b) fracture surface perpendicular to the loading direction 53

Fig. 3.7. The evolution of the EBSD results for maximum stress of 245 MPa: (a) IPF and KAM maps, (b) the averaged KAM value for entire observational area, and (c) the averaged KAM value for each constituent layer. RD indicates rolling direction; ND indicates normal direction 55

Fig. 3.8. The evolution of the EBSD results for maximum stress of 245 MPa: (a) IQ maps overlaid with grain boundaries and (b-e) histograms of misorientation angles ……..... 56

Fig. 3.9. Enhancement of the fatigue life by electropulsing treatment: (a) temperature histories during the application of the electric pulse and (b) enhanced fatigue life compared with the corresponded original fatigue life 57

Fig. 3.10. Microhardness change for samples of BM, 250,000 cycles, and 250,000 cycles with electropulsing treatment under σ_{max}=245 MPa and R=0.1 ……. 58

Fig. 3.11. Microstructural change before and after electropulsing treatment: (a) IPF map, (b) KAM map, and (c) IQ map overlaid with grain boundaries before electropulsing treatment; (d) IPF map, (e) KAM map, and (f) IQ map overlaid with grain boundaries after electropulsing treatment. RD indicates rolling direction; ND indicates normal direction 59

Fig. 4.1. Configuration of the joint ……..... 73

Fig. 4.2. Schematic of the experimental set-up ……..... 73

Fig. 4.3. Schematic of electric current and displacement histories during EAPJ. (a) EAPJ without additional holding time, (b) EAPJ with additional holding time ……..... 74

Fig. 4.4. Schematic of lap shear tensile test ……..... 76

Fig. 4.5. Process responses during EAPJ: (a) temperature histories of G-I group; (b) compressive loads of G-I group; (c) temperature histories of G-II group; (d) compressive loads of G-II group ……..... 78

Fig. 4.6. EAPJ lap joints of S45C and Al6061-T6 ……..... 78

Fig. 4.7. Optical microscopy image of typical cross section ……..... 78

Fig. 4.8. Failure mode of the joints during quasi-static lap shear tensile test: (a) shear fracture, (b) tensile fracture ……..... 79

Fig. 4.9. Fracture load of quasi-static lap shear tensile tests ……..... 80

Fig. 4.10. EAPJ joints fabricated by small electrode ……..... 82

Fig. 4.11. Shear strength as a function of current density ……..... 82

Fig. 4.12. SEM images and EDS line scan of the S45C/Al6061-T6 joints; (a) G-I-60 joint; (b) G-II-80 joint ……..... 84

Fig. 4.13. EDS elemental mapping of G-II-80 joint ……..... 84

Fig. 4.14. (a) and (b) EBSD inverse polar figure (IPF) ND maps and Kernel average misorientation (KAM) maps of Al and steel BMs. The different colors in IPF maps indicate the orientation of each grain with respect to ND ……..... 86

Fig. 4.15. EBSD IPF ND maps for G-I and G-II joints with various nominal electric current densities (60, 65, 75, and 80 A/mm^2) ……..... 87

Fig. 4.16. Microhardness profiles of the joints across the interface: (a) G-I group; (b) G-II group ……..... 88

Fig. 4.17. Fracture morphology of G-I-60 and G-II-80 joints ……..... 88

Fig. 5.1. Schematics of EAPJ: without porous layer (top) and with porous layer (bottom) ……..... 102

Fig. 5.2. The electric current and displacement during EAPJ ……..... 104

Fig. 5.3. Process response during EAPJ: (a) temperature histories and (b) compressive load histories; temperature distribution along the axial direction for (c) the NPL joint and (d) the PL joint ……..... 107

Fig. 5.4. The appearance of the joints: (a) NPL joint and (b) PL joint ……..... 108

Fig. 5.5. Optical micrographs of the AM-MS1/AISI410 interface for (a) the NPL joint and (b) the PL joint; SEM images of the interface and its relevant EDS mapping of the major elements for (c) the NPL joint and (d) the PL joint ……..... 109

Fig. 5.6. EDS line scan analysis with a length of 4.5 μm for major elements traces: (a) NPL joint and (b) PL joint ……..... 110

Fig. 5.7. EBSD IPF maps and the grain size: (a) the AISI410 BM, (b) the AM-MS1 BM, (c) each side for the NPL joint, and (d) each side for the PL joint (JD-joining direction; TD-transverse direction; ND-normal direction) ……..... 112

Fig. 5.8. IQ maps overlaid with grain boundaries: (a) the BMs, (b) the NPL joint, and (c) the PL joint; KAM maps: (d) the BMs, (e) the NPL joint, and (f) the PL joint (the fractions of HAGBs and LAGBs are given in IQ maps; the average KAM values are given in KAM maps) ……..... 113

Fig. 5.9. GAIQ maps and relevant distributions of area fraction: (a) the AISI410 BM, (b) the NPL joint, (c) the AM-MS1 BM, and (d) the PL joint ……..... 115

Fig. 5.10. Microhardness profiles across the interface (measurement distance of 400 μm) ……...……. 116

Fig. 5.11. Engineering stress-strain curves and the fracture appearance of the joints.... 118

Fig. 5.12. Fracture surface of the representative joint (PL joint) ……..... 118

Fig. 6.1. Schematic of EAPJ experiment ……..... 131

Fig. 6.2. Schematic of electric current and displacement histories during EAPJ …..... 133

Fig. 6.3. Dimension of the specimen for quasi-static tensile test ……..... 134

Fig. 6.4. Dimension of the specimen for fatigue test ……..... 134

Fig. 6.5. Process response during EAPJ: (a) temperature histories and (b) load histories…….…. 139

Fig. 6.6. The appearance of the EAPJ joints ……..... 139

Fig. 6.7. The cross section and OM images of each joint ……..... 140

Fig. 6.8. The backscatter electron (BSE) images and results of EDS line scan across the interface ……..... 141

Fig. 6.9. EBSD IPF and GOS maps of both BMs and EAPJ joints: (a) IPF maps of the BMs; (b) GOS maps of the BMs; (c) IPF maps of the EAPJ joints; (d) GOS maps of the EAPJ joints. The blue and red color in the GOS maps indicate the recrystallized and unrecrystallized grains, respectively ……..... 142

Fig. 6.10. The grain size change with the nominal electric current density ……..... 143

Fig. 6.11. IQ (overlaid with grain boundaries) maps and KAM maps of BMs and EAPJ joints: (a) IQ maps of the BMs; (b) KAM maps of the BMs; (c) IQ maps of the EAPJ joints; (d) KAM maps of the EAPJ joints ……..... 145

Fig. 6.12. Grain average image quality (GAIQ) maps and relevant distribution of area fraction for the BMs and EAPJ joints ……..... 146

Fig. 6.13. Microhardness profiles of the EAPJ joints across the interface …..... 148

Fig. 6.14. Quasi-static tensile results of the EAPJ joints ……..... 149

Fig. 6.15. The fatigue life obtained from experiments at different stress levels …..... 151

Fig. 6.16. Fatigue results at different stress levels: (a) 600 MPa; (b) 580 MPa; (c) 567 MPa; (d) 540 MPa ……..... 151

Fig. 6.17. Weibull plots for different maximum cyclic stress ……..... 152

Fig. 6.18. S-N curves with different reliability levels ……..... 153

Fig. 6.19. Fracture appearance of the failed specimen under 600 MPa …..... 154

Fig. 6.20. Fracture appearance of the failed specimen under 567 MPa ……..... 155

LIST OF TABLES

Table 2.1. Chemical compositions of the raw materials (wt%) …..... 15

Table 2.2. Process parameters during electrically assisted rapid heat treatment 16

Table 2.3. Phase constituents of the IMC layer 21

Table 3.1. Chemical compositions of the raw materials (wt%) 44

Table 4.1. The nominal chemical compositions of S45C and Al6061-T6 (in wt%) 73

Table 4.2. Experimental parameter matrix 75

Table 4.3. Chemical composition of locations in Fig. 4.12 85

Table 5.1. Chemical compositions of the materials (wt%) 100

Table 5.2. SLM AM process parameters 101

Table 5.3. EAPJ process parameters 104

Table 5.4. Chemical compositions of points A and B (wt%) 111

Table 6.1. Chemical compositions of the materials (in wt%) 131

Table 6.2. Mechanical properties of the materials 132

Table 6.3. Joining parameters of EAPJ 133

Table 6.4. The results of fatigue tests for J-32 joint 150

Table 6.5. Weibull parameters, MTTF, and CV for each stress level 152

CHAPTER I

INTRODUCTION

There is an increasing interest in electrically assisted manufacturing (EAM), because the electric current is expected to effectively enhance the formability of metallic materials during deformation [1]. The phenomenon of electric current on the changing of the material behavior was first reported by Machin et al. [2] in 1959. According to Machlin, applying an electric current affects flow stress, ductility, and yield strength of brittle rock salt. Besides, Roth et al. [3] reported studies that achieved nearly 400% tensile elongation of aluminum 5754 alloys. Regarding rolling, Zhang et al. [4] reported that twins in the microstructure of a rolled AZ91 magnesium alloy were eliminated and a homogeneous fine grain structure was achieved by dynamic electropulsing. Also, Yu et al. [5] reported microstructure refinement in electropulse induced cold-rolled medium carbon low alloy steels. Kim et al. [6] analyzed the microstructure changes after applying electric current during uniaxial tension and found that the electric current itself, rather than the Joule heating effect, was the dominant reason for annealing. Moreover, many studies have reported that the changes in the microstructure of materials could be controlled and accelerated by applying electric current with high density to the material without deformation [7-12].

During the application of the electric current, a combined effect of rapid resistance heating and athermal effect (electroplasticity) of the electric current drastically affects the material properties such as yield stress, flow stress, and elongation. When the athermal effect of electric current during deformation has prominence over the thermal effect, the effect is called “electroplasticity”. The electroplasticity is often demonstrated by that the elongation

increases drastically during deformation under electric current without a significant elevation of temperature due to Joule heating [13]. Kim et al. [14] reported the mechanism of the electroplasticity by concluding that the electric current can additionally weaken the atomic bonding by inducing a charge imbalance near defects. Therefore, the annealing [15], recrystallization [16], and aging [17] during electropulsing treatment can be significantly enhanced in comparison to conventional furnace heat treatment. Furthermore, for the conventional process, it needs a long time to heat up the furnace and materials with additional excess energy to maintain the temperature of the furnace and mold, while the electric current can rapidly heat the materials at a sub-second level. Thus, the common problems of the conventional process, such as thermal stress, warp, and low controllability of tolerance can be minimized. So, the EAM is a cost-effective and energy-saving manufacturing process, which also enhances the quality of products.

In addition to the electrically assisted (EA) enhanced ductility of the metal alloys, the healing of fatigue-induced damage by the electric pulse is also an interesting concept in achieving infinite serving of the components. Several researchers reported that the electric pulse is an effective method to restore the microstructural damage and close the initiated microcracks, even though the suggested healing mechanisms of fatigue-induced damage were slightly different depending on the experimental conditions. Tang et al. [18] investigated the restoration of the fatigue damage in stainless steel by high-density electric current. They concluded that the delayed fatigue crack initiation was the result of a decrease in the dislocation density, which was characterized by transmission electron microscopy. Jung et al. [19] attributed the delay of crack propagation to the crack-shielding effect resulting from current-induced local melting. Yang et al. [20] found that selective heating and thermal

compressive stress around the cracks led to void healing when an electric pulse was applied to damaged samples. Although several researchers have reported prolonged fatigue life resulting from the reduced dislocation density and the closed cracks through electropulsing treatment for homogeneous metal alloys, the healing mechanism of multi-layer materials by electropulsing treatment has rarely been reported. In comparison with homogeneous metal alloys, the fatigue damage evolution of multi-layer materials can be much more complicated due to the stress redistribution and the strain transfer between different layers during the test. Therefore, investigating the fatigue damage evolution of laminated metal sheets and the healing mechanism by electropulsing treatment can be crucial for engineering applications of multi-layer materials.

Electrically assisted pressure joining (EAPJ), as a part of EAM and pressure joining techniques, utilizes resistance heating to join two similar or dissimilar materials in solid state without melting or solidification. In this method, electric current is applied to a specimen assembly under continuously compressive plastic deformation, which enhances the interfacial diffusion by a combination of high pressure and the EA enhanced atomic mobility. Also, in comparison to conventional pressure joining, EAPJ has several technical advantages. The workpieces can be heated rapidly and locally. As a result, the process time can be reduced and unnecessary thermal effects on the workpiece can be minimized. Also, the joining apparatus can be significantly simpler and cost-effective due to the need for a heating furnace is eliminated. Xu et al. [21] investigated the feasibility of joining stainless steel (SUS) 316 foils having different thicknesses by means of electrically assisted solid state pressure welding. Their results show that SUS316 sheets could not be joined at room temperature but could be successfully joined by applying an electric current density of 6.7 A/mm^2. They studied the

effects of various current densities upon joint strength and concluded that not only the resistance heating but also the athermal effect of electric current contributed to the success of joining. Also, Li et al. [22] successfully joined titanium alloy sheets in a lap configuration by means of EAPJ. In addition, Li et al. [23] demonstrated that EAPJ could be easily implemented in dissimilar joining by successfully joining dissimilar SUS316L and Inconel 718 alloys in a cylinder shape. Jo et al. [24] applied EAPJ to join equiatomic CrMnFeCoNi-based high-entropy alloys in solid state without any compositional segregation in the joining zone. Finally, Zhang et al. [25] investigated the fatigue performance of an EAPJed bulk joint of SUS316L and SUS410. In this dissertation, a comprehensive investigation on the application of electric current, including EA annealing, EA crack healing, and EAPJ, was systematically investigated.

In the present study, in chapter II, EA rapid heat treatment was used to rapidly enhance the formability of the aluminum clad steel (ACS) sheet while adjusting the intermetallic evolution. During experiment, A single pulse with different current densities of 120 A/mm^2, 150 A/mm^2, 170 A/mm^2, and 190 A/mm^2 was adopted to investigate the effect of the current density on intermetallic evolution, which will in turn affect the mechanical properties of the ACS sheet. The intermetallic formation and evolution with increasing current density were characterized using a field emission scanning electron microscope (FE-SEM: SU5000, Hitachi, Japan) equipped with an energy dispersive spectrometer (EDS: X-Max50, Horiba, Japan). The mechanical properties of the EA rapid heat-treated samples were evaluated by quasi-static tensile tests and microhardness tests.

In chapter III, the fatigue damage evolution of the ACS sheet was investigated by scanning electron microscope (SEM) images and electron backscatter diffractometer (EBSD)

observations from samples that suffered different fatigue cycles. In addition, the prolonged fatigue life by electropulsing treatment was demonstrated by comparing the microstructural change between electropulsing treated samples and untreated samples. For prolonging fatigue life by electropulsing treatment, the fatigue test was stopped at 0.7 times failure life for each corresponding fatigue loading condition with applied maximum stress of 255, 245, and 235 MPa. Then, the electric pulse with a current density of 150 A/mm^2 and a duration of 0.5 sec was applied to the fatigued samples to prolong the fatigue life by restoring the damaged microstructure.

From chapter IV to chapter VI, solid-state joints of various combinations of dissimilar metal alloys, such as S45C and Al661-T6, additively manufactured AMMS1 and conventional SUS410, and SUS316L and SUS410, are successfully fabricated by EAPJ technique. Firstly, Lap joining of dissimilar steel S45C and aluminum 6061-T6 alloy sheets in the solid state is conducted by means of EAPJ. Second, for the material combination of SUS316L and SUS410, the fatigue behavior of the joints is evaluated by a P-S-N curve using two-parameter Weibull distribution. Finally, for the joining of additively manufactured maraging steel and conventional SUS410, the base sample of additively manufactured cylindrical maraging steel specimen is fabricated to have a porous layer on the joining end, while another end is printed as a perfectly solid matrix. The porous layer significantly increases the maximum joining temperature by the locally increased electrical resistance and dramatically enhances the interfacial diffusion thickness. The effect of the porous layer on the microstructural evolution and mechanical properties is characterized by the electron back-scatter diffraction and quasi-static tensile test, respectively. The microstructure of the cross-sections of these dissimilar joints were observed by microstructural analysis (FE-SEM with EBSD and EDS). The

mechanical properties of the dissimilar joint were evaluated by Vickers hardness measurements and quasi-static tensile tests.

REFERENCES

[1] Ruszkiewicz, B. J., Grimm, T., Ragai, I., Mears, L., and Roth, J. T. (September 13, 2017). "A Review of Electrically-Assisted Manufacturing With Emphasis on Modeling and Understanding of the Electroplastic Effect." ASME. J. Manuf. Sci. Eng. November 2017; 139(11): 110801.

[2] E.S. Machlin, Applied voltage and the plastic properties of``Brittle"rock salt, J. Appl. Phys. 30(7) (1959) 1109-1110.

[3] J.T. Roth, I. Loker, D. Mauck, M. Warner, S.F. Golovashchenko, A. Krause, Enhanced formability of 5754 alu11minum sheet metal using electric pulsing, Trans. NAMRI/SME. 36 (2008) 405-412.

[4] D. Zhang, S. To, Y. Zhu, H. Wang and G. Tang, Dynamic electropulsing induced phase transformations and their effects on single point diamond turning of AZ91 alloy, Journal of Surface Engineered Materials and Advanced Technology, 2 (2012) 16-21

[5] W. P. Yu, R. S. Qin and K. M. Wu, The effect of hot-and cold-rolling on the electropulse-induced microstructure and property changes in medium carbon low alloy steels, Steel Research International, 84 (2013) 443-449

[6] M.-J. Kim, K. Lee, K.H. Oh, I.S. Choi, H.H. Yu, S.-T. Hong, H.N. Han, Electric current-induced annealing during uniaxial tension of aluminum alloy, Scr. Mater. 75 (2014) 58–61.

[7] Conrad, H., Karam, N., Mannan, S. and Sprecher, A. (1988). Effect of electric current pulses on the recrystallization kinetics of copper. Scripta metallurgica, 22(2), 235-238.

[8] Conrad, H., Karam, N. and Mannan, S. (1983). Effect of electric current pulses on the recrystallization of copper. Scripta metallurgica, 17(3), 411- 416.

[9] Wang, T., Xu, J., Xiao, T., Xie, H., Li, J., Li, T. (2010). Evolution of dendrite morphology of a binary alloy under an applied electric current: An in situ observation. Physical Review E - Statistical, Nonlinear, and Soft Matter Physics, 81(4).

[10] Jeong, H. J., Kim, M. J., Park, J. W., Yim, C. D., Kim, J. J., Kwon, O. D. and Han, H. N. (2017). Effect of pulsed electric current on dissolution of Mg 17 Al 12 phases in as-extruded AZ91 magnesium alloy. Materials Science and Engineering A, 684, 668-676.

[11] Choi, J., Sung, H. M., Roh, K. B., Hong, S. H., Kim, G. H. and Han, H. N. (2017). Fabrication of sintered tungsten by spark plasma sintering and investigation of thermal stability. International Journal of Refractory Metals and Hard Materials, 69, 164-169.

[12] Y. Estrin, L.S. Tóth, A. Molinari, Y. Bréchet, A dislocation-based model for all hardening stages in large strain deformation. Acta Mater. 46 5509- 5522 (1998).

[13] H. Conrad, Electroplasticity in metals and ceramics, Materials Science and Engineering: A, 287 (2000) 276-287.

[14] M.-J. Kim, S. Yoon, S. Park, H.-J. Jeong, J.-W. Park, K. Kim, J. Jo, T. Heo, S.-T. Hong, S.H. Cho, Y.-K. Kwon, I.-S. Choi, M. Kim, H.N. Han, Elucidating the origin of electroplasticity in metallic materials, Applied Materials Today, 21 (2020) 100874.

[15] M.-J. Kim, M.-G. Lee, K. Hariharan, S.-T. Hong, I.-S. Choi, D. Kim, K.H. Oh, H.N. Han, Electric current–assisted deformation behavior of Al-Mg-Si alloy under uniaxial tension, International Journal of Plasticity, 94 (2017) 148-170.

[16] J.-W. Park, H.-J. Jeong, S.-W. Jin, M.-J. Kim, K. Lee, J.J. Kim, S.-T. Hong, H.N. Han, Effect of electric current on recrystallization kinetics in interstitial free steel and AZ31 magnesium alloy, Materials Characterization, 133 (2017) 70-76.

[17] J. Zhang, L. Zhan, S. Jia, Effects of Electric Pulse Current on the Aging Kinetics of 2219 Aluminum Alloy, Advances in Materials Science and Engineering, 2014 (2014) 1-8.

[18] Y. Tang, A. Hosoi, Y. Morita, Y.J.I.j.o.f. Ju, Restoration of fatigue damage in stainless steel by high-density electric current, 56 (2013) 69-74.

[19] J. Jung, Y. Ju, Y. Morita, Y. Toku, Enhancement of fatigue life of aluminum alloy affected by the density of pulsed electric current, International Journal of Fatigue, 103 (2017) 419-425.

[20] C.L. Yang, H.J. Yang, Z.J. Zhang, Z.F. Zhang, Recovery of tensile properties of twinning-induced plasticity steel via electropulsing induced void healing, Scripta Materialia, 147 (2018) 88-92.

[21] Z. Xu, L. Peng, X. Lai, Electrically assisted solid-state pressure welding process of SS 316 sheet metals, Journal of Materials Processing Technology, 214 (2014) 2212-2219.

[22] Y.-F. Li, H. Das, S.-T. Hong, J.-W. Park, H.N. Han, Electrically assisted pressure joining of titanium alloys, Journal of Manufacturing Processes, 35 (2018) 681-686.

[23] Y.-F. Li, S.-T. Hong, H. Choi, H.N. Han, Solid-state dissimilar joining of stainless steel 316L and Inconel 718 alloys by electrically assisted pressure joining, Materials Characterization, 154 (2019) 161-168.

[24] M.-G. Jo, T.A.N. Nguyen, S. Park, J.-Y. Suh, S.-T. Hong, H.N. Han, Electrically Assisted Solid-State Joining of CrMnFeCoNi High-Entropy Alloy, Metallurgical and Materials Transactions A 51(12) (2020) 6142-6148.

[25] S. Zhang, K. Gao, L. Cai, S.Y. Anaman, S.-T. Hong, H.-H. Cho, P.-C. Lin, H.N. Han, Microstructural evolution and fatigue performance of dissimilar solid-state joints of SUS316L and SUS410, Journal of Materials Research and Technology, 16 (2022) 555-569.

CHAPTER II

EFFECTS OF INTERMETALLIC EVOLUTION BY ELECTRICALLY ASSISTED RAPID HEAT TREATMENT ON THE MECHANICAL PERFORMANCE AND FORMABILITY OF ALUMINUM CLAD STEEL

2.1 INTRODUCTION

Aluminum clad steel (ACS), which consists of a substrate of steel and a cladding layer of aluminum, has balanced performance featuring the high strength of steel and lightweight nature of aluminum (high specific strength), high thermal conductivity, and good corrosion resistance. It is widely used to fabricate heat exchangers, cookware, electronics, and battery cases of electric vehicles [1-4]. The cold roll bonding (CRB) process is an effective solid-state joining method for the industrial production of the ACS due to its simplicity, economic, and efficiency, which bond the material by severe plastic deformation. Several theories were proposed to explain the mechanism of CRB: film theory, diffusion bonding, energy barrier theory, and recrystallization theory [5]. Among them, the film theory is widely accepted as the primary mechanism in CRB, as well as the other pressure joining techniques. According to the film theory, severe deformation fractures the oxide layer and contaminate surface, which extrudes the virgin metals through the cracks and establishes an intimate contact between the stacked layers [5,6]. For fabrication of the ACS sheet by CRB, a high thickness reduction was required to achieve enough surface enlargement and establish good bonding quality, which simultaneously induces a very high work hardening for the ACS sheet. Therefore, subsequent heat treatment is necessary to anneal the severely work-hardened ACS sheet to release the

high residual stress and improve the ductility. In the meantime, metallurgical bonding is also established in the subsequent heat treatment by forming the intermetallic compounds (IMCs). However, undesirable intermetallic compounds (IMCs) can also be formed depending on the conditions of the subsequent heat treatment, which result in low bonding strength and early interfacial debonding during forming process in manufacturing. According to the Fe-Al phase diagram, five IMCs phases (Fe3Al, FeAl, FeAl2, Fe2Al5, FeAl3) can form at the interface between aluminum and steel layers. A higher Al content of the IMCs such as Fe2Al5 and FeAl3 are reported to be very brittle and can lead to premature failure or delamination during deformation [7,8]. Despite the IMCs type, the thickness of the formed IMCs was also reported to have an important effect on the joining strength of the Fe/Al joints [9]. Particularly, during tensile deformation, interfacial phases of the clad metals (laminated metal composites) acted as barriers playing an essential role in the bonding strength, work hardening, and damage evolution [10,11]. Thus, the optimization of annealing treatment is important to adjust the interfacial IMCs to achieve sound bonding strength and good formability of the ACS sheet for the final shaping process.

Several researchers have investigated the effects of the annealing process on the mechanical properties of ACS by identifying the IMCs. Milad et al. [12] manufactured an Al/steel multilayered composite by accumulative roll bonding and investigated the effects of annealing on the microstructural and mechanical characteristics. They found that the strength decreased and the elongation increased after annealing, and the dramatically reduced strength was due to the formation of brittle intermetallic at an annealing temperature of 500 °C. Jeong et al. [7] reported the formation of Fe2Al5 phase at the interface during the annealing treatment of the CRBed ACS at 540 °C for 16 h. Yang et al. [13] investigated the effect of the

annealing temperature and time on the microstructure evolution and mechanical properties of the ACS. The results show that the mechanical properties of the ACS can be seriously deteriorated when the thickness of the IMC layer is over 10 μm.

One clear disadvantage of conventional annealing process for ACS is that the specimen needs to be maintained at an elevated temperature for a few hours up to dozens of hours through furnace heating [12,13]. Therefore, developing a less-time consuming annealing process can improve the process efficiency and energy efficiency. Using an electric current as a heating source provides faster resistance heating and the athermal effect (electroplastic effect [14-18]) of the electric current. In addition to the thermal effect of resistance heating, the athermal effect of an electric current can accelerate annealing and atomic diffusion by enhancing the kinetics of the metal atoms [14-16]. Furthermore, it was also pointed out that the athermal effect of electric current can accelerate the recrystallization kinetics during electropulsing treatment [17] and enhance the kinetics of microstructural changes to reset the damaged microstructure of metallic materials [18]. Park et al. [19] stated that the electrically assisted stress relief annealing significantly reduced the process time and enhanced the annihilation of dislocations compared with conventional stress relief process. Dinh et al. [20] experimentally investigated the intermetallic evolution of Al-Si-coated hot stamping steel during electrically assisted (EA) rapid heating, and they suggested that EA heating can be effectively used as a rapid heating method to improve the efficiency of a hot stamping process. Zhang et al. [9] concluded that the different IMCs with a different relative thickness formed in electrically assisted pressure joining of SM45C and aluminum 6061-T6 resulted in different interfacial joint strengths. Furthermore, Chen et al. [21] found that the electric current pulse

can eliminate the interfacial residual voids and improve the peel strength of the cast steel/aluminum clad sheet.

The present study was aimed to utilize the advantages of EA rapid heat treatment to balance the bonding strength and formability of the ACS sheet by adjusting the intermetallic evolution (enhanced interfacial diffusion). Furthermore, the effect of the electric current density on the mechanical properties and formability was evaluated by the tensile test and U-shape forming test, respectively.

2.2 EXPERIMENTAL SET-UP

The as-received ACS sheet with a thickness ratio of 0.4 mm: 0.3 mm for mild steel (PosACC) and aluminum 1050 alloy (Al1050-O) was fabricated following a conventional manufacturing process, including CRB and the subsequent furnace annealing, as schematically shown in Fig. 2.1(a). The annealed ACS sheet was used as the base material (BM) for the EA rapid heat treatment experiment. The chemical compositions of the mild steel and Al1050 are listed in Table 2.1. The ACS BM sheet was cut into two different shapes for the tensile test and U-shape forming test. The dimensions of the subsize tensile specimen (ASTM E8/E8M) are given in Fig. 2.1(b). Strip samples with a width of 25 mm and a length of 250 mm are used in the U-shape forming test to evaluate the formability of the ACS sheet.

For the EA rapid heat treatment, the electric pulse was generated by a controllable generator (SP-1000U, Hyosung, South Korea) and was applied to the samples for a period of 0.5 s to achieve rapid heating (thermal effect) and induce the athermal effect of electric current. The combined thermal and athermal effects were expected to enhance the interfacial

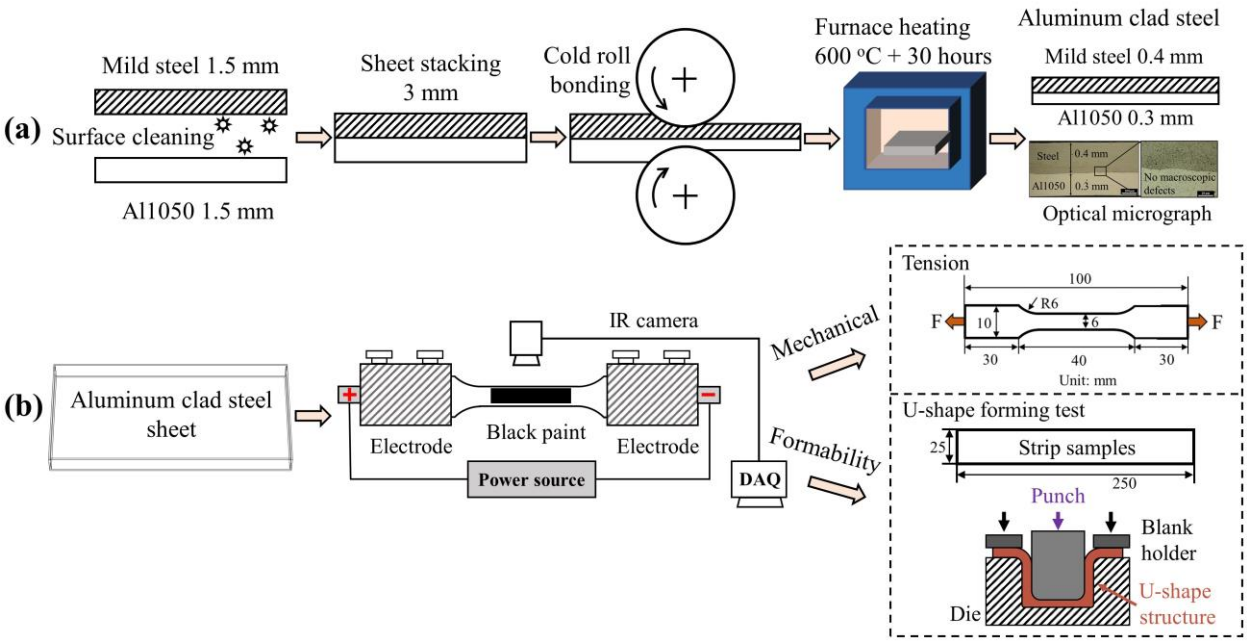

Fig. 2.1. Schematics of the experimental set-up: (a) manufacturing process of the aluminum clad steel sheet and (b) electrically assisted rapid heat treatment and subsequent mechanical testing

Table 2.1. Chemical compositions of the raw materials (wt%)

Elements	Fe	Al	C	Si	Mn	P	S	Cu	Ti
Mild steel	Bal.	-	0.002	-	0.219	0.006	0.005	-	-
Al1050	0.702	Bal.	-	0.603	-	-	-	0.001	0.016

atomic diffusion. A single pulse with different current densities of 120 A/mm^2, 150 A/mm^2, 170 A/mm^2, and 190 A/mm^2 was adopted to investigate the effect of the current density on intermetallic evolution, which will in turn affect the mechanical properties of the ACS sheet. The current density is simply calculated by dividing the applied electric current by the cross-

sectional area perpendicular to the direction of electric current for each specimen, as depicted in Fig. 2.1(b). Representative current densities of 150 A/mm^2 and 170 A/mm^2 were also applied four times to investigate the effect of multiple pulses on the mechanical properties of the ACS sheet. The samples electrically pulsed under different current densities were labeled based on the applied current density and repetition number (for example, 170-I and 170-IV represent samples treated with a single pulse under 170 A/mm^2 and four pulses under 170 A/mm^2, respectively). Note that the samples were cooled down to room temperature prior to applying the next pulse in the multi-pulse treatment. During the application of the electric pulse, the temperature histories were monitored by an infrared thermal imaging camera (FLIR-T621, FLIR, Sweden). Black paint was sprayed on the surface of the samples to stabilize the emissivity and improve the accuracy of the recorded temperature. The parameters of the EA rapid heat treatment are summarized in Table 2.2.

Table 2.2. Process parameters during electrically assisted rapid heat treatment

Sample ID	Density of electric pulse (A/mm^2)	Duration of electric pulse (sec)	Number of cycles
120-I	120	0.5	1
150-I and 150-IV	150	0.5	1 and 4
170-I and 170-IV	170	0.5	1 and 4
190-I	190	0.5	1

After EA rapid heat treatment, the samples were cross-sectioned along the width direction and then ground and polished following a standard metallographic preparation process. The interface was first observed by laser confocal microscopy (VK-X200, Keyence, Osaka, Japan) for macro-assessment of the joint quality. The intermetallic formation and evolution with increasing current density were characterized using a field emission scanning electron microscope (FE-SEM: SU5000, Hitachi, Japan) equipped with an energy dispersive spectrometer (EDS: X-Max50, Horiba, Japan).

The mechanical properties of the EA rapid heat-treated samples were evaluated by quasi-static tensile tests and microhardness tests. Quasi-static tensile tests were conducted on a universal tensile machine with a constant displacement rate of 0.5 mm/min. During the tensile test, the displacement history was recorded by an LX500 laser extensometer (MTS, USA) for the subsequent calculation of the true stress-strain curve and work hardening exponent of the sample. Additionally, the deformation characteristics on both the steel and Al1050 sides were recorded by an ARAMIS digital image correlation (DIC) system (GOM, Germany) after spraying black speckled paint on the surface with a white primer background to investigate the fracture mechanism of the ACS sheet during tension. The strain distribution and evolution with the tensile displacement were mapped by the post-analysis software GOM Correlate 2020. For verifying the repeatability, four specimens for each heat treatment condition were tensile tested. Vickers hardness measurements (2 N, 10 s on the steel side; 0.5 N, 10 s on the Al1050 side) were performed at the locations near interface on both steel and Al1050 layers using a Vickers indenter (HM-200, Mitutoyo, Japan). After the tensile test, the vicinity of the fracture region was cross-sectioned and observed along the loading direction using an optical microscope to characterize the interfacial fracture evolution during tension. The fracture

surfaces perpendicular to the loading direction were observed by SEM to understand the failure mechanism of the tensile samples. In addition, the performance of the formability was evaluated by U-shape forming tests after EA rapid heat treatment. The U-shape forming test with an identical compressive displacement of 22 mm was performed for base, 170-I, and 170-IV specimens to assess the effect of the EA rapid heat treatment on the formability. The U-shape forming tests for all cases were conducted under the same experimental conditions without any lubricant.

2.3 RESULTS AND DISCUSSIONS

The optical microscopy (OM) image of the cross-section of the ACS BM sheet along the rolling direction suggests the formation of a sound and smooth joint interface without macro-defects as a result of CRB and subsequent annealing (Fig. 2.1(a)). The temperature histories during EA rapid heat treatment (Fig. 2.2(a)) show that peak temperatures of approximately 250 °C, 350 °C, 450 °C, and 550 °C were reached for 120-I, 150-I, 170-I, and 190-I samples, respectively. In addition, the samples with the periodically applied electric pulses (four times) and current densities of 150 A/mm^2 and 170 A/mm^2 exhibit good repeatability in terms of the peak temperature (Fig. 2.2(b)).

IPF maps of BM and 190-I samples were compared to verify the effect of the electric current density on the microstructural change since the 190-I sample experienced the maximum electric current density and the highest peak temperature (Fig. 2.2(a)). As shown in Fig. 2.3, no significant difference in the microstructure (the grain shape and size) was observed for both the Al1050 and steel sides between the BM and 190-I samples. Note that the black region in Fig. 2.3(b) indicates a thick IMC layer and will be discussed further in the next

section. The nearly identical microstructures of the BM and 190-I (highest current density) samples suggest that the current densities selected in the present study did not alter the microstructure of the sample.

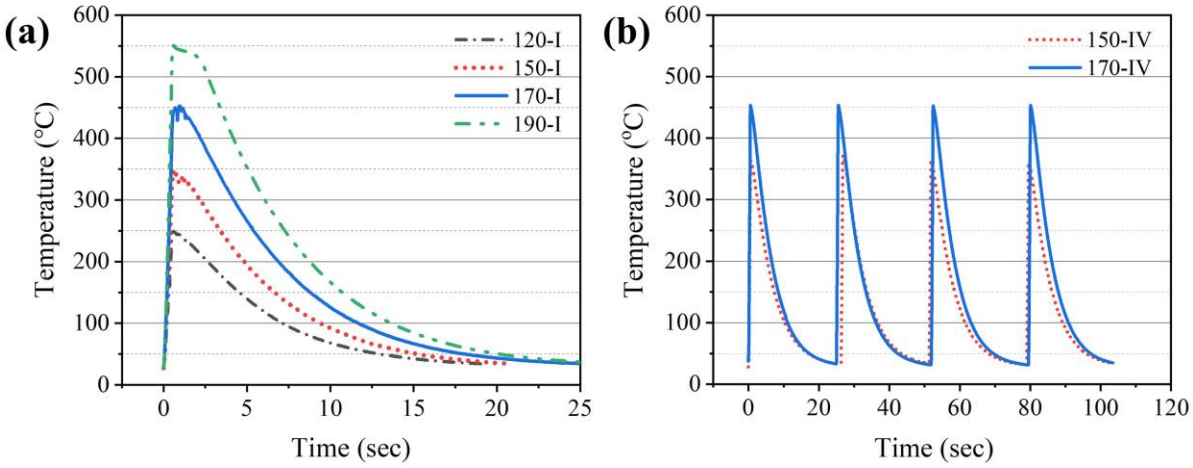

Fig. 2.2. Temperature histories during electrically assisted rapid heat treatment: (a) single pulse treatment and (b) four pulses treatment

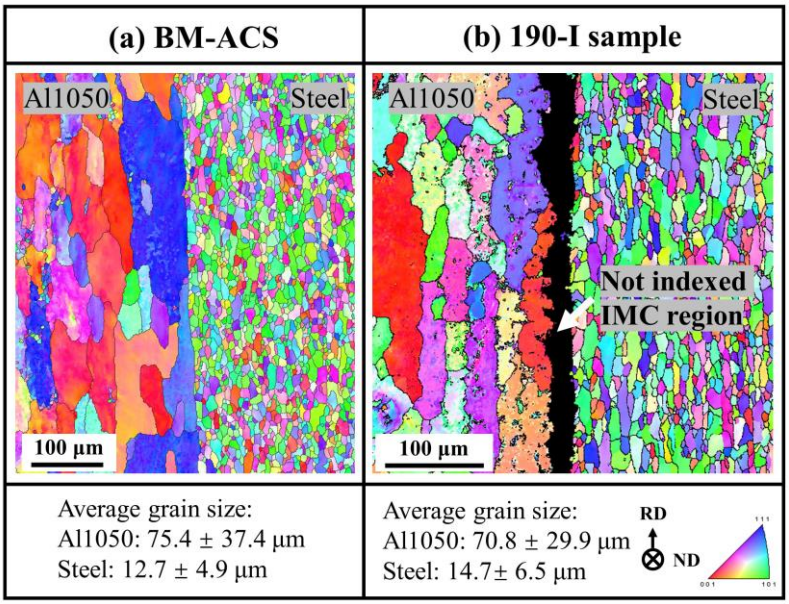

Fig. 2.3. EBSD IPF maps: (a) BM-ACS sample and (b) 190-I sample

To understand the intermetallic evolution in relation to the current density, the BM, 170-I, and 190-I samples were cross-sectioned for SEM-EDS analysis to determine the interfacial diffusion and phase constituents. The representative sample with the four-pulse treatment (170-IV) was also cross-sectioned for SEM-EDS analysis to investigate the effect of the multi-pulse application on the intermetallic evolution. The SEM results of the BM sample (Fig. 2.4(a)) suggested that a smooth and sound solid-state joint without micro-defects was fabricated with an interfacial diffusion thickness of about 1 μm (intermetallic formation). In EA rapid heat treatment, the interfacial diffusion thickness was not observably increased and maintained near consistency (1 μm) when the current density was lower than 170 A/mm^2, as shown in the results for 170-I and 170-IV (Figs. 2.4(b) and (c)). However, a significantly increased interfacial diffusion thickness (about 6 μm) was formed for 190-I (Fig. 2.4(d)). The results suggested that the interfacial diffusion thickness was majorly controlled by the peak temperature (or the magnitude of current density) rather than the repetition of the electric pulse when the current density was relatively low (in the present study, for the current density up to 170 A/mm^2). According to the line scan results, the intermetallic was majorly embedded at the interface toward the steel side for the BM, 170-I, and 170-IV samples. The higher current density of 190 A/mm^2 significantly activated the intermetallic growth toward the Al1050 side and finally formed a thick IMC layer along the interface. Therefore, point analysis was performed at the steel side near the interface for the BM, 170-I, and 170-IV samples, while analysis was carried out at the point located at the center of the IMC layer for 190-I, as presented in Fig. 2.4. The point analysis results (Table 2.3) revealed that the EA rapid heat treatment altered the ratio of Fe:Al, resulting in the formation of different phases at the interface. Fe_3Al and FeAl were detected along the joint interface of the BM and 170-I

samples, respectively. The phase of FeAl was changed to Fe_2Al_5 in 170-IV as a result of the enhanced diffusion by repeatedly applying the electric pulse. Note that the diffusion thickness was not observably changed after applying four pulses. In 190-I, the IMC layer is primarily composed of Fe_2Al_5 with a significantly increased thickness of about 6 μm, which resulted from the higher peak temperature. The formation of the different IMCs under different current densities can be explained by a combined result of peak temperature and accelerated mobility of the atoms when increasing the density of the electric pulse. In addition to the well-known temperature effect on the formation of the IMC, the athermal effect of the electric current can be further enhanced with the increase of the current density due to the charge imbalance near the defects, which in turn motivated the diffusion of the atoms and resulted in the formation of different IMCs [20,22].

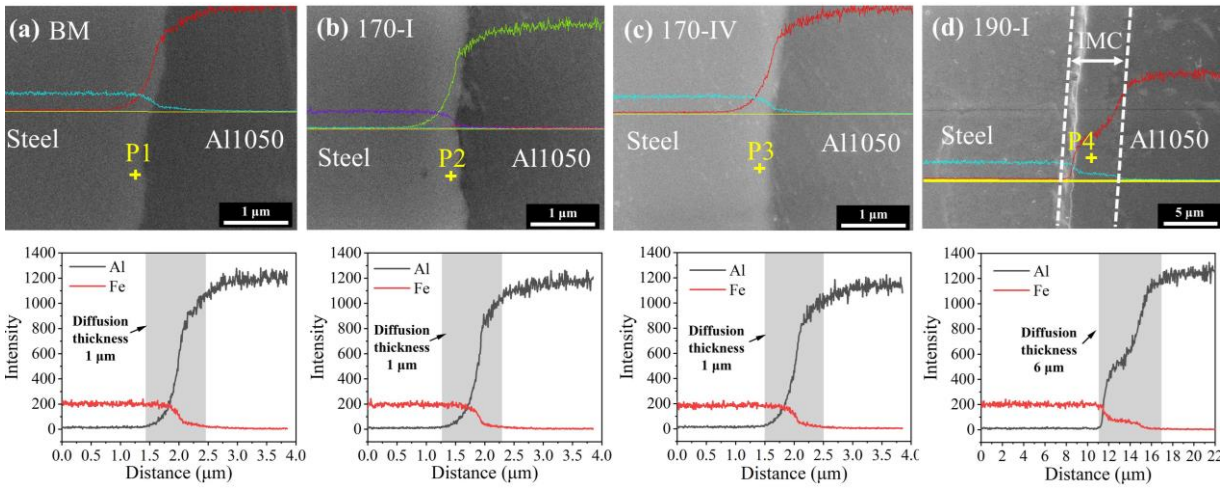

Fig. 2.4. SEM images and EDS line scan of the major elements: (a) BM sample, (b) 170-I sample, (c) 170-IV sample, and (d) 190-I sample

Table 2.3. Phase constituents of the IMC layer

Samples	Locations	Fe at%	Al at%	Possible phase	Diffusion thickness (μm)
BM	P1	69.17	30.83	Fe_3Al	1
170-I	P2	60.38	39.62	FeAl	1
170-IV	P3	29.77	70.23	Fe_2Al_5	1
190-I	P4	26.36	73.64	Fe_2Al_5	6

Microhardness indentations, located at each layer near the interface (about 10 μm away from the interface), were performed four times for all single-pulsed samples, as schematically shown in Fig. 2.5. The microhardness profiles showed that the steel layer was barely affected in terms of the microhardness by all the EA rapid heat treatments. In contrast to the general rule of the aluminum heat treatment, the microhardness of the Al layer was initially kept constant (about 35 HV) up to the current density of 170 A/mm^2, but then significantly increased to about 52 HV at the current density of 190 A/mm^2. Note that the peak temperature and the thickness of the IMC layer under 190 A/mm^2 is 550 °C and 6 μm, respectively. The increase (rather than a decline) in the microhardness for the Al layer under 190 A/mm^2 can be explained by the combined effects of the formation of a thick IMC layer and thermal mismatch dislocations [23]. Thermal mismatch dislocations were generated by the interfacial thermal stress that occurred while applying the electric pulse due to the large differences in the thermal conductivity between steel and Al1050.

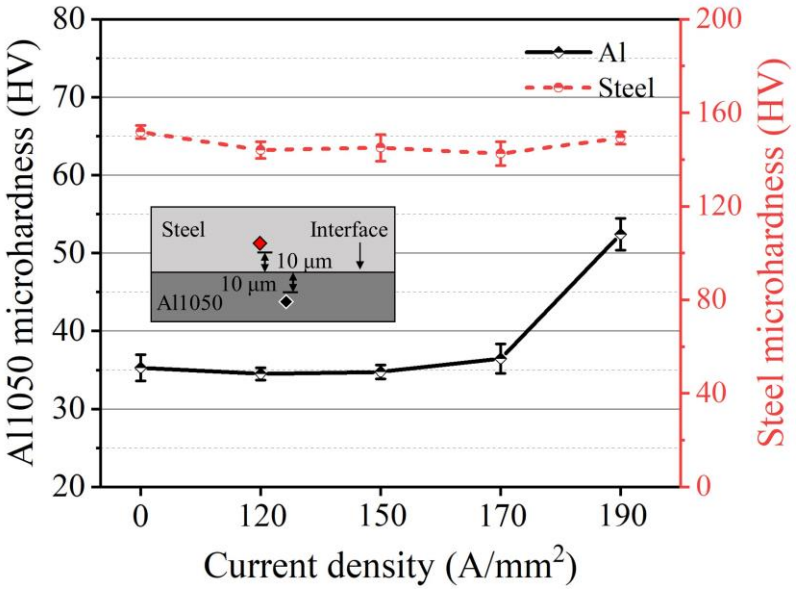

Fig. 2.5. Microhardness changes with the current density for all single pulsed samples

Representative true stress-strain curves (Fig. 2.6(a)) show that the mechanical properties were barely affected when the current density was lower than 150 A/mm^2. However, when increasing the current density to 170 A/mm^2, the yield strength of 255 MPa for BM sample was reduced to 230 MPa, while the elongation was increased from about 12% to 15%. The decreased yield strength and improved elongation were caused by the combined effects of annealing and the enhanced interfacial bonding strength [24-27]. However, the yield strength and elongation were significantly reduced with a further increase in the current density to 190 A/mm^2, as summarized in Fig. 2.6(b). Note that the elongation of the 190-I sample was even lower than the BM sample. In addition, the fracture appearance (Fig. 2.6(c)) of the 190-I sample shows a fracture perpendicular to the loading direction, while all the other samples fractured at about 45° to the loading direction.

It is well known that the work hardening exponent (n) can be expressed by the Hollomon equation in the stage of uniform plastic deformation:

$$\sigma = k\varepsilon^n \quad (1)$$

Taking the natural logarithm on both sides of eq. (1) yields eq. (2):

$$ln\,\sigma = n\,ln\,\varepsilon + ln\,k \quad (2)$$

Here, σ and ε are the true stress and true strain, respectively, while k and n are the strength coefficient and work hardening exponent, respectively. The n value (Fig. 2.6(d)) has nearly no change under current densities lower than 150 A/mm^2 and then gradually increases with increasing current density. The maximum n value of 0.138 was obtained for 190-I due to the formation of a thick IMC layer. The significantly increased thickness of the IMC layer hinders dislocation movement across the interface, results in pinning of dislocation at the interface, and promotes the dislocation multiplication, which significantly increases the hardening behavior during plastic deformation [23]. The accumulated shear stress resulting from the increased hardening behavior along the interface during plastic deformation causes premature fracture of the interface. Thus, cracking occurs at the early stage and significantly decreases the elongation of the 190-I sample.

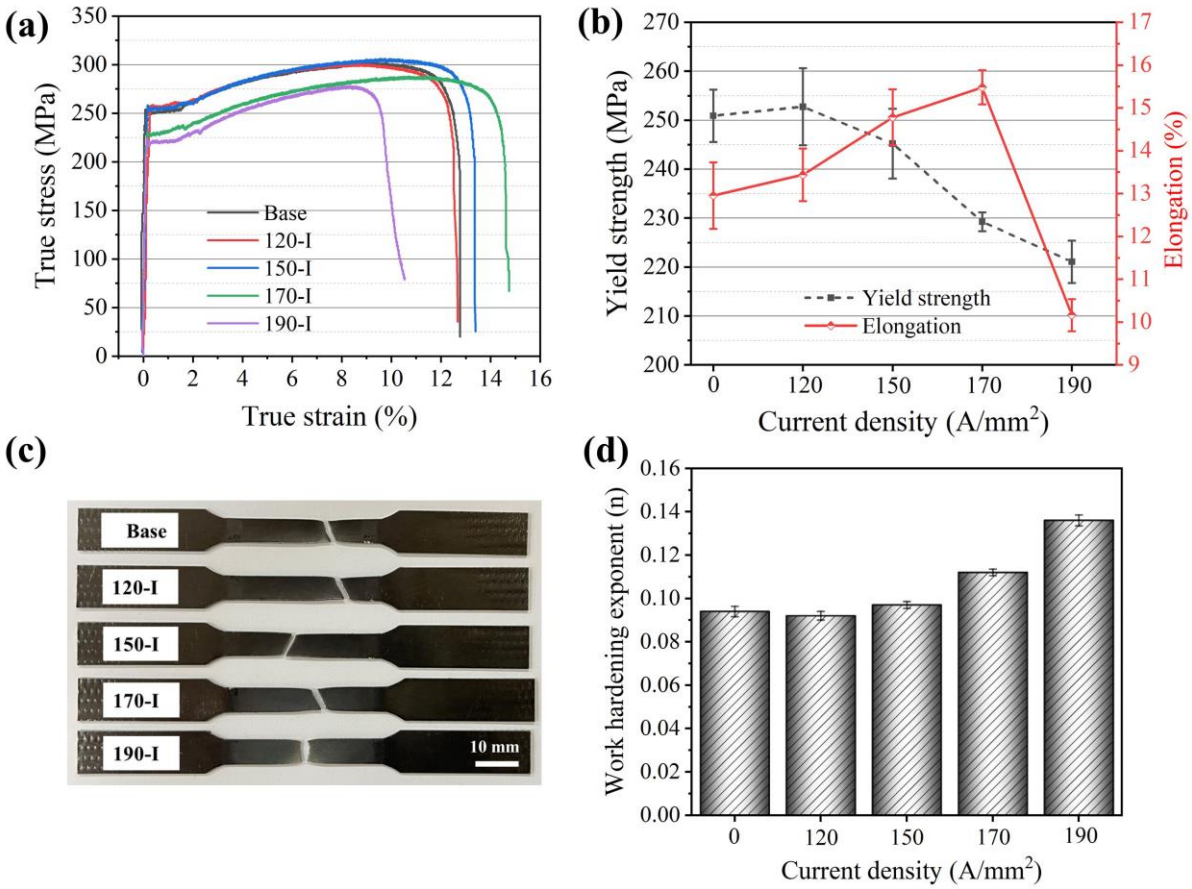

Fig. 2.6. Tensile test results of the single pulse treatment: (a) true stress-strain curves, (b) the change of yield strength and elongation with the current densities, (c) fracture appearance, and (d) the change of work hardening exponent with the current densities

The true stress-strain curves (Fig. 2.7(a)) for the samples undergoing the four-pulse treatment suggest that this treatment under representative current density (150 and 170 A/mm^2) further decreased the yield strength and increased the elongation, as summarized in Fig. 2.7(b). The work hardening exponent (Fig. 2.7(d)) was increased by repeatedly applying four pulses for each corresponding current density due to the IMC evolution (enhanced diffusion). The fracture appearances (Fig. 2.7(c)) of the 150-IV and 170-IV samples also show fracture 45° to

the loading direction, which is similar to the fractures of the 150-I and 170-I samples. The current results revealed that the elongation could be further increased by repeatedly applying multiple pulses under a relatively low current density instead of using a higher current density; this approach avoided the deterioration of the mechanical properties of the ACS sheet caused by the severely thickened IMC layer under a higher current density (190 A/mm^2).

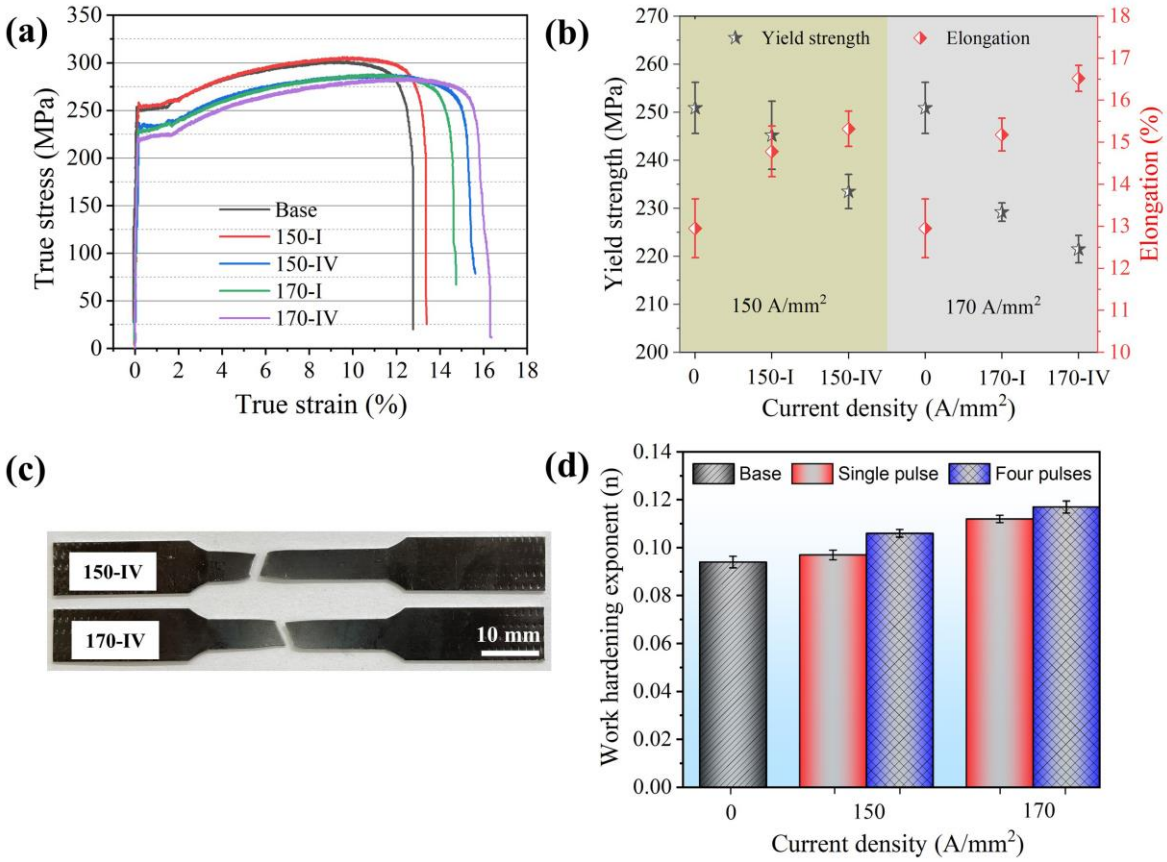

Fig. 2.7. Comparison between single pulse and four pulses treatment for representative current densities of 150 A/mm^2 and 170 A/mm^2: (a) true stress-strain curves, (b) the change of yield strength and elongation with the current densities, (c) fracture appearance, and (d) the change of work hardening exponent with the current densities

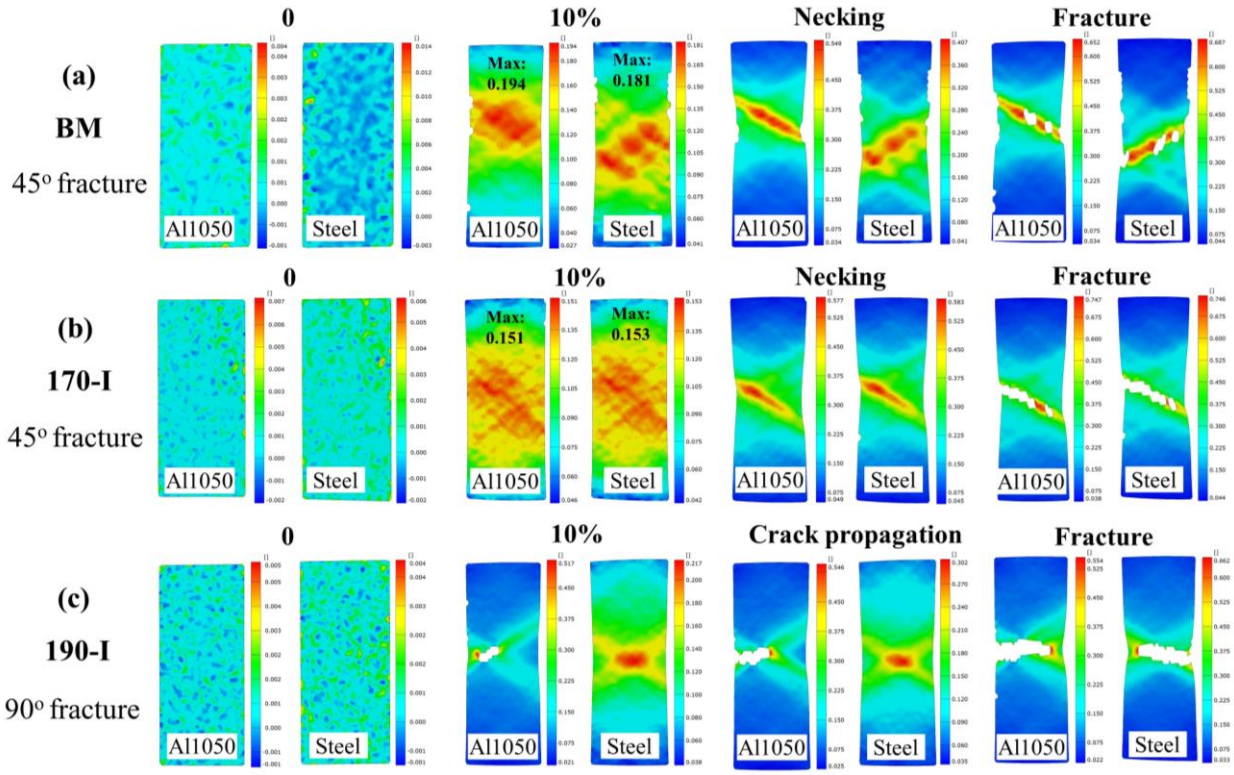

Fig. 2.8. Strain distribution observed by DIC during tensile test: (a) BM sample, (b) 170-I sample, and (c) 190-I sample

To determine the failure process of the ACS sheet during tensile test, the strain distribution at an elongation of 0%, 10%, necking, and fracture for the BM, 170-I, and 190-I samples were mapped from DIC tests, as presented in Fig. 2.8. As shown in the figure, many discrete shear bands were developed at about 45° to the loading direction at the elongation of 10% for the BM and 170-I samples (Figs. 2.8(a) and (b)), which resulted from the local and uneven deformation during tensile tests. Intriguingly, the maximum local strain for 170-I appears to be lower than that of the BM sample at the same elongation of 10% for both the Al1050 and steel sides. This is due to the more even distribution of the local strain in 170-I.

The more even distribution of the local strain, resulting from the appropriate EA rapid heat treatment, significantly delayed the earlier combination of the shear bands, which dramatically increased the fracture elongation compared with the BM sample. After necking, a predominant shear band at about 45° to the loading direction was developed, eventually resulting in simultaneous fracture on both sides. Alternatively, the strain (10% elongation in Fig. 2.8(c)) was localized at the center region of the 190-I specimen, resulting in crack initiation and propagation from the center site. Then, the crack propagated to the edge side from the center region with the tensile displacement, which caused the final fracture to be perpendicular to the loading direction. It is interesting to note that for the 190-I specimen, the crack initiation and propagation at the Al1050 side occurred earlier than they did in the steel side (comparing the 10% elongation stage with the crack propagation stage in Fig. 2.8(c)) without obvious necking until fracture due to the hard and thick IMC layer formation on the Al1050 side.

The cross-sections along the loading direction near the fracture region and the fracture surfaces (Fig. 2.9) for the BM, 170-I, and 190-I samples were observed to investigate the fracture mechanism. The cross-section of the BM sample (Fig. 2.9(a)) shows that the steel and Al1050 layers were gradually deformed during plastic deformation, resulting in macro-thinning of the thickness of each layer and local necking at the fracture region. Moreover, interfacial delamination occurred at the region near the fracture surface and extended to the inner side to some extent. In the 170-I sample, similar thinning and necking on each layer were obtained, although less interfacial delamination occurred (Fig. 2.9(b)). The relatively deep and dark interface (Fig. 2.9(d)) also indicated more severe interfacial delamination in the BM sample due to the weaker interfacial bonding strength. The shallow separation of the

interface (Fig. 2.9(e)) for the 170-I sample suggested that the interfacial bonding strength was enhanced by the EA rapid heat treatment. In contrast, the steel and Al1050 layers of the 190-I sample exhibited a non-uniform deformation (Fig. 2.9(c)). The steel layer was independently elongated after the fracture of the Al1050 layer, and it fractured with a

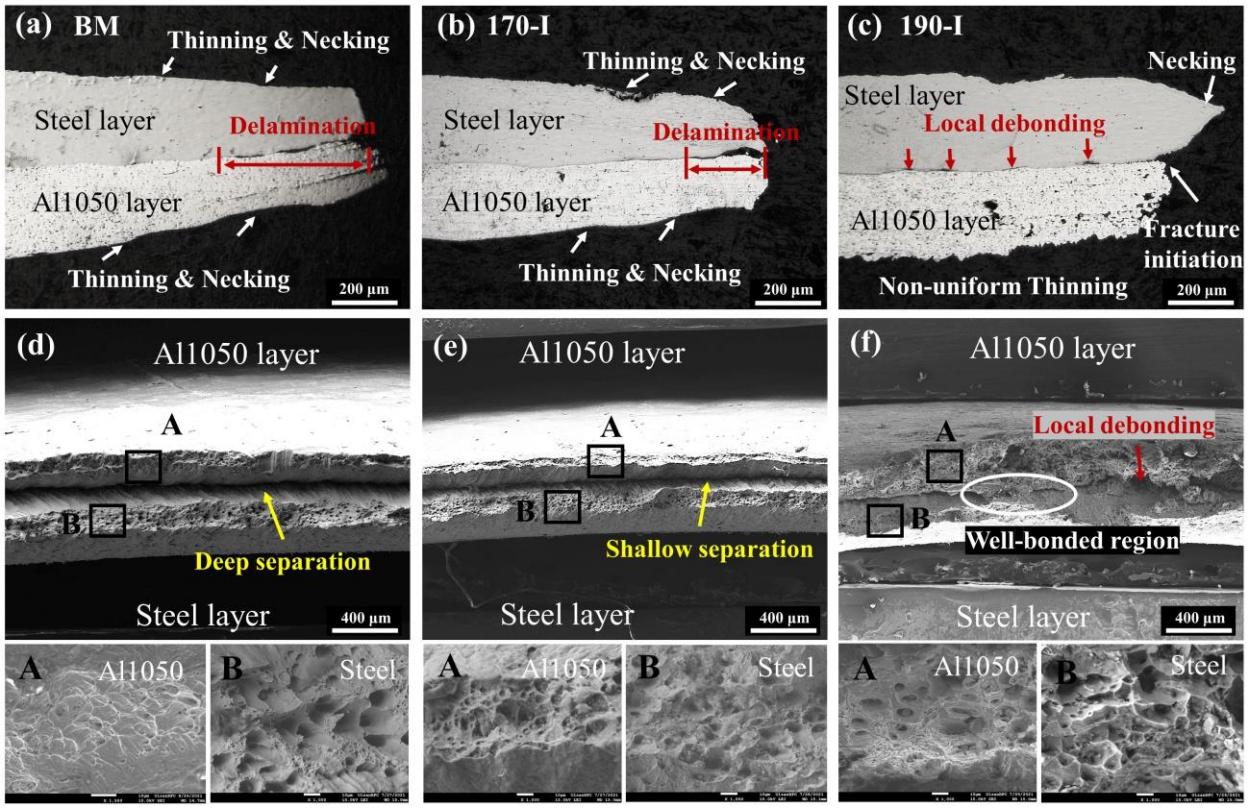

Fig. 2.9. OM images: (a) BM sample, (b) 170-I sample, and (c) 190-I sample along loading direction; SEM images: (d) BM sample, (e) 170-I sample, and (f) 190-I sample perpendicular to the loading direction

typical necking morphology. This demonstrates that an early fracture occurred on the Al1050 layer during plastic deformation. These results correspond well with the observation of the DIC test, as clarified previously. Along the interface of the steel and Al1050 of 190-I sample,

some local debonding sites were observed after the tensile test. These act as crack initiation sites and propagate to the Al1050 layer, causing the Al1050 matrix to fracture at the early stage. The normal fracture surface of the 190-I sample (Fig. 2.9(f)) exhibits a different morphology compared with the BM and 170-I samples, which included some well-bonded regions and local debonding sites rather than complete interfacial delamination. The mixture of well-bonded and local debonding sites suggested that the crack initiated from some local debonding areas, while other areas were still well-bonded during plastic deformation. The enlarged images for each case are presented at the bottom of the relative fracture surface images. These results suggest ductile fracture, as indicated by the dimples that occurred during tensile tests for all conditions. In general, deeper and bigger dimples were observed after EA rapid heat treatment compared to the BM sample.

The fracture mechanism was classified into two different modes: matrix-dominated fracture for current densities up to 170 A/mm^2 and interfacial IMC-dominated fracture for a current density of 190 A/mm^2, as schematically described in Fig. 2.10. In the matrix-dominated fracture mode (Fig. 2.10(a)), the steel and Al1050 suffered different stress conditions during the tensile test due to the large difference in their elastic modulus ($E_{Steel} > E_{Al}$), which resulted in severe shear stress along the interface. Due to the high interfacial bonding strength, the ACS was plastic-deformed uniformly at the early stage of the tensile test, which caused the gradual thinning of each layer. The enhanced strength was attributed to the desired thickness and constituents of the intermetallic component, as altered by EA rapid heat treatment. With increasing plastic deformation, local necking of each layer followed by interfacial delamination occurred. Finally, the sample fractured at about 45° to the loading direction with interfacial delamination. Note that the delamination distance is shorter for EA

rapid heat-treated samples due to the enhanced interfacial bonding strength caused by intermetallic evolution.

In the interfacial IMC-dominated fracture mode for a current density of 190 A/mm^2 (Fig. 2.10(b)), the significantly increased thickness of the IMC layer played a vital role in fracture. The IMC layer acted as an independent embedded layer with the highest elastic modulus E_{IMC}, between the steel and Al1050 layers. The larger difference in elastic modulus between the Al1050 layer and IMC layer compared to the IMC layer and steel layer ($E_{IMC} > E_{Steel} > E_{Al}$) caused more severe shear along the interface of IMC/Al ($\tau_{Al/IMC} > \tau_{IMC/Steel}$), thereby initiating the crack (debonding) at the IMC/Al interface during the early stage of tensile testing due to the hard and brittle characteristics of the IMC. The debonding site acted as the initial crack that propagated toward the Al1050 side resulting fracture in the Al1050 layer at the earlier stage during the tensile test, while the steel layer was plastically deformed. Note that the microhardness of the Al1050 layer near the interface for the 190-I sample was significantly increased after the EA rapid heat treatment. After the fracture of the Al1050 layer, the steel layer was independently plastic-deformed, resulting in local necking and ductile fracture with distinct thickness thinning. Finally, the complete fracture occurred perpendicular to the loading direction.

The formability of the clad materials is majorly affected by the interfacial bonding strength and ductility of each layer. BM, 170-I, and 170-IV samples were used in U-shape forming tests due to their higher elongation observed in single and multi-pulse treatment tests. The U-shape forming test results (Fig. 2.11) suggested that the four-pulse treatment under 170 A/mm^2 (170-IV) significantly improved the formability and successfully deformed the ACS sheet into the desired shape without necking and fracture. However, the BM and 170-I

samples were fractured with distinct necking during the U-shape forming test at the stretch side, which experienced the largest strain and thinning during forming. The current results show good agreement with the observed evolution of mechanical properties during the tensile test. In the present study, the 170-IV sample exhibited the largest elongation and desired formability.

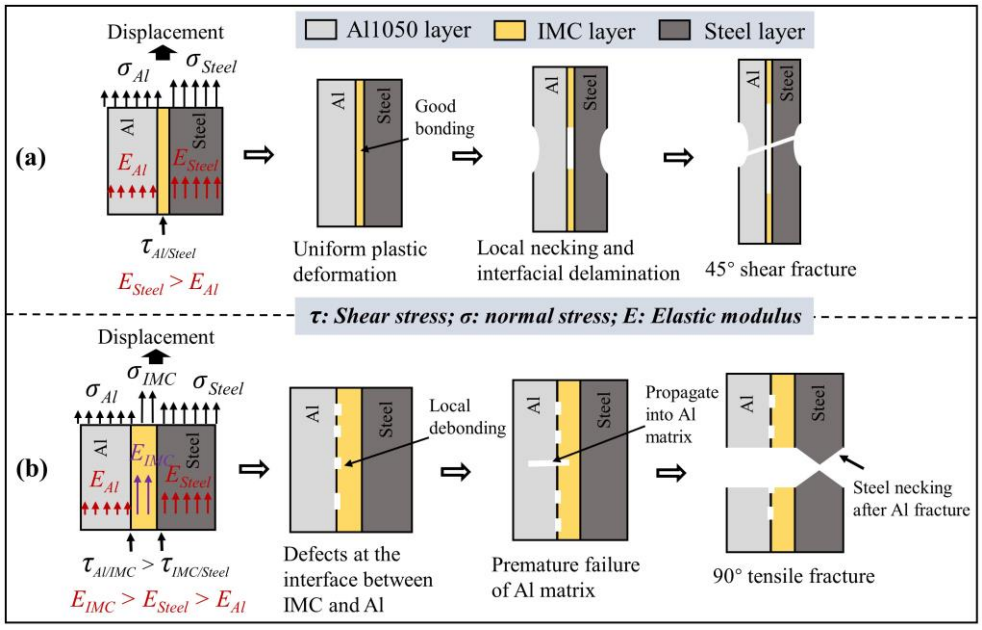

Fig. 2.10. Schematics of the fracture mechanism: (a) matrix-dominated fracture and (b) interfacial IMC-dominated fracture

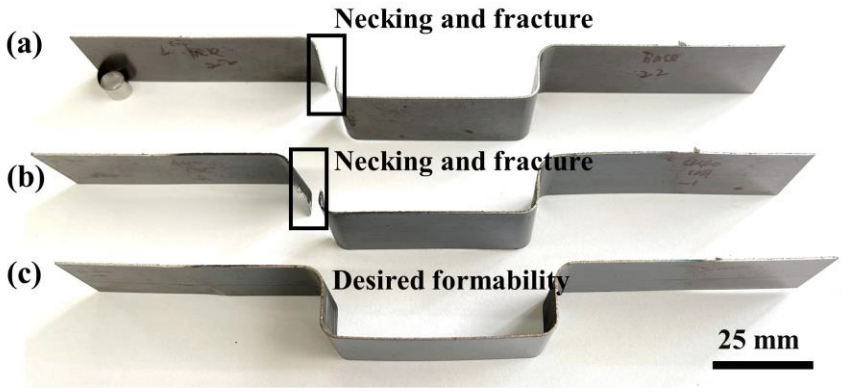

Fig. 2.11. U-shape forming tests: (a) BM sample, (b) 170-I sample, and (c) 170-IV sample

2.4 CONCLUSIONS

In the present study, the intermetallic evolution and mechanical properties of the CRBed ACS sheet were significantly altered by EA rapid heat treatment after CRB and subsequent furnace annealing. The results showed that the yield strength of the ACS sheet was gradually reduced, while the elongation was gradually increased up to the current density of 170 A/mm^2. In the meantime, the interfacial bonding strength was also enhanced by EA rapid heat treatment. A higher current density of 190 A/mm^2 resulted in a premature fracture of the ACS sheet due to an early interfacial debonding caused by the thick IMC layer during the tensile test. The fracture modes of the matrix-dominated fracture and interfacial IMC-dominated fracture were determined based on observations from DIC tests and SEM fracture surfaces. The U-shape forming test confirmed that the desired formability can be attributed to the changes in the IMC caused by applying the four pulses treatment under a relatively low current density, rather than using a higher current density.

The present study suggested that EA rapid heat treatment is an effective method to balance the strength and ductility of the ACS sheet, which can notably improve the formability of the ACS sheet with a process time of a few seconds. The results of the present study are expected to contribute to the development of a cost-effective and efficient diffusion process for clad materials.

REFERENCES

[1] C. Wang, Y. Jiang, J. Xie, D. Zhou, X. Zhang, Interface formation and bonding mechanism of embedded aluminum-steel composite sheet during cold roll bonding, Materials Science and Engineering: A, 708 (2017) 50-59. https://doi.org/10.1016/j.msea.2017.09.111

[2] C. Wang, Y. Jiang, J. Xie, D. Zhou, X. Zhang, Effect of the steel sheet surface hardening state on interfacial bonding strength of embedded aluminum–steel composite sheet produced by cold roll bonding process, Materials Science and Engineering: A, 652 (2016) 51-58. https://doi.org/10.1016/j.msea.2015.11.039

[3] H. Springer, A. Kostka, E.J. Payton, D. Raabe, A. Kaysser-Pyzalla, G. Eggeler, On the formation and growth of intermetallic phases during interdiffusion between low-carbon steel and aluminum alloys, AcMat, 59 (2011) 1586-1600. https://doi.org/10.1016/j.actamat.2010.11.023

[4] F. Yin, J. Ma, B. Liu, J. He, F. Zhang, M. Liu, et al. Microstructure and Mechanical Properties of Aluminum Clad Steel Plates by Cold Rolling and Annealing Heat Treatment, in: Advances in Materials Processing, 2018, pp. 655-665. https://doi.org/10.1007/978-981-13-0107-0_61

[5] H.R. Akramifard, H. Mirzadeh, M.H. Parsa, Cladding of aluminum on AISI 304L stainless steel by cold roll bonding: Mechanism, microstructure, and mechanical properties, Materials Science and Engineering: A, 613 (2014) 232-239. https://doi.org/10.1016/j.msea.2014.06.109

[6] L. Li, K. Nagai, F. Yin, Progress in cold roll bonding of metals, Sci Technol Adv Mater, 9 (2008) 023001. https://doi.org/10.1088/1468-6996/9/2/023001

[7] E.-W. Jeong, K.N. Hui, D.-H. Bae, D.-S. Bae, Y.-R. Cho, Identification of the intermetallic compound layer formed at the interface of roll-bonded aluminum-clad steel by

thermal annealing, Metals and Materials International, 20 (2014) 499-502. https://doi.org/10.1007/s12540-014-3013-6

[8] C.-y. Wang, Y.-b. Jiang, J.-x. Xie, S. Xu, D.-j. Zhou, X.-j. Zhang, Formation mechanism and control of aluminum layer thickness fluctuation in embedded aluminum–steel composite sheet produced by cold roll bonding process, Transactions of Nonferrous Metals Society of China, 27 (2017) 1011-1018. https://doi.org/10.1016/S1003-6326(17)60118-3

[9] S. Zhang, K. Gao, S.-T. Hong, H. Ahn, Y. Choi, S. Lee, et al. Electrically assisted solid state lap joining of dissimilar steel S45C and aluminum 6061-T6 alloy, Journal of Materials Research and Technology, 12 (2021) 271-282. https://doi.org/10.1016/j.jmrt.2021.02.091

[10] J. Wang, A. Misra, An overview of interface-dominated deformation mechanisms in metallic multilayers, Current Opinion in Solid State and Materials Science, 15 (2011) 20-28. https://doi.org/10.1016/j.cossms.2010.09.002

[11] Hirth JP. The influence of grain boundaries on mechanical properties. Metall Trans 1972;3:3047–67. https://doi.org/10.1007/BF02661312

[12] M. Talebian, M. Alizadeh, Manufacturing Al/steel multilayered composite by accumulative roll bonding and the effects of subsequent annealing on the microstructural and mechanical characteristics, Materials Science and Engineering: A, 590 (2014) 186-193. https://doi.org/10.1016/j.msea.2013.10.026

[13] Y. Yang, F. Zhang, J. He, Y. Qin, B. Liu, M. Yang, et al. Microstructure, growth kinetics and mechanical properties of interface layer for roll bonded aluminum-steel clad sheet annealed under argon gas protection, Vacuu, 151 (2018) 189-196. https://doi.org/10.1016/j.vacuum.2018.02.018

[14] H.-J. Jeong, J.-w. Park, K.J. Jeong, N.M. Hwang, S.-T. Hong, H.N. Han, Effect of Pulsed Electric Current on TRIP-Aided Steel, International Journal of Precision Engineering and Manufacturing-Green Technology, 6 (2019) 315-327. https://doi.org/10.1007/s40684-019-00060-1

[15] M.-J. Kim, M.-G. Lee, K. Hariharan, S.-T. Hong, I.-S. Choi, D. Kim, et al. Electric current–assisted deformation behavior of Al-Mg-Si alloy under uniaxial tension, Int. J. Plast., 94 (2017) 148-170. https://doi.org/10.1016/j.ijplas.2016.09.010

[16] T.A.N. Nguyen, H. Choi, M.-J. Kim, S.-T. Hong, H.N. Han, Evaluation of Efficiency of Electrically Assisted Rapid Annealing Compared to Rapid Induction Heat Treatment, International Journal of Precision Engineering and Manufacturing-Green Technology, (2021). https://doi.org/10.1007/s40684-021-00382-z

[17] J.-W. Park, H.-J. Jeong, S.-W. Jin, M.-J. Kim, K. Lee, J.J. Kim, et al. Effect of electric current on recrystallization kinetics in interstitial free steel and AZ31 magnesium alloy, Materials Characterization, 133 (2017) 70-76. https://doi.org/10.1016/j.matchar.2017.09.021

[18] H.-J. Jeong, M.-J. Kim, S.-J. Choi, J.-W. Park, H. Choi, V.T. Luu, et al. Microstructure reset-based self-healing method using sub-second electric pulsing for metallic materials, Applied Materials Today, 20 (2020). https://doi.org/10.1016/j.apmt.2020.100755

[19] G.D. Park, V.L. Tran, S.-T. Hong, Y.-H. Jeong, T.S. Yeo, M.J. Nam, et al. Electrically assisted stress relief annealing of automotive springs, Journal of Mechanical Science and Technology, 31 (2017) 3943-3948. https://doi.org/10.1007/s12206-017-0740-x

[20] K.-A. Dinh, S.-T. Hong, T.V. Luu, M.-J. Kim, H.N. Han, Intermetallic Evolution of Al–Si-Coated Hot Stamping Steel During Modified Electrically Assisted Rapid Heating, Acta

Metallurgica Sinica (English Letters), 31 (2018) 1327-1333. https://doi.org/10.1007/s40195-018-0740-6

[21] G. Chen, J.-T. Li, G.-M. Xu, Improvement of Bonding Strength of Horizontal Twin-Roll Cast Steel/Aluminum Clad Sheet by Electromagnetic Fields, Acta Metallurgica Sinica (English Letters), 31 (2017) 55-62. https://doi.org/10.1007/s40195-017-0633-0

[22] M.-J. Kim, S. Yoon, S. Park, H.-J. Jeong, J.-W. Park, K. Kim, J. Jo, T. Heo, S.-T. Hong, S.H. Cho, Y.-K. Kwon, I.-S. Choi, M. Kim, H.N. Han, Elucidating the origin of electroplasticity in metallic materials, Applied Materials Today, 21 (2020).

[23] M. Cao, C.-j. Wang, K.-k. Deng, K.-b. Nie, W. Liang, Y.-c. Wu, Effect of interface on mechanical properties and formability of Ti/Al/Ti laminated composites, Journal of Materials Research and Technology, 14 (2021) 1655-1669. https://doi.org/10.1016/j.jmrt.2021.07.021

[24] B.X. Li, Z.J. Chen, W.J. He, P.J. Wang, J.S. Lin, Y. Wang, et al. Effect of interlayer material and rolling temperature on microstructures and mechanical properties of titanium/steel clad plates, Materials Science and Engineering: A, 749 (2019) 241-248. https://doi.org/10.1016/j.msea.2019.02.018

[25] Z. Zhang, W. Xu, T. Gu, D. Shan, Fabrication of steel/aluminum clad tube by spin bonding and annealing treatment, The International Journal of Advanced Manufacturing Technology, 94 (2017) 3605-3617. https://doi.org/10.1007/s00170-017-1119-y

[26] Y. Wang, K.S. Vecchio, Microstructure evolution in a martensitic 430 stainless steel–Al metallic–intermetallic laminate (MIL) composite, Materials Science and Engineering: A, 643 (2015) 72-85. https://doi.org/10.1016/j.msea.2015.07.014

[27] H. Danesh Manesh, A. Karimi Taheri, The effect of annealing treatment on mechanical properties of aluminum clad steel sheet, Materials & Design, 24 (2003) 617-622. https://doi.org/10.1016/S0261-3069(03)00135-3

CHAPTER III

PROLONGED FATIGUE LIFE IN ALUMINUM CLAD STEEL BY ELECTROPULSING TREATMENT: RETARDATION OF INTERFACE-MICROCRACK FORMATION

3.1 INTRODUCTION

Aluminum (Al) clad steel (ACS), a two-layer laminated metal sheet combining the individual advantages of each constituent material (lightweight, good corrosion resistance, and high thermal conductivity of aluminum; high strength of steel) is expected to be used for fabricating battery cases of the electric vehicles [1-5]. ACS components are usually subjected to complicated working conditions related to high temperature, cyclic loading, and corrosion. Among them, fatigue failure could be one of the most critical failure modes during service. Moreover, the interface of multi-layer materials influences the monotonic and cyclic mechanical properties because of the significant differences in the yield strength, elastic modulus, ultimate tensile strength, and elongation of the constituent layers [6,7]. Under cyclic loading, the initiation and propagation of the cracks formed at the interface are the essential factors affecting the fatigue life of multi-layer materials. Therefore, understanding the crack initiation mechanism and finding an approach to suppress the initiation and propagation of the interfacial cracks are crucial for extending the service life of ACS sheets.

During the past decades, only a few works focused on the fatigue behavior of multi-layer materials from a microstructural perspective. Most of them investigated the effect of the manufacturing process or layer architecture on the fatigue performance of the multi-layer sheets. Lamik et al. [8] studied the fatigue behavior of cold roll bonded Al6016 and FeP06.

They reported that the cyclic hardening behavior of the FeP06 has a remarkable effect on the fatigue life of the fabricated Al clad steel compound. Kummel et al. [9] designed and manufactured ultrafine-grained Al/steel laminated metal composites by the accumulative roll bonding process. They stated that the fatigue life could be dramatically increased by varying the position of the steel layer. Li et al. [10] fabricated soft/hard copper/bronze laminates with transition interfaces and superior mechanical properties using three processing steps: diffusion welding, cold rolling, and annealing. The superior combination of strength and ductility of the soft/hard copper/bronze laminates was primarily attributed to the back-stress strengthening induced by the well-bonded interface. Huang et al. [11,12] reported that the improved mechanical properties of the soft/hard laminates were primarily related to the stress partition and strain transfer between soft and hard layers.

In high cycle fatigue, the crack initiation related to the accumulation of dislocations and microcrack nucleation and coalescence dominate the fatigue period. Microstructural changes in fatigue tests of metallic materials are strongly related to the crystal orientation, which can be observed by electron backscatter diffraction (EBSD) analysis. Therefore, the EBSD technique has been used as a damage indicator to describe the damage evolution and to predict crack initiation during the fatigue test [13-19]. Schayes et al. [13] pointed out that kernel average misorientation (KAM) and grain reference orientation deviation (GROD) maps can be used to reveal the localization of the deformation at grain boundaries of Fe-3Si steel in fatigue tests, which enables the prediction of intergranular crack initiation due to the stress concentration. Wang et al. [16] investigated creep fatigue based on the diffraction-based misorientation mapping and its correlation to macroscopic damage evolution. Bouquerel et al.

[18] carried out a mesoscopic investigation of the local cyclic plasticity on notched Fe-3%Si steel subjected to fatigue loading by the EBSD technique.

During electropulsing treatment (or electrically assisted heat treatment), in addition to the well-known thermal effect by resistance heating, the athermal effect of electric current (so called electroplastic effect) can additionally weaken the atomic bonding by inducing a charge imbalance near defects, as revealed by Kim et al. [20]. Therefore, the annealing [21], recrystallization [22], and aging [23] during electropulsing treatment can be significantly enhanced in comparison to conventional furnace heat treatment. Moreover, Jeong et al. [24] proposed a microstructural self-healing method using a sub-second electric pulse during cyclic tensile tests of SUS301L and SUS316L. They found that the electric pulse enhanced the kinetics of microstructural changes to reset the damaged microstructure of the selected materials and significantly increased the elongation at fracture.

For healing fatigue-induced damage in homogeneous metal alloys, several researchers reported that the electric pulse is an effective method to restore the microstructural damage and close the initiated microcracks, even though the suggested healing mechanisms of fatigue-induced damage were slightly different depending on the experimental conditions. Tang et al. [25] investigated the restoration of the fatigue damage in stainless steel by high-density electric current. They concluded that the delayed fatigue crack initiation was the result of a decrease in the dislocation density, which was characterized by transmission electron microscopy. Jung et al. [26] attributed the delay of crack propagation to the crack-shielding effect resulting from current-induced local melting. Yang et al. [27] found that selective heating and thermal compressive stress around the cracks led to void healing when an electric pulse was applied to damaged samples.

Although several researchers have reported prolonged fatigue life resulting from the reduced dislocation density and the closed cracks through electropulsing treatment for homogeneous metal alloys, prolonging the fatigue life of multi-layer materials by electropulsing treatment has rarely been reported. In comparison with homogeneous metal alloys, the fatigue damage evolution of multi-layer materials, including the ACS, can be much more complicated due to the stress redistribution and the strain transfer between different layers during the test. Therefore, investigating the fatigue damage evolution of the ACS sheet and the healing mechanism by electropulsing treatment can be crucial for engineering applications of multi-layer materials.

In the present study, the fatigue damage evolution of the ACS sheet was investigated by scanning electron microscope (SEM) images and EBSD observations from samples that suffered different fatigue cycles. In addition, the prolonged fatigue life by electropulsing treatment was demonstrated by comparing the microstructural change between electropulsing treated samples and untreated samples.

3.2 EXPERIMENTAL SET-UP

3.2.1 Material preparation

Mild steel (PosACC) and Al alloy 1050 (Al1050) sheets with identical thicknesses of 1.5 mm were stacked together and solid-state joined by the cold roll bonding (CRB) technique after surface cleaning. The chemical compositions of the mild steel and Al1050 are listed in Table 3.1. After joining, the ACS sheet was heat-treated in a conventional furnace (600 °C, 30 hrs) to enhance the metallurgical bonding between the steel substrate layer and the Al1050 clad layer. As shown in Fig. 3.1, different thicknesses for each corresponding layer (steel: 0.4

mm; Al1050: 0.3 mm) were obtained after joining and heat treatment. The heat-treated ACS sheet was used as the base material (BM) for the subsequent monotonic tension and fatigue tests.

Table 3.1. Chemical compositions of the raw materials (wt%)

Elements	Fe	Al	C	Si	Mn	P	S	Cu	Ti
Mild steel	Bal.	-	0.002	-	0.219	0.006	0.005	-	-
Al1050	0.702	Bal.	-	0.603	-	-	-	0.001	0.016

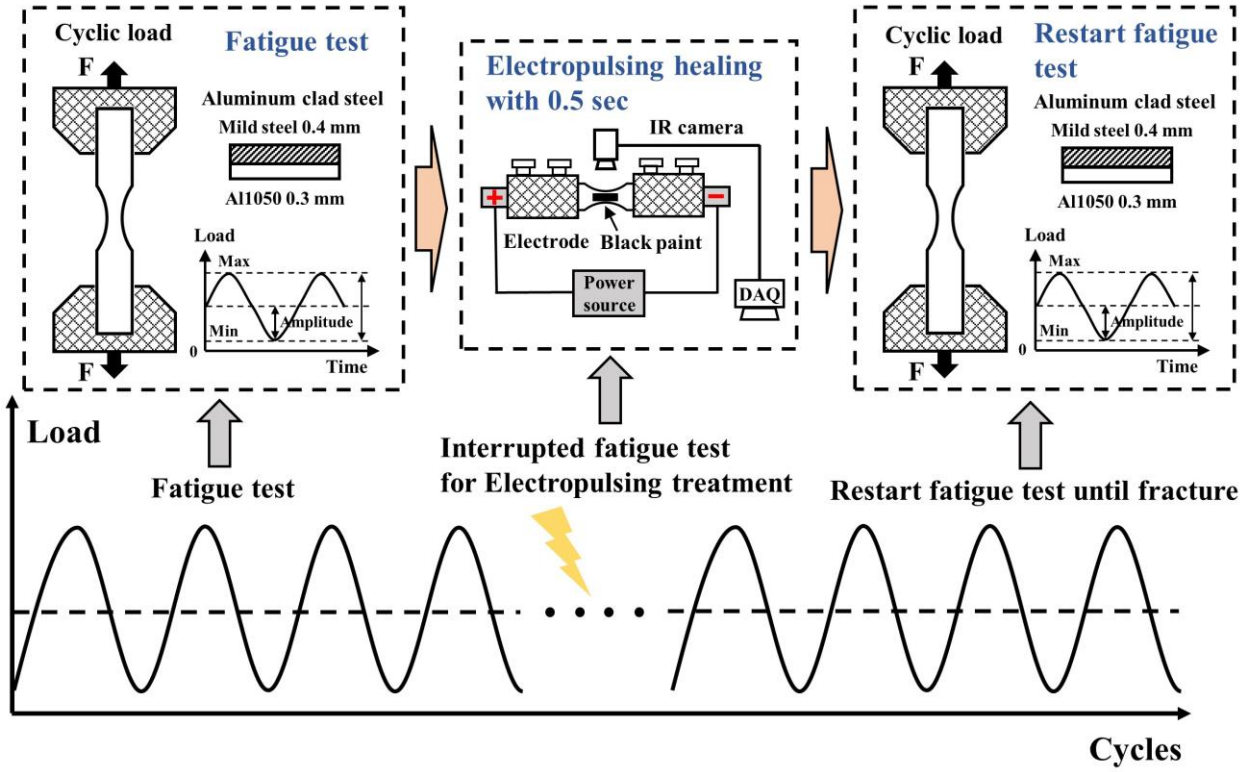

Fig. 3.1. Experimental process of the fatigue life enhancement

3.2.2 Monotonic tension test and force-controlled axial fatigue test

The mechanical properties of the BM ACS sheet were determined by a monotonic tension test on a universal testing machine with a constant displacement rate of 0.5 mm/min. Tensile specimens (ASTM E8/E8M) were prepared in the rolling direction of the sheet with a gauge length of 32 mm and a width of 6 mm, as illustrated in Fig. 3.2(a). During the tensile test, the strain variation of both the steel and Al1050 layers was monitored by an ARAMIS digital image correlation (DIC) system (GOM, Germany) to identify the incompatible deformation on different layers, while the displacement history was recorded using an LX500 laser extensometer (MTS, USA). Three samples were tensile tested to verify the repeatability.

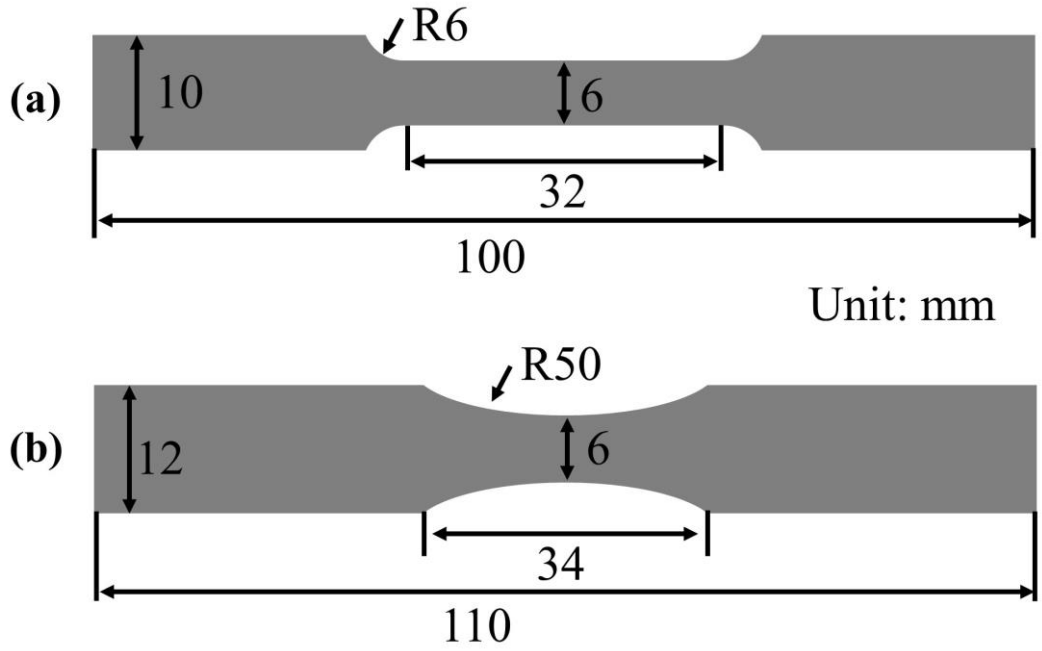

Fig. 3.2. Dimensions of the samples for (a) monotonic tension and (b) fatigue

Force-controlled constant amplitude axial fatigue tests were conducted using a servo-hydraulic fatigue machine (MTS-322, MTS, USA) to assess the fatigue performance of the ACS sheet. The dimensions of the samples (ASTM E466) used in the fatigue test are shown in

Fig. 3.2(b). The load frequency (F) and stress ratio (R) were 20 Hz and 0.1, respectively, throughout the entire fatigue tests. In addition, 5 million cycles without fracture were considered to be the fatigue limit in the present study. Also, specimens for microstructural analysis to assess the evolution of fatigue-induced damage were prepared by stopping the fatigue tests with a maximum stress (σ_{max}) of 245 MPa at different fatigue cycles.

3.2.3 Prolonging fatigue life by electropulsing treatment

For prolonging fatigue life by electropulsing treatment, the fatigue test was stopped at 0.7 times failure life for each corresponding fatigue loading condition with σ_{max}=255, 245, and 235 MPa. Then, the electric pulse with a current density of 150 A/mm^2 and a duration of 0.5 sec was applied to the fatigued samples to prolong the fatigue life by restoring the damaged microstructure, as schematically exhibited in Fig. 3.1. After electropulsing treatment, the sample was cooled down to room temperature in air, and then the fatigue test was restarted until fracture. The electric pulse generated by a controllable generator (SP-1000U, Hyosung, South Korea) was used to induce rapid resistance heating and the athermal effect of the electric current. The combined thermal and athermal effects that acted as external driving forces were considered to reduce the fatigue damage (micro-cracks or dislocation density). Thus, the fatigue life of the ACS sheet can be improved by healing the microstructural damage. The temperature of the fatigued sample was recorded by an infrared thermal imaging camera (FLIR-T621, FLIR, Sweden) during the electropulsing treatment.

3.2.4 Microstructure observation

The interrupted samples were cross-sectioned along the loading direction at the minimum width area, while the fractured samples were examined on the fracture surface perpendicular to the loading direction. The cross-sections were ground and polished following

the standard metallographic preparation for the microstructural observation. The macro-morphology of the interface between the substrate and clad layers was first obtained by SEM, and the quantitative assessment of the interfacial diffusion thicknesses between the steel and Al1050 were determined by an energy dispersive spectrometer (EDS: X-Max 50, Horiba, Japan). In EBSD analysis, a step size of 1.2 μm and a working distance of 15 mm were used, while the accelerating voltage, probe current, and tilt angle were set to 20 eV, 14 nA, and 70°, respectively. The grain size, inverse pole figure (IPF) maps, image quality (IQ) maps with grain boundaries, and kernel average misorientation (KAM) maps were obtained by an electron backscatter diffractometer (EBSD: TSL Hikari Super, TSL, USA) to understand the damage evolution of the ACS sheet under cyclic loading. In IQ maps, the misorientation angle of 2–15° was defined as the low angle grain boundary (LAGB), while the high angle grain boundary (HAGB) was defined as angles greater than 15°.

3.2.5 Microhardness test

The Vickers hardness on each constituent layer before and after electropulsing treatment was measured using a Vickers indenter (HM-200, Mitutoyo, Japan) under conditions of 0.5 N for 10 sec on the Al1050 side and 2 N for 10 sec on the steel side.

3.3 RESULTS

3.3.1 Microstructure characterization of the BM ACS sheet

A continuous and straight morphology for each corresponding layer was observed after cold rolling and subsequent heat treatment, as presented in Fig. 3.3(a). It is well known that steel is much harder than Al1050, so the thickness reduction of the Al1050 layer was higher than that of the steel layer. The substrate layer of mild steel with a thickness of about 0.4 mm

and the clad layer of Al1050 with a thickness of about 0.3 mm were well bonded without forming macrocracks or voids at the interface. The initial microstructure (Fig. 3.3(b)) of the BM ACS sheet characterized by EBSD showed that both steel and Al1050 (especially, the steel substrate layer) are recrystallized after annealing with randomly distributed grain orientations.

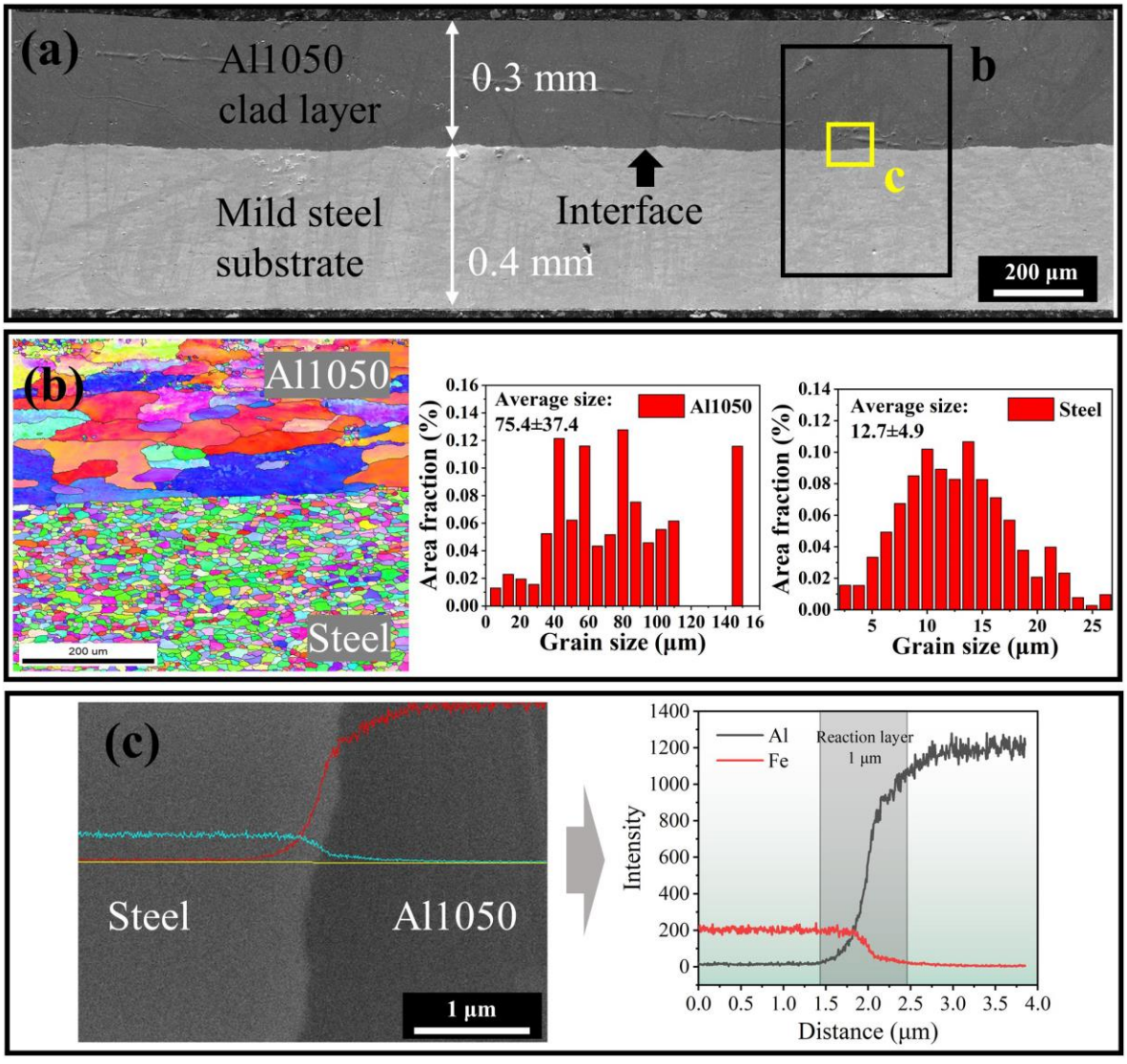

Fig. 3.3. Microstructural observation of the BM ACS: (a) SEM morphology, (b) IPF map and the relevant grain size distribution, and (c) EDS-line scan across the interface

Equiaxed grain shape with an average grain size of 12.7 ± 4.9 μm in steel layer was observed, while the Al1050 layer exhibited a slightly elongated grain shape along the rolling direction with a much coarser grain size of 75.4 ± 37.4 μm, as shown in the IPF map and the histogram of grain size distribution in Fig. 3.3(b). Also, the EBSD IPF map of the entire observational area shows that a large grain gradient formed at the interface between the Al1050 and steel layers. The result of the SEM-EDS line scan (Fig. 3.3(c)) suggested that a solid-state interface with a diffusion thickness of approximately 1 μm was formed between the Al1050 and the steel layers after cold roll bonding and heat treatment.

3.3.2 Monotonic tensile properties

The engineering stress-strain curves (Fig. 3.4(a)) of the BM ACS sheet show a yield strength of approximately 255 MPa and an elongation of 12% in the rolling direction. Also, as shown in the inset of Fig. 3.4(a), the specimen fractured at 45° relative to the loading direction. It should be noted that the BM ACS sheet is a laminated metal composite, so the stress can be estimated by the simple rule-of-mixture (ROM) using the equation $\sigma=\sigma_{Al}V_{Al}+\sigma_{steel}V_{steel}$. Here, σ and V are the stress and the volume fraction, respectively. The subscripts Al and steel indicate the Al clad layer and the steel substrate layer, respectively. However, the predicted mechanical properties using ROM are lower than the experimental observation. The ultimate tensile strengths (UTS) of the annealed mild steel and Al1050 are 343 MPa and 76 MPa, respectively. Using ROM, the predicted UTS for the BM ACS sheet is expected to be 228.5 MPa. This discrepancy suggests that there is an additional mechanical strengthening effect in the interface during deformation. Back stress (σ_b), as a type of long-range stress due to the mechanical incompatibility of the constituent layers, was reported to play an important role in additional strengthening of laminated composites [28,29]. To quantitatively evaluate the effect

of the back stress, the loading-unloading-reloading (LUR) test was performed five times with a true strain interval of about 2%, as exhibited in Fig. 3.4(b). The calculation method of the back stress and the results are summarized in Fig. 3.4(c). Note that σ_r and σ_u are the yield stress during loading and unloading, respectively, while E is the elastic modulus (considered to be the same as the initial value). The results show that the back stress even increases with an increase in the true strain and provides high back stress hardening during continuous plastic deformation. The gradually increased back stress indicates that the transition interface can maintain the incompatible plastic deformation without interfacial delamination.

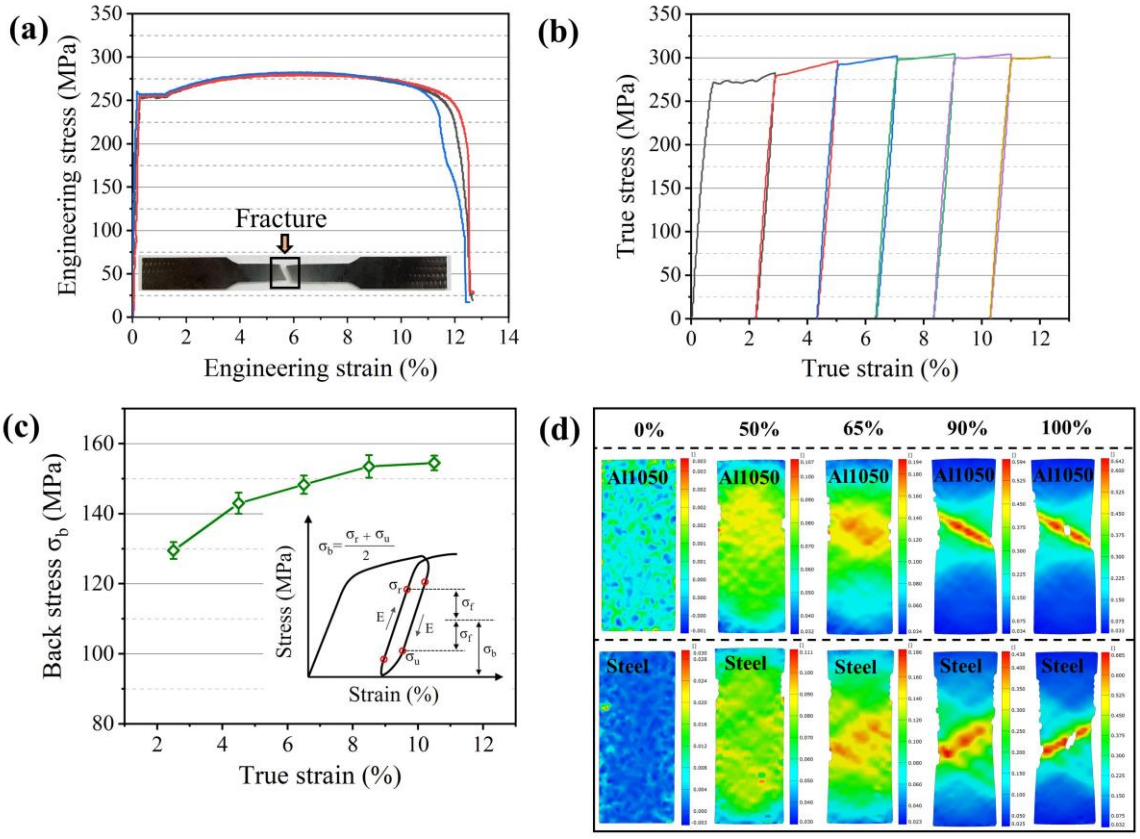

Fig. 3.4. Monotonic tensile results of the BM ACS: (a) tensile stress-strain curve, (b) loading-unloading-reloading curve, (c) the calculated back stress, and (d) strain distribution by DIC test

To determine the failure process of the ACS sheet under the monotonic tension test, the strain distribution (Fig. 3.4(d)) measured by the DIC test for each layer was mapped at elongations of 0%, 50%, 65%, 90%, and 100% of the elongation at fracture. As shown in the figure, at the 50% of the elongation at fracture, a distinct strain concentration can be found in the Al1050 layer, while the steel layer exhibited a more uniform deformation. As plastic deformation increased to the 65% of the elongation at fracture, many discrete shear bands were developed at about 45° to the loading direction. A predominant shear band formed as a combination of many discrete shear bands at the 90% of the elongation at fracture for both the Al1050 and steel layers. Intriguingly, an early combination with high strain amplitude can be found in the Al1050 layer due to the incompatibility of plastic formation. Finally, the ACS sheet fractured at about 45° to the loading direction.

3.3.3 Damage and failure mechanism under cyclic loading

The fatigue life distribution as a function of the maximum stress in Fig. 3.5 shows a natural increase with the change of cyclic stress from σ_{max}=255 MPa to σ_{max}=210 MPa. The stress was calculated by dividing the entire cross-section of the fatigue sample without considering the load transfer between the steel and Al1050 layers. The stress of 210 MPa under the fatigue condition of R=0.1 was defined as the fatigue limit in the present study, since the samples suffered 5 million cycles without fracture. A representative stress of 245 MPa was used to investigate the failure mechanism by observing the interfacial evolution from different fatigue cycles. As shown in Fig. 3.5, the average fatigue life under the cyclic stress of σ_{max}=245 MPa and R=0.1 is about 350,000 cycles. The samples subjected to cyclic stress of σ_{max}=245 MPa and R=0.1 were interrupted at cycles of 0, 150,000, 250,000, and their interfaces were characterized by SEM. A qualitative description of the interfacial damage

features (Fig. 3.6(a)) with respect to the different fatigue cycles showed that an interfacial crack was initiated at 150,000 cycles and gradually propagated to the Al1050 side perpendicular to the loading direction as the fatigue cycles increased to 250,000. Note that the interfacial cracks were not detected in the BM samples. In addition, the fracture surfaces (Fig. 3.6(b)) revealed that the interfacial delamination occurred and resulted in sudden ductile fracture features for both Al1050 and steel layers at the final stage.

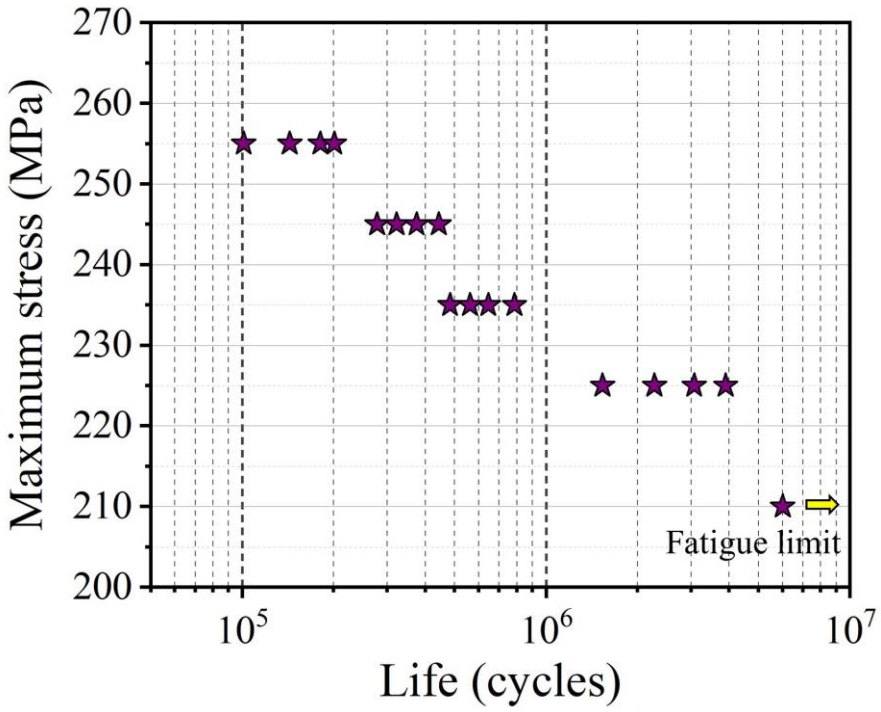

Fig. 3.5. Discrete fatigue life at different stress levels

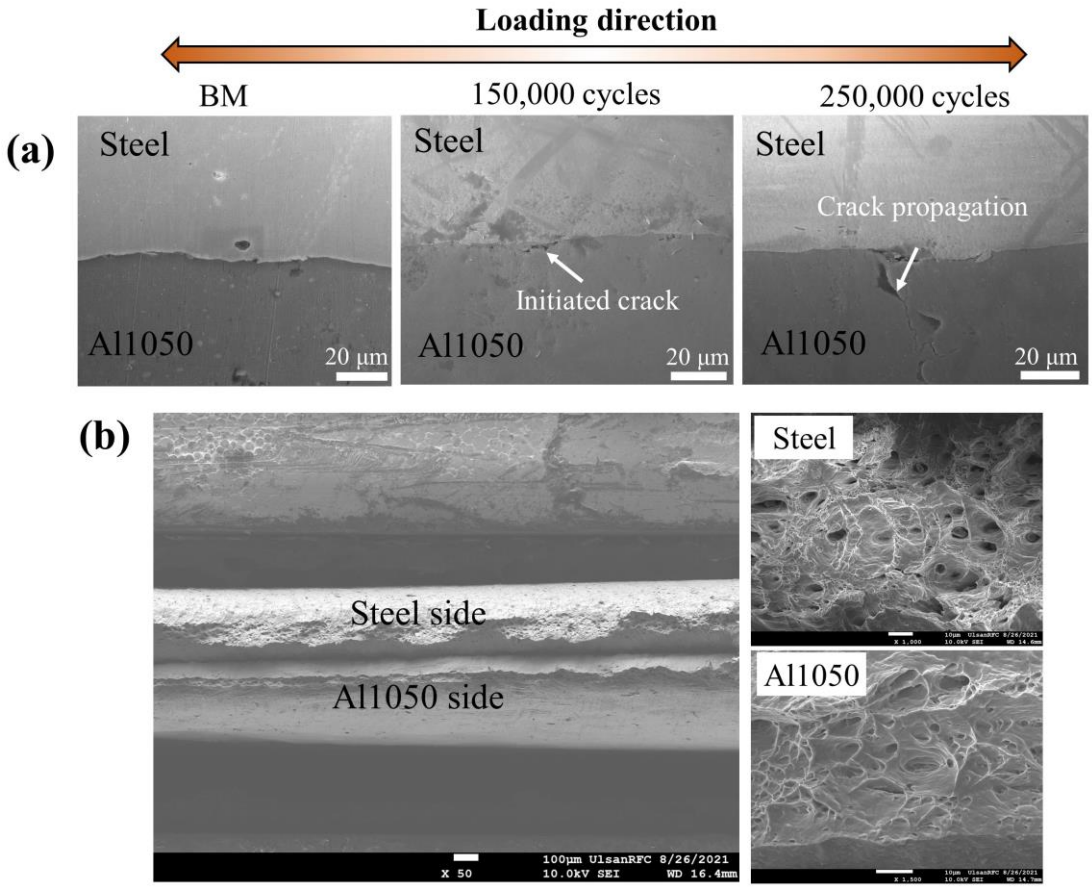

Fig. 3.6. The fatigue failure process for maximum stress of 245 MPa: (a) SEM image of interface along the loading direction at different fatigue ratios and (b) fracture surface perpendicular to the loading direction

The EBSD observations from the samples suffered different fatigue cycles under cyclic stress of σ_{max}=245 MPa and R=0.1 (Figs. 3.7 and 3.8) provided evidence of the progressive microstructural changes, which can be used to evaluate the fatigue damage evolution and predict the crack formation. The microstructures of the BM, 150,000 cycled, 250,000 cycled, and fractured samples were characterized to investigate the failure mechanism of the ACS sheet under cyclic loading. The IPF maps (Fig. 3.7(a)) show that the Fe grains

were distinctly elongated along the loading direction, while Al grains showed nearly no change up to 250,000 cycles. Al grains finally exhibited a deformed shape in the fractured sample along with further elongated and distorted Fe grains. The KAM maps are the reflection of the dislocation density and were used to describe the fatigue damage evolution, as presented in Figs. 3.7(a)-(c). The average KAM values for the entire observational area and each constituent layer (Figs. 3.7(b) and (c)) were also presented to reveal the deformation differences on different layers during cyclic loading. In general, averaged KAM values progressively increased with the increase of the fatigue cycle, as suggested in Figs. 3.7(a) and (b). However, the KAM value of the Al1050 layer had no pronounced increase up to 150,000 cycles, while the steel layer showed a progressive increase in the KAM value from the early stage to the fracture. These differences indicate that the Al1050 has not been plastically deformed at the early fatigue cycles due to the transformation of the applied stress to the harder steel layer. At 250,000 cycles, significantly increased KAM values can be observed in both Al1050 and steel layers. Note that the dislocations preferred to form and pile up in the interior of the Al grains and at the grain boundaries of the Fe grains, as shown in Fig 3.7(a).

IQ maps overlaid with grain boundaries (Fig. 3.8(a)) show that there is no noticeable change in the fraction of the grain boundaries up to 150,000 cycles. At 250,000 cycles, an increase of the LAGBs was observed primarily at the interior of the Al grains near the interface. In fractured samples, the large volume fraction of LAGBs is eventually distributed throughout the steel and Al1050 layers. The increased volume fraction of the LAGBs is consistent with the increase in the fatigue cycles. The histograms of the misorientation angles (Figs. 3.8(b)-(e)) for the entire observational area agree well with the IQ maps, showing an increased volume fraction of the LAGBs. Also, the gradually decreased average value of the

misorientation angles indicates a progressive accumulation of the fatigue damage related to the evolution of the dislocation.

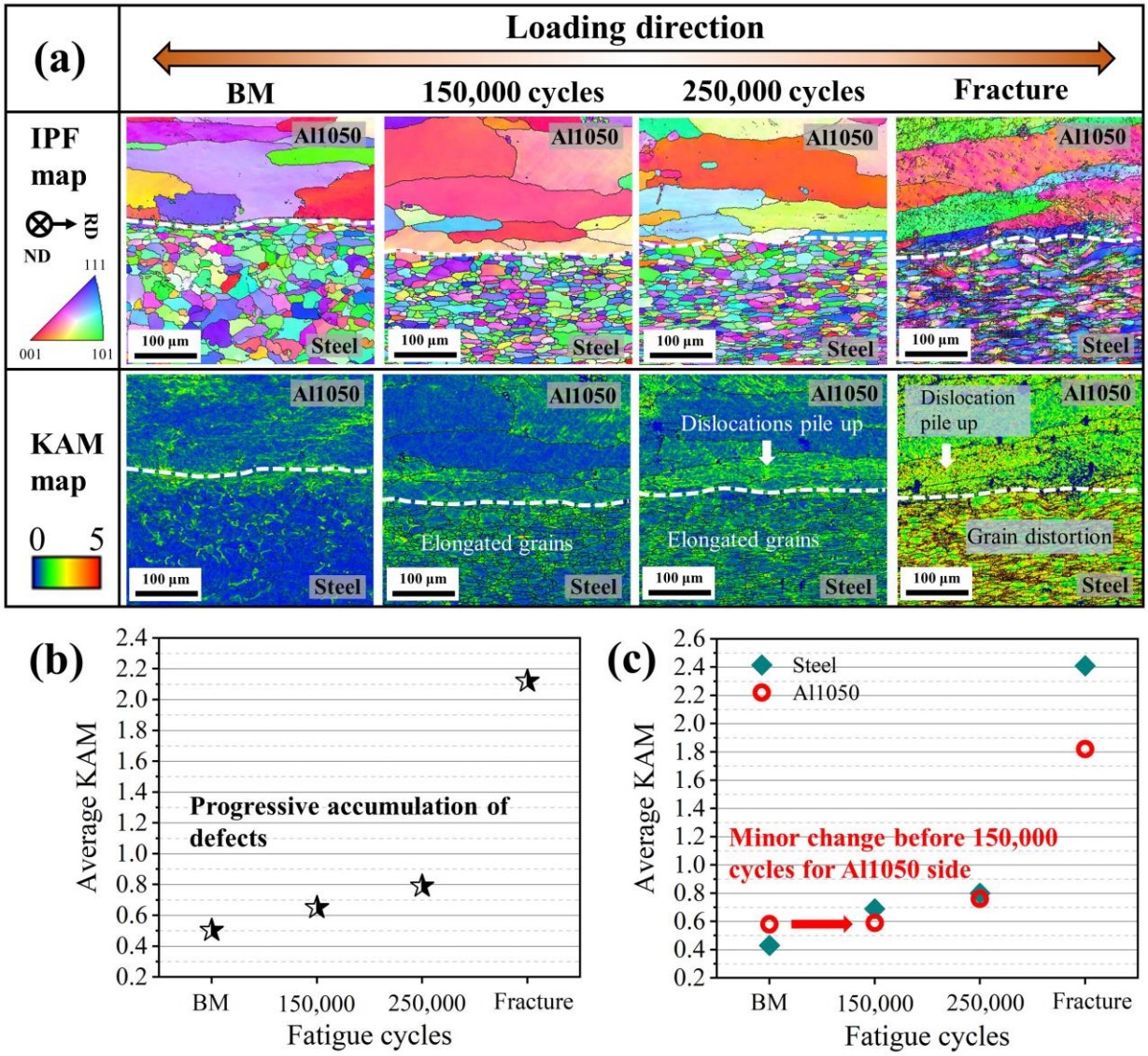

Fig. 3.7. The evolution of the EBSD results for maximum stress of 245 MPa: (a) IPF and KAM maps, (b) the averaged KAM value for entire observational area, and (c) the averaged KAM value for each constituent layer. RD indicates rolling direction; ND indicates normal direction.

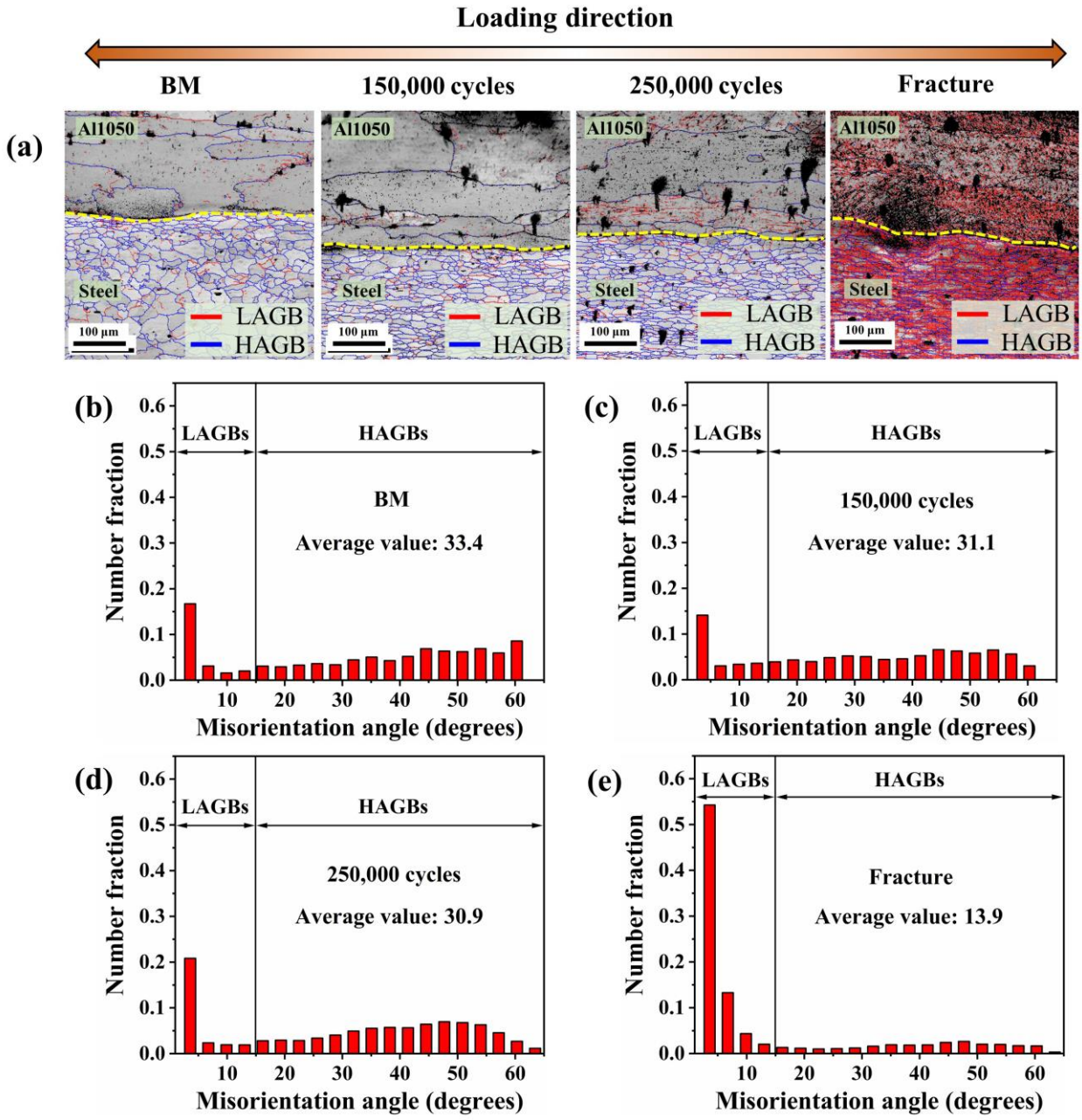

Fig. 3.8. The evolution of the EBSD results for maximum stress of 245 MPa: (a) IQ maps overlaid with grain boundaries and (b-e) histograms of misorientation angles

3.3.4 Prolonged fatigue life by electropulsing treatment

A peak temperature of approximately 350 °C (Fig. 3.9(a)) was reached during electropulsing treatment under 150 A/mm^2 for 0.5 sec. The comparison of the fatigue life before and after electropulsing treatment (Fig. 3.9(b)) shows that the fatigue life was significantly enhanced by electropulsing treatment (red circle symbol) compared to the BM life (purple star symbol) at σ_{max}=245 and 235 MPa. However, the overlapped fatigue life for σ_{max}=255 MPa indicates that the prolonging of the fatigue life by electropulsing treatment is not obvious due to the high deformation for each cycle. Note that the yield stress of the BM ACS sheet is about 255 MPa.

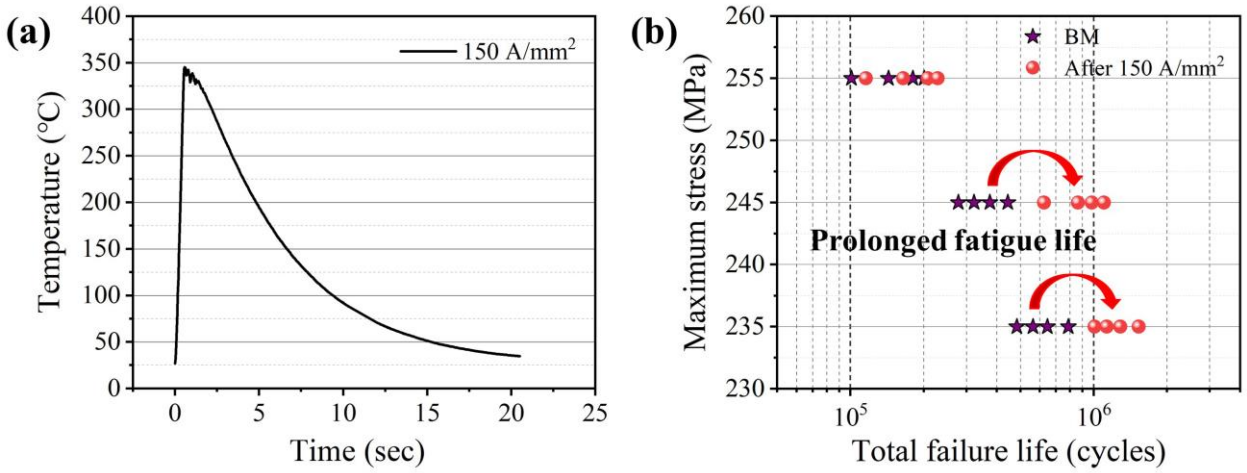

Fig. 3.9. Enhancement of the fatigue life by electropulsing treatment: (a) temperature histories during the application of the electric pulse and (b) enhanced fatigue life compared with the corresponded original fatigue life

The microhardness measurement was performed on samples of BM, 250,000 cycles, and 250,000 cycles with electropulsing treatment under a representative fatigue condition of

σ_{max}=245 MPa and R=0.1. The microhardness change (Fig. 3.10) shows that there is no notable change for either the Al1050 or steel layers in any conditions, which indicates that the mechanical properties of the sample did not remarkably change after fatigue and electropulsing treatment. Therefore, the prolonged fatigue life should be attributed to the restoration of microstructure damage by the high-density electric pulse.

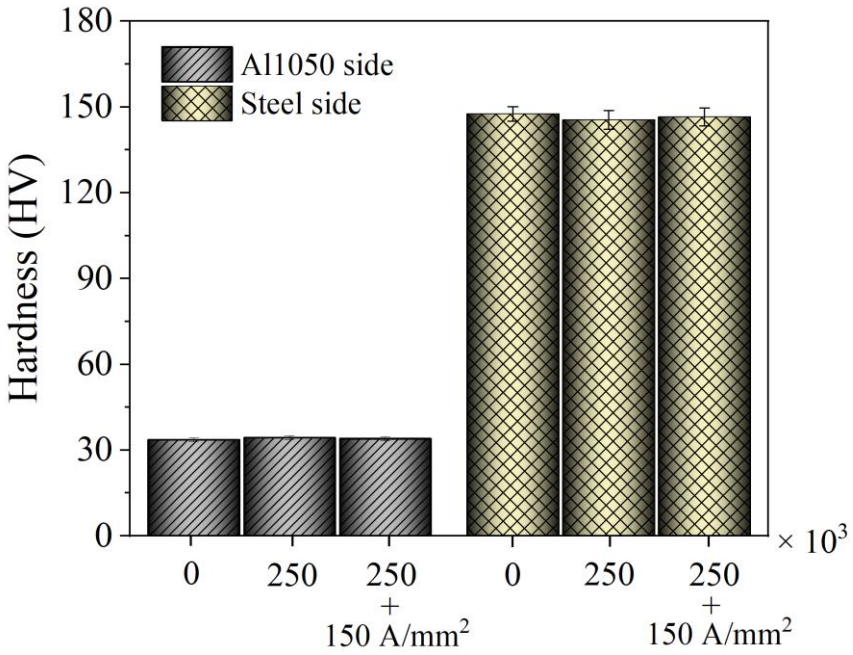

Fig. 3.10. Microhardness change for samples of BM, 250,000 cycles, and 250,000 cycles with electropulsing treatment under σ_{max}=245 MPa and R=0.1

To investigate the mechanism of prolonged fatigue life, a sample was electropulsing treated after 250,000 cycles under σ_{max}=245 MPa and R=0.1. The microstructure of the electropulsing treated sample was then compared with that of a sample, which only suffered the same number of fatigue cycles (no electropulsing treatment). The results of the IPF maps (Figs. 3.11(a) and (d)) show that the grain orientation and shape were not changed by

electropulsing treatment. The average KAM value of the steel layer decreased from 0.80 to 0.73, while the KAM value of the Al1050 layer decreased from 0.76 to 0.68 by electropulsing treatment (Figs. 3.11(b) and (e)). Before electropulsing treatment (Fig. 3.11(b)), a strain gradient induced by the dislocation pile-up can be found at the interface (especially for Al grains near the interface) due to the mechanical incompatibility of the constituent layers. This is also evidenced by the high density of LAGBs in Al grains near the interface (Fig. 3.11(c)). After electropulsing treatment, a noticeable reduction of the LAGBs related to the dislocation

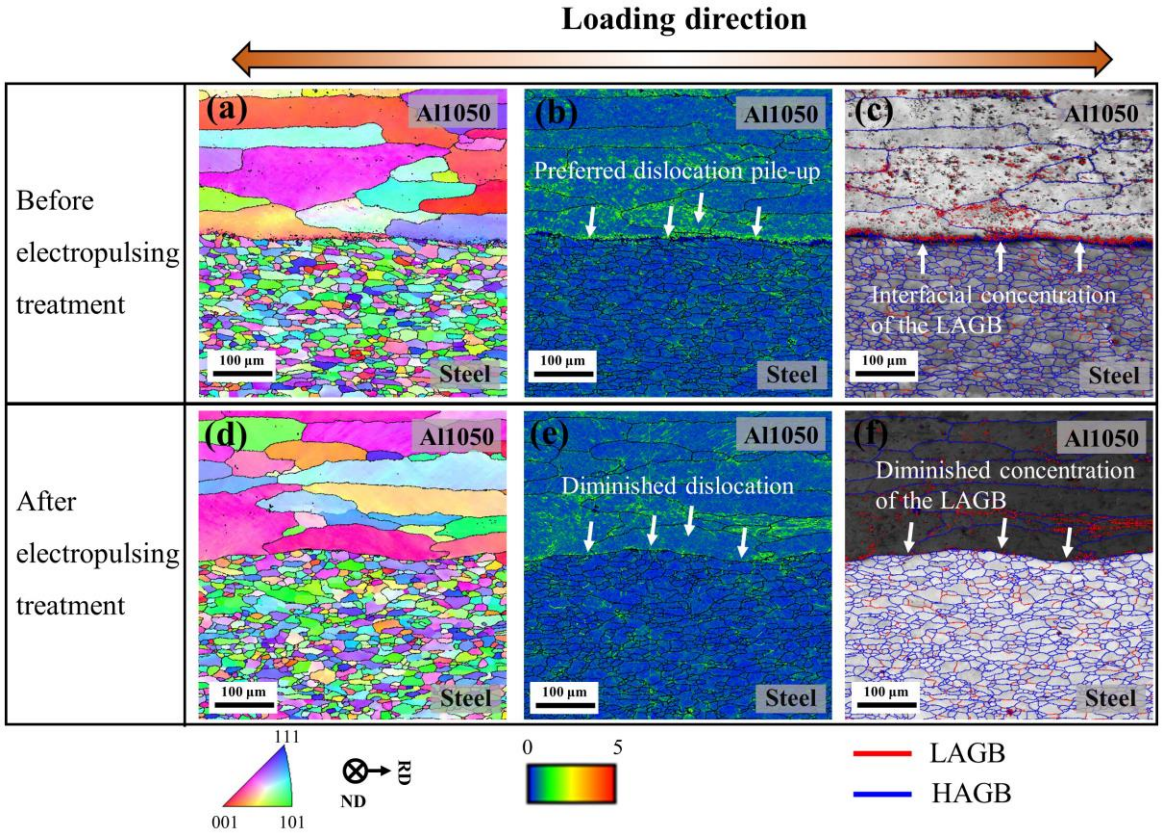

Fig. 3.11. Microstructural change before and after electropulsing treatment: (a) IPF map, (b) KAM map, and (c) IQ map overlaid with grain boundaries before electropulsing treatment; (d) IPF map, (e) KAM map, and (f) IQ map overlaid with grain boundaries after electropulsing treatment. RD indicates rolling direction; ND indicates normal direction.

annihilation in the Al1050 layer was observed (Fig. 3.11(f)). The reduced dislocation density is attributed to the combination of the thermal and athermal effects of the electric current [30]. The significantly enhanced fatigue life can be explained by dislocation annihilation near the interface, which reduced the chances of crack initiation.

3.4 DISCUSSION

As clearly shown in Fig. 3.4, the UTS of the ACS is much higher than that calculated by the ROM formula using the mechanical properties of the metal alloy for each layer, which is attributed to back stress strengthening. The long-range back stress was caused by the pile-up of the geometrically necessary dislocations (GNDs) due to the incompatible deformation of the constituent layers. The piled dislocation produces high back stress to compensate for the strength mismatch between the soft Al1050 layer and the hard steel layer. During the monotonic tension test of the ACS, the interface between steel and Al1050 acted as barriers that impeded the dislocation motion, resulting in the pile-up of GNDs at the interface, which induces the strain partitioning [29]. The strain gradient across the interface is further enlarged with an increase of the tensile displacement and progressively increases the back stress amplitude, which significantly increases the mechanical properties [29,31]. In addition to the observed back stress in the ACS sheet, gradient structure materials having a graded grain size can also enhance the back stress level due to the spatial distribution of the dislocation density [32]. In the present study, it is speculated that the large difference in grain size (Fig. 3.3(b)) between the Al1050 and the steel is attributed to the difference in recovery and recrystallization during the initial heat treatment process that can further increase the back stress level. Therefore, the combined effects of the large difference in the mechanical

properties and the grain size between steel and Al1050 synergistically enhanced the back stress strengthening and increased the mechanical properties of the ACS sheet.

Under the fatigue loading condition of σ_{max}=245 MPa and R=0.1, the steel layer was plastically deformed after 150,000 cycles, and this was associated with a noticeable increase in the averaged KAM value, as shown in Figs. 3.7(a) and (c). However, there was almost no change in either the grain shape or the averaged KAM value of the Al1050 layer for this number of cycles. This inconsistent change in grain shape and the averaged KAM value were the results of the stress redistribution due to the large difference in the mechanical properties between the Al1050 and the steel. The redistributed stress is more concentrated on the harder steel layer, resulting in premature yielding even when the applied stress is in the elastic region. Consequently, the grains for the steel layer were plastically deformed during the fatigue test and elongated along the loading direction to some extent at 150,000 cycles. At 250,000 cycles, the averaged KAM value of the Al1050 layer began to increase, while a continuous increase of the averaged KAM value was observed in the steel layer. It should be noted that a high density of local misorientation developed and accumulated at the interface of the interior of Al grains near the interface. This evolution resulted in a preferred dislocation pile-up at the interface and formed a strain gradient. In the meantime, the strain gradient promoted the dislocation multiplication and storage, resulting in a more complicated stress state at the interface and activation of more slip systems. Therefore, cracks tend to form at the interface during cyclic loading. Even though the increase of the GND density near the interface of the soft layer is the main reason for the back stress strengthening in a tension of aluminum laminated composites [29], the area with a high density of GNDs provided a strain gradient and became an ideal crack initiation site under a fatigue loading condition.

The healing mechanism of fatigue damage using electric pulses was suggested to be phase reset-based self-healing [24], dislocation annihilation [25,33], or microcrack closure induced by the compressive thermal stress and local melting around the microcrack tips [34-37]. The thermal compressive stress proved to be the result of the temperature gradient due to the uneven distribution of the electric current density around the crack [36,37]. In the present fatigue test of the ACS sheet, the cyclic load promoted the accumulation of fatigue damage, including the pile-up of GNDs and microcracks at the interface, as presented above. Application of an electric pulse provided the compressive thermal stress to close the formed microcracks and diminished the density of the GNDs at the interface by the combination of the thermal (Joule heating) and athermal effect of electric current.

Regarding the athermal effect of electric current, the mechanism of the athermal effect was suggested that a charge imbalance strongly weakens the bonding strength at the defect region, including dislocations, grain boundary, and interface, which was validated by the first principle calculation and measurement of the elastic modulus under electric pulse [20]. When the electric current passed through the specimen, the interface with a thin IMC (about 1 μm) acted as a line defect and enlarged the charge imbalance near the interface. The charge imbalance resulted in weakened atomic bonding strength. The movement of atoms was then enhanced (in addition to the thermal effect of Joule heating) and the redistribution and eradication of the dislocations in the interface region occurred. In other words, the electric pulse with a subsecond duration (0.5 sec) diminished the density of the GNDs at the interface. The initiation of the microcracks resulting from the accumulated dislocations was then suppressed or even eliminated (i.e., healed). As a result, the formation and propagation of macrocracks were retarded, and the fatigue life was prolonged. In summary, the prolonged

fatigue life can be explained by a combination of diminished dislocation density at the interface and the retardation of microcrack formation or even crack-healing.

3.5 CONCLUSION

High potential lightweight ACS sheet fabricated by cold roll bonding and following heat treatment was used to investigate the tensile and fatigue behavior of the laminated metal composites in the present study. The progressive fatigue damage evolution and the healing mechanism of the fatigue-induced damage by electric current were elucidated in detail using EBSD. The following conclusions can be drawn:

1. The dramatically increased mechanical properties in the monotonic tension test were attributed to back stress strengthening due to the incompatible deformation of each constituting layer.

2. Even though the pile-up of the GNDs across the interface generated the back stress strengthening effect, the area with a high density of GNDs provided a strain gradient and became an ideal crack initiation site under a fatigue loading condition. Thus, the crack preferred to form at the interface under cyclic loading and propagate toward the Al1050 side prior to failure due to the pile-up of GNDs in the soft Al grains near the interface.

3. The significantly prolonged fatigue life is the result of a combination of diminished dislocation density and retardation of microcrack formation.

4. Electropulsing treatment with a subsecond duration is an effective method to prolong the fatigue life of the ACS sheet at low stress fatigue, but it is not invariably effective at high stress fatigue.

REFERENCES

[1] F. Yin, J. Ma, B. Liu, J. He, F. Zhang, M. Liu, Y. Dong, Adv. Mater. Process. 2017, pp. 655-665.

[2] M. Talebian, M. Alizadeh, Mater. Sci. Eng.: A 590 (2014) 186-193.

[3] S. Zhang, K. Gao, S.-T. Hong, H. Ahn, Y. Choi, S. Lee, H.N. Han, J. Mater. Res. Technol. 12 (2021) 271-282.

[4] E.-W. Jeong, K.N. Hui, D.-H. Bae, D.-S. Bae, Y.-R. Cho, Met. Mater. Int. 20 (2014) 499-502.

[5] Y. Yang, F. Zhang, J. He, Y. Qin, B. Liu, M. Yang, F. Yin, Vacuum 151 (2018) 189-196.

[6] C. Wang, Y. Jiang, J. Xie, D. Zhou, X. Zhang, Mater. Sci. Eng.: A 708 (2017) 50-59.

[7] J. Wang, A. Misra, Curr. Opin. Solid State Mater. Sci. 15 (2011) 20-28.

[8] A. Lamik, H. Leitner, W. Eichlseder, F.J.S. Riemelmoser, Strain 44 (2008) 440-445.

[9] F. Kümmel, B. Diepold, K.F. Sauer, C. Schunk, A. Prakash, H.W. Höppel, M. Göken, Adv. Eng. Mater. 21 (2019) 1800286.

[10] J. Li, S. Wang, Q. Mao, Z. Huang, Y. Li, Mater. Sci. Eng.: A 756 (2019) 213-218.

[11] M. Huang, G.H. Fan, L. Geng, G.J. Cao, Y. Du, H. Wu, T.T. Zhang, H.J. Kang, T.M. Wang, G.H. Du, H.L. Xie, Sci. Rep. 6 (2016) 38461.

[12] M. Huang, C. Xu, G. Fan, E. Maawad, W. Gan, L. Geng, F. Lin, G. Tang, H. Wu, Y. Du, D. Li, K. Miao, T. Zhang, X. Yang, Y. Xia, G. Cao, H. Kang, T. Wang, T. Xiao, H. Xie, Acta Mater. 153 (2018) 235-249.

[13] C. Schayes, J. Bouquerel, J.-B. Vogt, F. Palleschi, S. Zaefferer, Mater. Charact. 115 (2016) 61-70.

[14] E. Breitbarth, S. Zaefferer, F. Archie, M. Besel, D. Raabe, G. Requena Mater. Sci. Eng.: A 718 (2018) 345-349.

[15] S.-S. Rui, Y.-B. Shang, Y.-N. Fan, Q.-N. Han, L.-S. Niu, H.-J. Shi, K. Hashimoto, N. Komai, Mater. Sci. Eng.: A 733 (2018) 329-337.

[16] R.-Z. Wang, L.-Y. Cheng, S.-P. Zhu, P.-C. Zhao, H. Miura, X.-C. Zhang, S.-T. Tu, Int. J. Fatigue 149 (2021) 106227.

[17] T. Nagoshi, S. Kozu, Y. Inoue, B.E. O'Rourke, Y. Harada, Mater. Charact. 154 (2019) 61-66.

[18] J. Bouquerel, M. Delbove, J.-B. Vogt, Mater. Charact. 145 (2018) 556-562.

[19] S.-S. Rui, Y.-B. Shang, Y. Su, W. Qiu, L.-S. Niu, H.-J. Shi, S. Matsumoto, Y. Chuman, Int. J. Fatigue 113 (2018) 264-276.

[20] M.-J. Kim, S. Yoon, S. Park, H.-J. Jeong, J.-W. Park, K. Kim, J. Jo, T. Heo, S.-T. Hong, S.H. Cho, Y.-K. Kwon, I.-S. Choi, M. Kim, H.N. Han, Appl. Mater. Today 21 (2020) 100874.

[21] M.-J. Kim, M.-G. Lee, K. Hariharan, S.-T. Hong, I.-S. Choi, D. Kim, K.H. Oh, H.N. Han, Int. J. Plast. 94 (2017) 148-170.

[22] J.-W. Park, H.-J. Jeong, S.-W. Jin, M.-J. Kim, K. Lee, J.J. Kim, S.-T. Hong, H.N. Han, Mater. Charact. 133 (2017) 70-76.

[23] J. Zhang, L. Zhan, S. Jia, Adv. Mater. Sci. Eng. 2014 (2014) 1-8.

[24] H.-J. Jeong, M.-J. Kim, S.-J. Choi, J.-W. Park, H. Choi, V.T. Luu, S.-T. Hong, H.N. Han, Appl. Mater. Today 20 (2020) 100755.

[25] Y. Tang, A. Hosoi, Y. Morita, Y.J.I.j.o.f. Ju, Int. J. Fatigue 56 (2013) 69-74.

[26] J. Jung, Y. Ju, Y. Morita, Y. Toku, Int. J. Fatigue 103 (2017) 419-425.

[27] C.L. Yang, H.J. Yang, Z.J. Zhang, Z.F. Zhang, Scr. Mater. 147 (2018) 88-92.

[28] J.G. Kim, M.J. Jang, H.K. Park, K.-G. Chin, S. Lee, H.S. Kim, Met. Mater. Int. 25 (2019) 912-917.

[29] T.Q. Mo, Z.J. Chen, H. Chen, C. Hu, W.J. He, Q. Liu, Mater. Sci. Eng.: A 766 (2019) 138354.

[30] M.-J. Kim, K. Lee, K.H. Oh, I.-S. Choi, H.-H. Yu, S.-T. Hong, H.N. Han, Scr. Mater. 75 (2014) 58-61.

[31] M. Yang, Y. Pan, F. Yuan, Y. Zhu, X. Wu, Mater. Res. Lett. 4 (2016) 145-151.

[32] J. Zhao, X. Lu, J. Liu, C. Bao, G. Kang, M. Zaiser, X. Zhang, Mech. Mater. 159 (2021) 103912.

[33] A. Babutskyi, M. Mohin, A. Chrysanthou, Y. Xu, A. Lewis, Mater. Sci. Eng.: A 772 (2020) 138679.

[34] A. Hosoi, T. Nagahama, Y. Ju, Mater. Sci. Eng.: A 533 (2012) 38-42.

[35] W. Xu, C. Yang, H. Yu, X. Jin, B. Guo, D. Shan, Sci. Rep. 8 (2018) 6016.

[36] H. Song, Z.J. Wang, X.D. He, J. Duan, Sci. Rep. 7 (2017) 7097.

[37] X. Ren, Z. Wang, X. Fang, H. Song, J. Duan, Mater. Des. 188 (2020) 108428.

CHAPTER IV

ELECTRICALLY ASSISTED SOLID STATE LAP JOINING OF DISSIMILAR STEEL S45C AND ALUMINUM 6061-T6 ALLOY

4.1 INTRODUCTION

Reducing the weight of automobiles is crucial to improve their energy efficiency and decrease their exhaust emissions. For battery-driven electric cars, reducing weight additionally increases their driving range, which is a major obstacle to their commoditization. To this end, aluminum alloys are being extensively considered as lightweight alternatives for automotive structural applications [1,2]. However, fabricating sound dissimilar joints between steel and aluminum alloys is still challenging due to their significant differences in melting temperature, thermal expansion, and specific heat, which adversely affect joint performance. In particular, formation of excessive Al-Fe intermetallic compound (IMC) at the steel-aluminum faying interface can dramatically decrease joint efficiency. More reliable joining will be fundamental to allow extensive application of aluminum alloys in the automobile industry.

Various processes for joining steel and aluminum alloys have been adopted to extend the application of aluminum alloys. Joining processes in use can be divided into three categories according to the joining mechanism: fusion joining, mechanical joining, and solid state joining. A major drawback of conventional fusion joining of steel and aluminum alloys is the formation of undesirable brittle IMCs and shrinkage voids during solidification of the molten part. The brittle IMCs most commonly formed at the steel-aluminum interface are Fe_2Al_5 and $FeAl_3$. These brittle IMCs severely deteriorate joint strength, as commonly observed in resistance spot welding [3,4]. While various mechanical joining methods are

applicable, these methods can damage the region surrounding the joint and also increase the manufacturing cost and weight of the joined structural components [5].

Solid state joining methods such as friction stir welding (FSW), ultrasonic spot welding, and solid state pressure welding can be suitable alternative methods for dissimilar joining of steel and aluminum alloys due to their relatively low heat input, high efficiency, and minimal damage to adjacent parts. Liu et al. [6] analyzed the effect of varying process parameters in the FSW of dissimilar aluminum alloys and advanced high-strength steel. According to their study, the maximum ultimate tensile strength could be up to 85% of that of the base aluminum alloy, on the condition that the thickness of the IMC layer was less than 1 μm at the aluminum-steel interface on the advancing side. Xu et al. [7] successfully joined steel DC04 and aluminum alloys by means of ultrasonic spot welding and reported on the formation of IMC versus welding time. Peter et al. [8] verified the bonding mechanism of aluminum-steel joints at the atomic level fabricated by cold pressure joining. Huang et al. [9] reported that plastic deformation under elevated forming temperature enhanced atomic interdiffusion at the aluminum-steel interface, which was found to be crucial to the joint strength resulting from joining by means of a thermally assisted plastic deformation process.

Among the various solid state joining processes, pressure joining is one of classical joining processes used in engineering applications due to its high efficiency and reliable bonding results. In pressure joining, the joint strength is significantly affected by parameters such as surface preparation, deformation ratio, forging speed, and forming temperature [10-12]. A widely accepted mechanism of pressure joining is the film theory [13]. Metallurgical bonding cannot be produced when the surface of the specimen is covered by oxide and contaminant layers, which prohibit contact between the virgin metals. In pressure joining, the

specimen is plastically deformed by force, which breaks the oxide layer and extrudes virgin metal through the microscale cracks. The virgin metals contact each other at the interface until a metallurgical bond is established. Also, elevated temperature plays an essential role in pressure joining by enhancing atomic diffusion and decreasing the compressive force. However, in conventional pressure joining, the specimen usually needs to be heated in a furnace, which requires long process time and complex control facilities.

Electrically assisted pressure joining (EAPJ) has been suggested in many recent studies as a means to overcome the drawbacks of conventional pressure joining. As compared to using a conventional furnace, resistance heating is much faster and has the capability of localized heating. Also, diffusion of atoms at the interfaces including grain boundary can be remarkably enhanced depending on the electric current parameters, by means of athermal effect of electric current distinct from resistance heating [14]. Similar or dissimilar joining by means of EAPJ has been reported by various researchers. Xu et al. [15] investigated the feasibility of joining stainless steel (SUS) 316 foils having different thicknesses by means of electrically assisted solid state pressure welding. Their results show that SUS316 sheets could not be joined at room temperature, but could be successfully joined by applying an electric current density of 6.7 A/mm^2. They studied the effects of various current densities upon joint strength and concluded that not only the resistance heating but also the athermal effect of electric current contributed to the success of joining. Also, Li et al. [16] successfully joined titanium alloy sheets in a lap configuration by means of EAPJ. In addition, Li et al. [17] demonstrated that EAPJ could be easily implemented in dissimilar joining by successfully joining dissimilar SUS316L and Inconel 718 alloys in a cylinder shape. Finally, Jo et al. [18]

applied EAPJ to join equiatomic CrMnFeCoNi-based high-entropy alloys in solid state without any compositional segregation in joining zone.

Even with recent studies on EAPJ by various researchers, studies on dissimilar EAPJ are still limited, and EAPJ of steel and aluminum alloy combinations has not been extensively addressed. In the present study, lap joining of dissimilar steel and aluminum alloys in the solid state was conducted by means of EAPJ and the resultant joint properties were evaluated by means of mechanical testing and microstructural analysis.

4.2 EXPERIMENTAL SET-UP

Commercially available steel S45C and aluminum 6061-T6 alloy (Al6061-T6) sheets of thickness 2 mm were cut along the rolling direction into strips of 10 mm width and 100 mm length for lap joining, as shown in Fig. 4.1. The chemical compositions of S45C and Al6061-T6 are listed in Table 4.1. The EAPJ experiment was conducted using a custom-made fixture installed in a universal testing machine (DTU-900MH, Daekyoung, South Korea), as illustrated schematically in Fig. 4.2. Electric current was provided by a programmable generator (VADAL SP-1000U, Hyosung, South Korea), which was integrated into the joining system to provide resistance heat and specified current densities during joining. The top and bottom dies acting as electrodes were made of tool steel for compression during EAPJ. Two different sets of electrodes were used in the joining experiment. Electrodes having a tip of joining length 6 mm (large electrodes) were firstly used to fabricate EAPJ joints. Electrodes having a tip of joining length 3 mm (small electrodes) were used to induce a failure along the joint interface by reducing the joint interfacial area, thus allowing quantitative evaluation of the shear strength of the steel-aluminum interface, as described in Fig. 4.2. Insulators made of

Bakelite were inserted between the electrodes and the grips of the universal testing machine to protect the testing equipment.

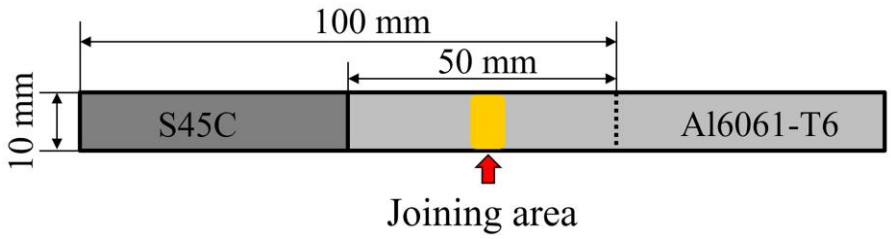

Fig. 4.1. Configuration of the joint.

Table 4.1. The nominal chemical compositions of S45C and Al6061-T6 (in wt%).

elements	C	P	S	Al	Si	Mn	Fe	Mg	Cu	Cr	Zn	Ti
S45C	0.40	0.03	0.04	-	0.20	0.50	Bal.	-	-	0.02	-	-
Al6061-T6	-	-	-	Bal.	0.60	0.11	0.40	0.90	0.23	0.17	0.04	0.03

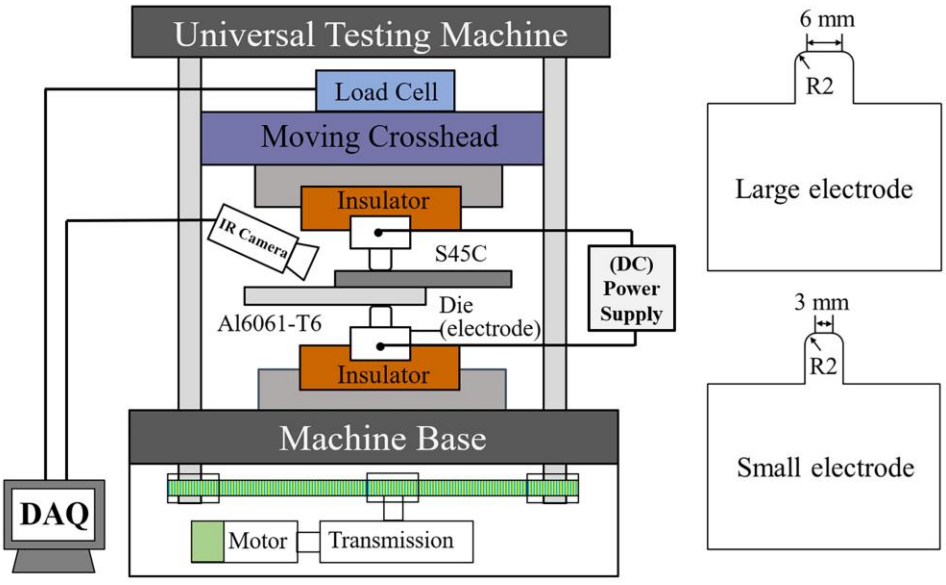

Fig. 4.2. Schematic of the experimental set-up.

In EAPJ, electric current was applied to the specimen assembly held in a lap joining configuration under continuously compressive plastic deformation. Two different sets of electric current patterns were designed, without (Group I) or with (Group II) additional holding time at an elevated temperature after the completion of compressive plastic deformation, as described in Fig. 4.3 and listed in Table 4.2. The Group II pattern was designed to investigate the effect of electric current in enhancing diffusion across the joint interface. Table 4.2 also summarizes other experimental parameters. For simplicity, joints with different electric current patterns were labeled as G-I-N and G-II-N (N represents the nominal electric current density in A/mm2 based on the initial joining area, calculated as the joining length multiplied by the specimen width).

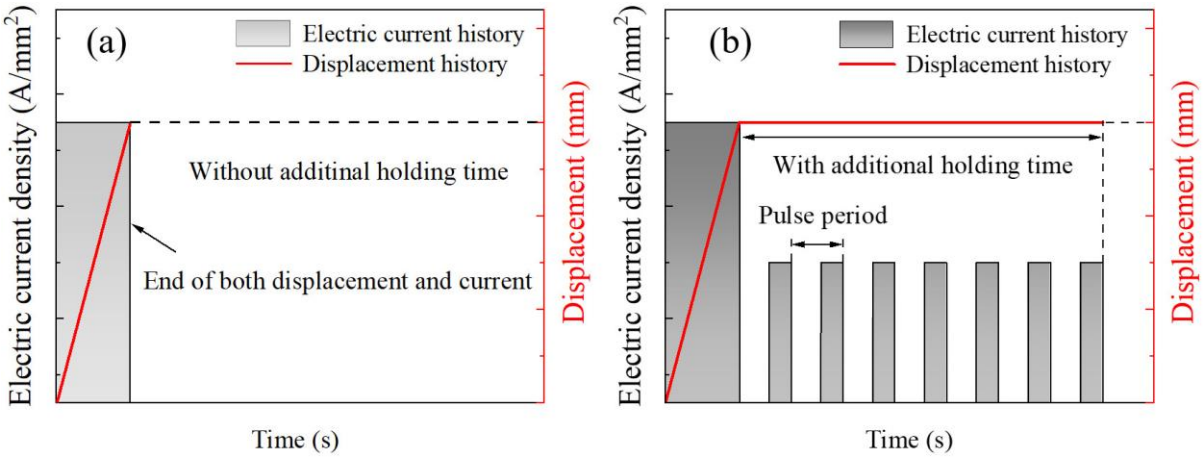

Fig. 4.3. Schematic of electric current and displacement histories during EAPJ. (a) EAPJ without additional holding time, (b) EAPJ with additional holding time.

Table 4.2. Experimental parameter matrix.

Parameter sets	Test label	Nominal current density (A/mm^2)	Current duration (s)	Pulse period (s)	Compressive displacement (mm)	Displacement rate (mm/min)
Group I	G-I-60	60	3	-	1.2	24
	G-I-65	65				
	G-I-75	75				
	G-I-80	80				
Group II	G-II-60	60		7		
	G-II-65	65				
	G-II-75	75				
	G-II-80	80				

Prior to joining, specimens were ground with 320-grit sandpaper to remove the oxide layer and then degreased with acetone to remove oil and other contaminants from the surface. The load history during EAPJ was recorded using a data acquisition system embedded in the testing machine. Also, the temperature history of the specimen was monitored using an infrared thermal imaging camera (FLIR-T621, FLIR, Sweden). To verify the repeatability of the results, at least three sets of specimens were joined for each parameter.

To observe the shape of each joint and to evaluate bonding quality, optical microscopy (OM; A1m Axio Imager, Carl Zeiss, Germany) was carried out on the joint cross-section prepared at the joint center along the length direction. Quasi-static lap shear tensile tests were performed using a universal tensile testing machine, applying the constant cross-head speed of 0.5 mm/min to dissimilar steel-aluminum joints to assess their joint strengths. To properly align each specimen, a spacer was attached to the end of each sheet along the tensile direction, as illustrated in Fig. 4.4. Additionally, Vickers hardness measurements (3 N, 10 s on the steel

side and 2 N, 10 s on the Al side) were carried out on the cross-section at the joint center along the length direction using a Vickers indenter (HM-100, Mitutoyo, Japan).

To better understand the material properties of the joints, the microstructures of the cross-sections at the joint center along the length direction were examined using a field emission scanning electron microscope (FE-SEM; SU70, Hitachi, Japan) equipped with an electron backscatter diffraction system (EBSD; EDAX-TSL Hikari, USA) and an energy dispersive spectrometer (EDS; X-Max50, Horiba, Japan). For the EBSD analysis, the samples were polished with colloidal silica suspension (0.02 μm) at the final. The accelerating voltage and scan step size were 15 kV and 0.45 μm, respectively. The critical misorientation angle was set to 10º for grain identification.

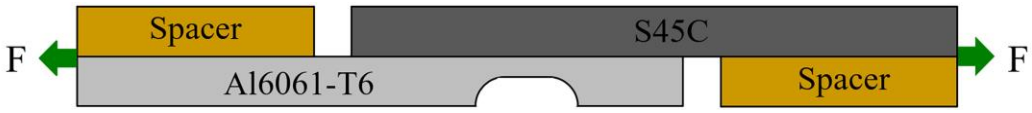

Fig. 4.4. Schematic of lap shear tensile test.

4.3 RESULTS AND DISCUSSIONS

Temperature and load histories were recorded during EAPJ at various nominal electric current densities. For Group I, temperature reached the peak value at the end of the continuous electric current, resulting in a sharp reduction of compressive load (Figs. 4.5(a) and (b)). For Group II, the application of an additional holding time (7 s) under a periodically applied electric current produced serrated (but nearly plateau) temperature and load responses (Figs. 4.5(c) and (d)). The maximum temperature during joining increased from approximately 400 to 580°C (the melting temperature of Al6061-T6 is 660°C) as the nominal electric current

density was increased from 60 to 80 A/mm^2. The maximum compressive load significantly decreased with increasing nominal current density, indicating that the aluminum alloy had been severely softened, as described in Figs. 4.5(b) and (d). After the electric current was stopped, the joint was allowed to cool to room temperature in air. Only the aluminum portion of the specimen was remarkably deformed during joining due to the huge differences in mechanical properties between the aluminum and steel (Fig. 4.6).

Optical microscopy (OM) of a typical joint cross-section along the length direction is provided in Fig. 4.7. This image is quite similar to OM images of joints fabricated by using a small electrode and thus the latter are not included here. All microstructural analysis was carried out on the joints fabricated by using the large electrodes. In the joining area, as shown in Fig. 4.7, only the aluminum sheet was observably deformed after the completion of EAPJ, naturally due to the significantly lower strength of the Al6061-T6 compared to the S45C. In the figure, the magnified image highlighted with red dashed lines shows that the joining interface is continuous, without obvious macroscale cracks or voids. The OM result confirms that Al6061-T6 and S45C were successfully joined. The effective joining length was defined by the initial contact width of the electrode tip since no macroscopic deformation occurred on the steel side, while the pressure and electric current flow focused on the initial contact area during EAPJ. The OM result confirms that it was reasonable to calculate the joining area based on the effective joining length and the specimen width.

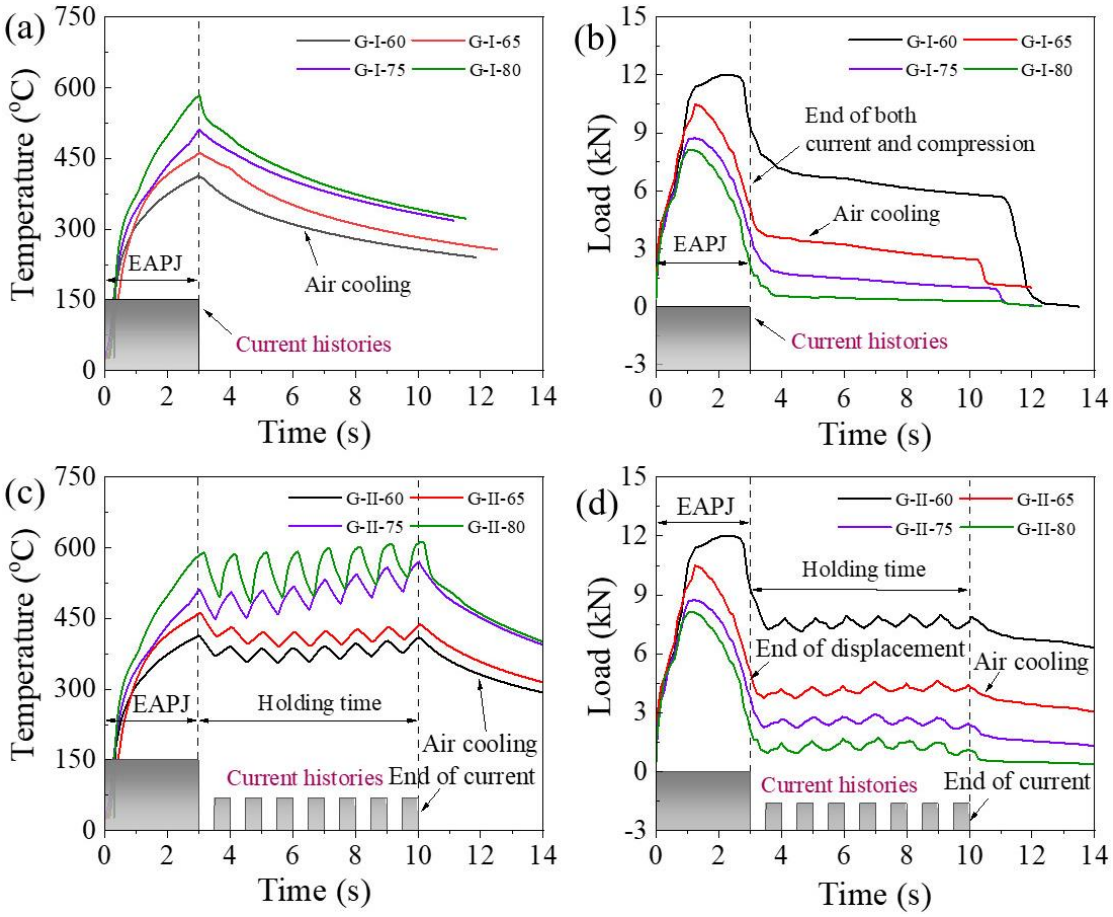

Fig. 4.5. Process responses during EAPJ: (a) temperature histories of G-I group; (b) compressive loads of G-I group; (c) temperature histories of G-II group; (d) compressive loads of G-II group.

Fig. 4.6. EAPJ lap joints of S45C and Al6061-T6.

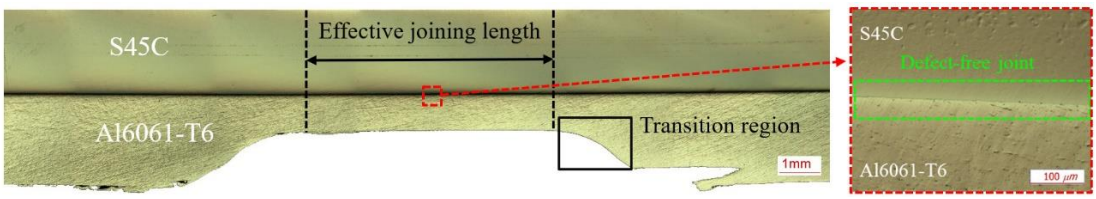

Fig. 4.7. Optical microscopy image of typical cross section.

In the quasi-static lap shear tensile tests to evaluate the joint strength, two different fracture modes (interfacial shear fracture and tensile fracture of the aluminum base metal (Al BM)) were observed, as shown in Fig. 4.8. In the interfacial shear fracture mode, separation along the joint interface occurred (Fig. 4.8(a)). In the tensile fracture mode, fracture occurred at the neck transition region (Fig. 4.8(b)) with some amount of plastic deformation in the Al BM. For the G-I joints, the fracture load increased linearly with increasing electric current density up to 75 A/mm^2. After that, the fracture load slightly decreased with further increase of the electric current density to 80 A/mm^2 (Fig. 4.9, blue line). At the electric current density of 75 A/mm^2, the peak fracture load was obtained (3.36 kN), and the fracture mode changed from interfacial shear fracture to tensile fracture of the Al BM. For the G-II joints, the fracture load similarly increased and then decreased with increasing current density (Fig. 4.9, red line). At the electric current density of 65 A/mm^2, the peak fracture load was obtained (3.61 kN), in the shear fracture mode. Note that for G-II joints, high current densities (75 and 80 A/mm^2) dramatically reduced the fracture load, while the fracture mode changed to tensile fracture of the Al BM.

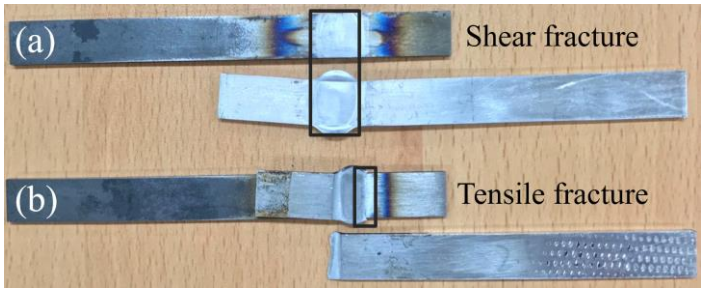

Fig. 4.8. Failure mode of the joints during quasi-static lap shear tensile test: (a) shear fracture, (b) tensile fracture.

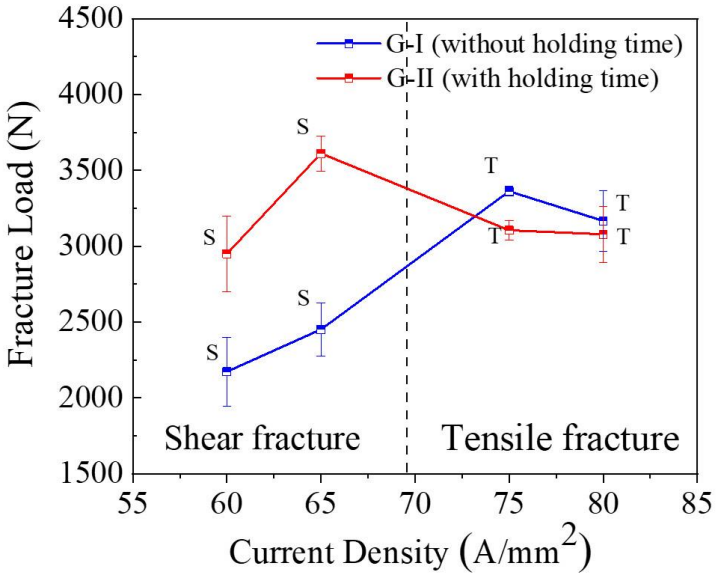

Fig. 4.9. Fracture load of quasi-static lap shear tensile tests.

The trends of fracture load and fracture mode change can be explained by the competition between increasing interfacial joint strength and softening of the BMs, especially of the Al BM, near the joining area under the increasing heat input at higher current densities. For both G-I and G-II joints, at the electric current densities of 60 and 65 A/mm^2, the load required to induce interfacial fracture, i.e., the interfacial joint strength multiplied by the interfacial area, was lower than the load required to induce tensile fracture of the Al BM, even though the results suggest that the interfacial joint strength increased as the current density increased. As a result, interfacial shear fracture occurred for both G-I and G-II joints at the electric current densities of 60 and 65 A/mm^2. The change of fracture mode to tensile fracture of the Al BM at the electric current densities of 75 and 80 A/mm^2 suggests that the load required to induce tensile fracture of the Al BM had decreased below the load required to induce interfacial fracture. This is due to a combined effect of increasing current density, in

mechanically degrading the Al BM while also improving interfacial joint strength. With increasing current density, the interfacial joint strength increased as suggested from the results at the current densities of 60 and 65 A/mm^2. At the same time, the strength of Al BM continuously decreased since more heat was applied to the Al BM as the applied current density increased. Without mechanical degradation of the Al BM owing to resistance heating, the expected tensile fracture load at the neck transition region would be about 3.5 kN. In the tensile fracture region, as indicated in Fig. 4.9, the fracture loads of the joints fabricated by the G-II process were somewhat lower than those of the joints fabricated by the G-I process. This can be easily explained with reference to the fact that excessive heat input during the holding time further softened the Al BM.

It is important to note that a lower fracture load does not suggest a lower joining strength along the interface (interfacial joint strength) of the S45C and the Al6061-T6. To further investigate the effect of the applied current density upon the interfacial joint strength, an electrode with smaller joining tip (Fig. 4.2) was used to evaluate the interfacial joint strength at high electric current densities. The same nominal electric current densities (75 and 80 A/mm^2) and process parameters were applied to join the S45C/Al6061-T6 sheets for the cases of G-I-75, G-I-80, G-II-75 and G-II-80. Joints were successfully fabricated using the small tips, and their mechanical properties were then evaluated by means of lap shear tensile tests. As expected, the joints fractured in shear fracture mode, and this allowed calculation of the interfacial joint strength at the current densities of 75 and 80 A/mm^2 as shown in Fig. 4.10. Finally, the shear fracture load obtained from the quasi-static lap shear tensile test was converted to interfacial joint strength using the joining area based on the joining length and the specimen width, and this data was then linearly fitted as a function of the current density.

Increasing the current density nearly linearly increased the resulting interfacial joint strength (Fig. 4.11). As a result of the added holding time, the interfacial joint strength of each G-II joint was in every case higher than that of the corresponding G-I joint, showing a significantly enhanced joint strength. The highest interfacial joint strength of 105 MPa was obtained in the G-II process by applying the electric current density of 80 A/mm^2.

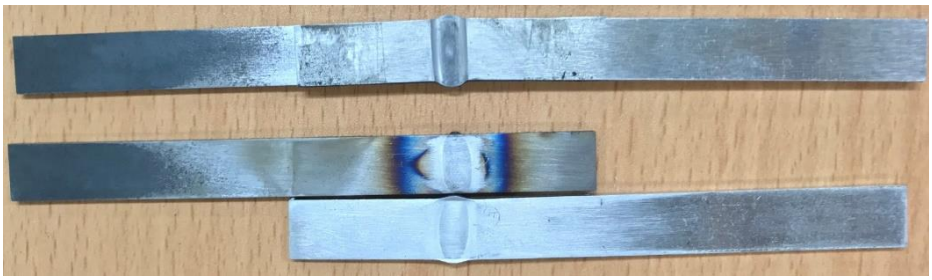

Fig. 4.10. EAPJ joints fabricated by small electrode.

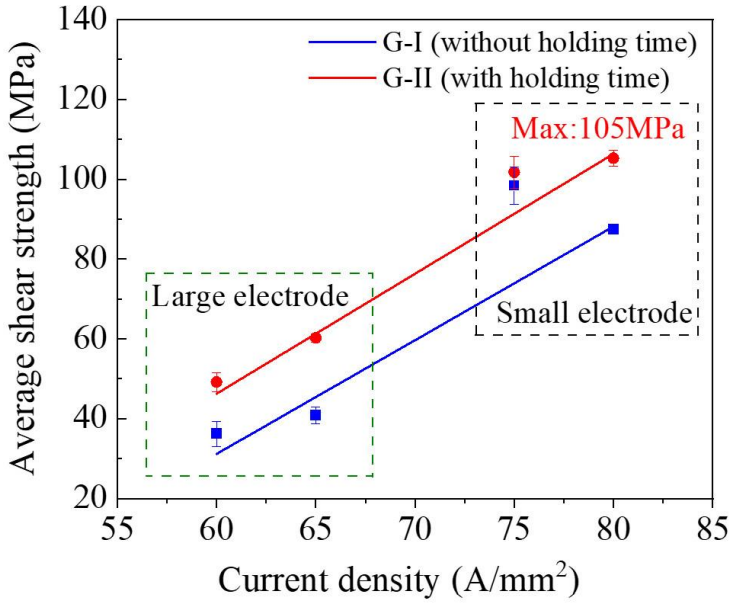

Fig. 4.11. Shear strength as a function of current density.

SEM imaging of the steel-aluminum interface for the G-I-60 joint (the shorter joining time at the lowest joining temperature) and the G-II-80 joint (the longer joining time at the highest joining temperature) confirms that EAPJ produced sound joints without microscale defects (Fig. 4.12). The smooth and continuous interface indicated that a solid state joining process occurred while no observable thick IMC layer was detected at the interface. This result corresponds with the result of Matsuda et al. [19], who reported that only a nanoscale IMC layer was observed by means of TEM in an Al6063/SS304 joint. Moreover, EDS line scans across the steel-aluminum interfaces of the G-I-60 and G-II-80 joints (Fig. 12) suggest that a diffusion zone (marked by a dotted line in the figure) developed along the interface. It is interesting to note that no obvious difference was identified in the thickness of the diffusion zone, even between the G-I-60 and G-II-80 joints. An approximate diffusion thickness of 1.3 μm was observed at the interface, which implied the formation of a relatively thin IMC layer [20-22]. SEM images of the other six different joints were nearly the same and are not presented herein.

EDS elemental mapping, especially the distribution of the Fe and Al, for the G-II-80 joint (Fig. 4.13) suggests that the diffusion was mostly directed into the aluminum. This is reasonable since the atomic radius of Fe is 0.68 times as large as the atomic radius of Al [23]. Note also that the diffusion coefficient of Fe into Al is more than 100 times that of Al into Fe at the joining temperature of 527°C [24]. As a result, the IMC layer was formed mainly on the aluminum side. The distribution of Mg and Mn across the interface in the EDS elemental maps also supports that diffusion occurred during EAPJ. As a result of diffusion, effective joining occurred at the interface under the electric current and plastic deformation.

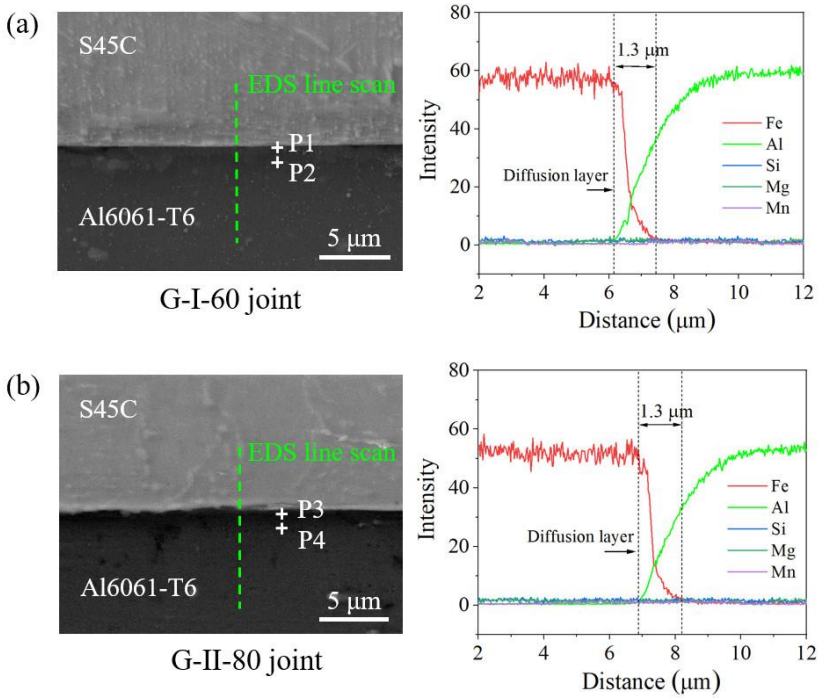

Fig. 4.12. SEM images and EDS line scan of the S45C/Al6061-T6 joints; (a) G-I-60 joint; (b) G-II-80 joint.

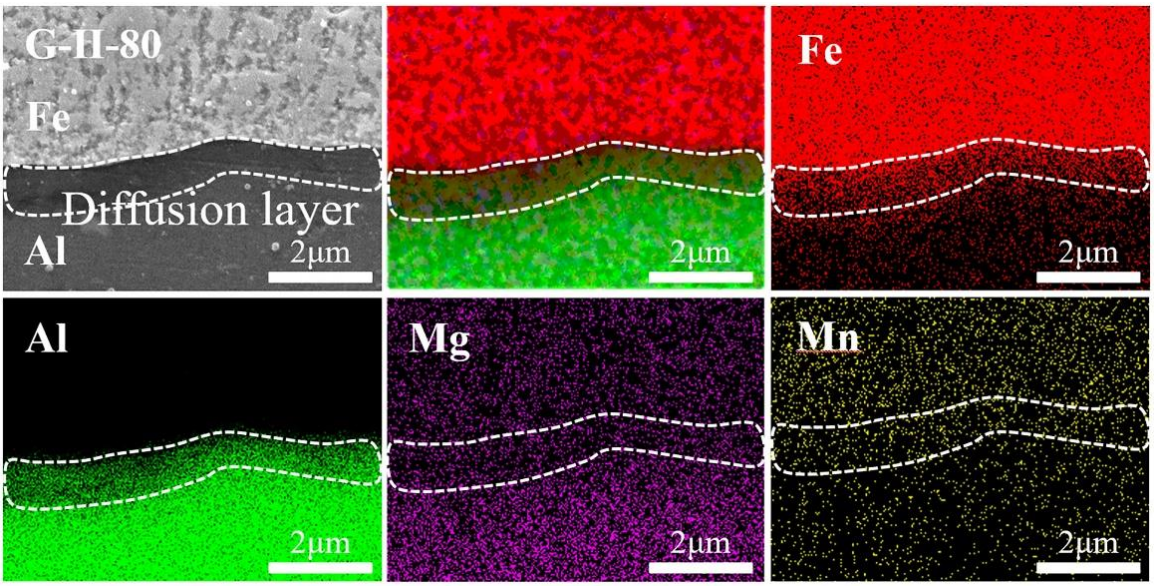

Fig. 4.13. EDS elemental mapping of G-II-80 joint.

Table 4.3. Chemical composition of locations in Fig. 4.12.

Patterns	Location	Composition (at.%)				Possible phase
		Al	Fe	Si	Mg	
G-I-60	P1	45.48	48.21	5.97	0.34	FeAl
	P2	75.36	21.48	2.55	0.61	FeAl3
G-II-80	P3	38.43	59.80	0.81	0.97	FeAl
	P4	68.30	30.02	0.81	0.87	Fe2Al5

As summarized in Table 3, the results of point analysis show that FeAl was formed at the interface of both G-I-60 and G-II-80 joints (P1 and P3 in Fig. 4.12, from the interfacial joining line), whereas $FeAl_3$ and Fe_2Al_5 were formed approximately 0.8 μm away from the joint interface for G-I-60 and G-II-80 joints (P2 and P4 in Fig. 4.12). It is speculated that the hard and brittle $FeAl_3$ deteriorated the interfacial joint strength, resulting in fracture along the IMC under a lower fracture load [25]. Hence, for the material combination selected in the present study, the different interfacial joint strengths observed can be explained by the formation of different IMCs having different relative thicknesses during EAPJ [26,27].

The EBSD inverse pole figure (IPF) maps and kernel average misorientation (KAM) maps were acquired for BMs (Fig. 4.14). In the figures, JD, ND, and TD indicate the joining, normal, and transverse direction, respectively. Grain sizes of Al and steel BMs were 32.2±11.2 μm and 13.6±6.7 μm, respectively, from the IPF maps (Fig. 4.14(a)). The KAM map shows that the Al BM might be fully annealed (Fig. 4.14(b)). IPF maps show that the

microstructure of the Al6061-T6 was significantly altered depending on the joining parameters, while that of the S45C was barely affected (Fig. 4.15). For the Al6061-T6, recrystallization, grain growth, and subsequently deformed microstructure were observed in all G-I joints since it underwent plastic deformation and temperature elevation during the EAPJ process. Increase of grain size was observed in Al6061-T6 with the increase of current density for both G-I and G-II joints, which shows the effect of elevated joining temperature and increased athermal effect [28-31] by higher nominal electric current density. Also, the grain growth of Al6061-T6 was further promoted during the added holding time with periodic application of electric current, as clearly shown by comparing the results of the corresponding G-I and G-II joints (for example, compare the IPF maps for the G-I-65 and G-II-65 joints). Note that for the Al6061-T6, not only average grain sizes of G-I joints were smaller than those of G-II joints, but also small grains were observed near large grains. For the S45C, noticeable microstructure evolution after EAPJ was barely observed in the IPF maps. For all the EAPJ conditions, applied stress and temperature might be insufficient to change the microstructure of the S45C BM.

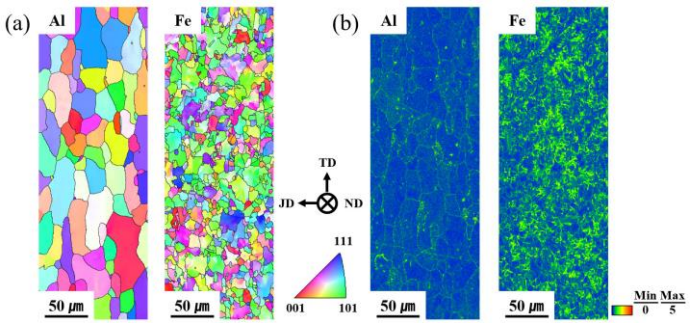

Fig. 4.14. (a) and (b) EBSD inverse polar figure (IPF) ND maps and Kernel average misorientation (KAM) maps of Al and steel BMs. The different colors in IPF maps indicate the orientation of each grain with respect to ND.

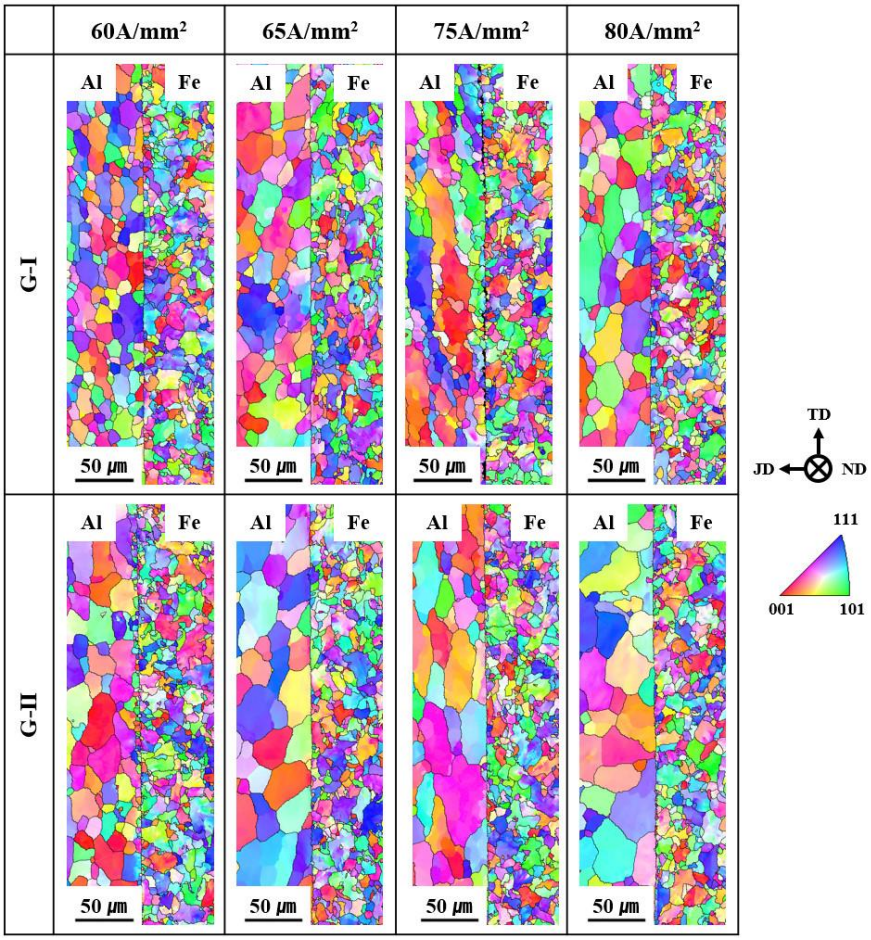

Fig. 4.15. EBSD IPF ND maps for G-I and G-II joints with various nominal electric current densities (60, 65, 75, and 80 A/mm^2).

For both G-I and G-II joints, the Vickers hardness profiles (Fig. 4.16) across the joint interface were similar. The significantly reduced hardness (average values close to 70 HV) on the aluminum side after joining could be understood to result from severe softening under the electric current. As reported by Sato et al. (1999) [32], Al-Mg-Si alloy typically softens when heated above 200°C. At high temperatures, strengthening precipitates (for example, Mg_2Si) dissolve, which markedly degrades the hardness and strength of the Al-Mg-Si alloy. The

transition of hardness observed across the interface, lacking any abrupt peak value, indicates that no thick IMC layer formed at the interface during EAPJ. Also, the hardness on the steel side had no noticeable variation, confirming that the microstructure of S45C barely changed during the EAPJ.

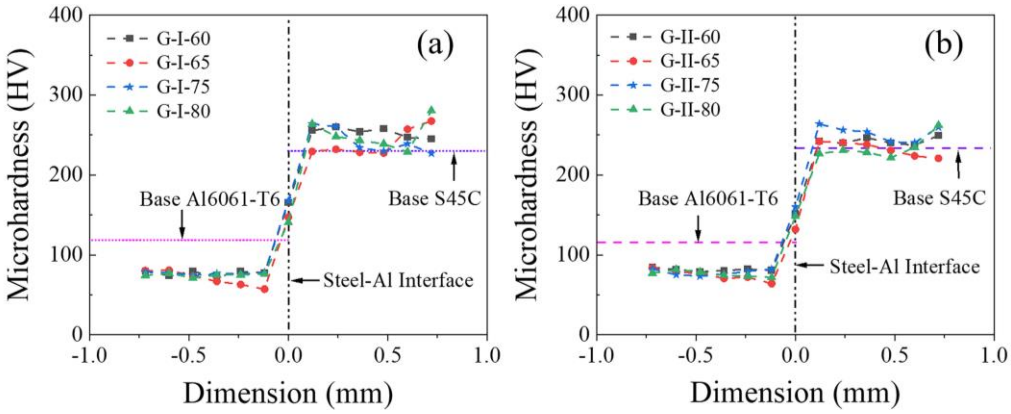

Fig. 4.16. Microhardness profiles of the joints across the interface: (a) G-I group; (b) G-II group.

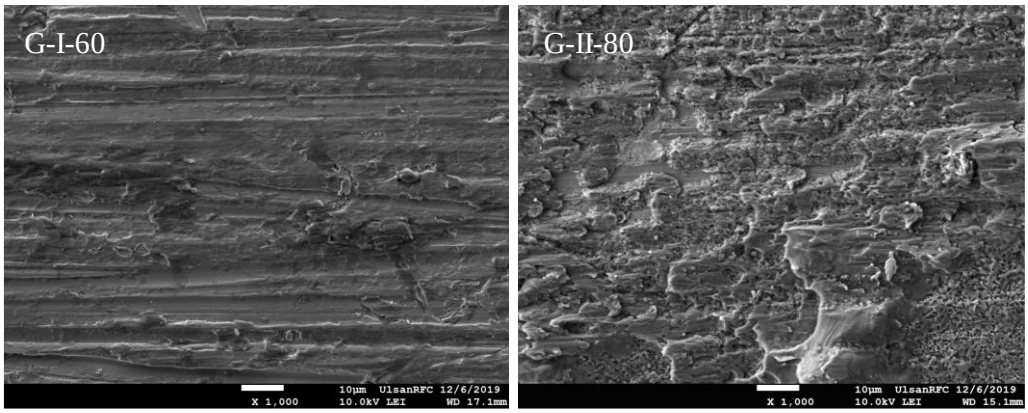

Fig. 4.17. Fracture morphology of G-I-60 and G-II-80 joints.

Fracture surfaces of the G-I-60 (large electrode) and G-II-80 (small electrode) joints exhibited typical characteristics of cleavage fracture along the interface (Fig. 4.17). During tension, cracks initiated and propagated through the steel-aluminum interface, producing

intermetallic fracture. The G-I-60 joint showed highly brittle cleavage fracture, which can be expected based upon its low interfacial joint strength. The G-II-80 joint showed relatively small and fine cleavage facets, which predominantly contributed to its higher interfacial joint strength compared to the other joints studied. Also, some dimpled fracture characteristics in the G-II-80 joint indicated relatively ductile fracture behavior during tension.

4.4 CONCLUSIONS

Solid state lap joining of dissimilar S45C steel and Al6061-T6 was successfully conducted by means of EAPJ. Increasing the current density nearly linearly increased the interfacial joint strength. SEM-EDS analysis suggested that diffusion occurred across the interface and formed a diffusion zone of thickness approximately 1.3 μm on the aluminum side. The results of point analysis suggested that the different interfacial joint strengths were the result of the formation of different IMCs of different thicknesses during EAPJ. EBSD analysis showed that the microstructure of the Al6061-T6 could be significantly altered depending on the EAPJ parameters, whereas the microstructure of S45C was barely affected. In quasi-static lap shear tensile tests with interfacial shear fracture, brittle cleavage fracture behavior was observed due to intermetallic fracture.

The present study clearly confirms the feasibility of EAPJ for the selected dissimilar combination of S45C and Al6061-T6. The results of the present study are expected to contribute to the development of cost-effective and energy-efficient solid state joining processes for steel and aluminum alloys.

REFERENCES

[1] K. Martinsen, S.J. Hu, B.E. Carlson, Joining of dissimilar materials, CIRP Annals, 64 (2015) 679-699.

[2] T. Sakiyama, Y. Naito, M. Yasunobu, T. Nose, G. Murayama, K. Saita, H. Oikawa, Dissimilar metal joining technologies for steel sheet and aluminum alloy sheet in auto body, Nippon Steel Technical Report, (2013) 91-98.

[3] N. Chen, M. Wang, H.-P. Wang, Z. Wan, B.E. Carlson, Microstructural and mechanical evolution of Al/steel interface with Fe2Al5 growth in resistance spot welding of aluminum to steel, Journal of Manufacturing Processes, 34 (2018) 424-434.

[4] N. Chen, H.-P. Wang, M. Wang, B.E. Carlson, D.R. Sigler, Schedule and electrode design for resistance spot weld bonding Al to steels, Journal of Materials Processing Technology, 265 (2019) 158-172.

[5] K.-i. Mori, N. Bay, L. Fratini, F. Micari, A.E. Tekkaya, Joining by plastic deformation, CIRP Annals, 62 (2013) 673-694.

[6] X. Liu, S. Lan, J. Ni, Analysis of process parameters effects on friction stir welding of dissimilar aluminum alloy to advanced high strength steel, Materials & Design, 59 (2014) 50-62.

[7] L. Xu, L. Wang, Y.-C. Chen, J.D. Robson, P.B. Prangnell, Effect of Interfacial Reaction on the Mechanical Performance of Steel to Aluminum Dissimilar Ultrasonic Spot Welds, Metallurgical and Materials Transactions A, 47 (2015) 334-346.

[8] N.J. Peter, C. Gerlitzky, A. Altin, S. Wohletz, W. Krieger, T.H. Tran, C.H. Liebscher, C. Scheu, G. Dehm, P. Groche, A. Erbe, Atomic level bonding mechanism in steel/aluminum joints produced by cold pressure welding, Materialia, 7 (2019).

[9] Z. Huang, J. Yanagimoto, Dissimilar joining of aluminum alloy and stainless steel thin sheets by thermally assisted plastic deformation, Journal of Materials Processing Technology, 225 (2015) 393-404.

[10] P. Groche, S. Wohletz, A. Erbe, A. Altin, Effect of the primary heat treatment on the bond formation in cold welding of aluminum and steel by cold forging, Journal of Materials Processing Technology, 214 (2014) 2040-2048.

[11] O. Napierala, C. Dahnke, A.E. Tekkaya, Simultaneous deep drawing and cold forging of multi-material components: Draw-forging, CIRP Annals, 68 (2019) 269-272.

[12] S. Wohletz, P. Groche, Temperature Influence on Bond Formation in Multi-material Joining by Forging, Procedia Engineering, 81 (2014) 2000-2005.

[13] H.A. Mohamed, J. Washburn, Mechanism of solid state pressure welding, Weld J (Miami), (1975) vp.

[14] M.-J. Kim, S. Yoon, S. Park, H.-J. Jeong, J.-W. Park, K. Kim, J. Jo, T. Heo, S.-T. Hong, S.H. Cho, Y.-K. Kwon, I.-S. Choi, M. Kim, H.N. Han, Elucidating the origin of electroplasticity in metallic materials, Applied Materials Today 21 (2020).

[15] Z. Xu, L. Peng, X. Lai, Electrically assisted solid-state pressure welding process of SS 316 sheet metals, Journal of Materials Processing Technology, 214 (2014) 2212-2219.

[16] Y.-F. Li, H. Das, S.-T. Hong, J.-W. Park, H.N. Han, Electrically assisted pressure joining of titanium alloys, Journal of Manufacturing Processes, 35 (2018) 681-686.

[17] Y.-F. Li, S.-T. Hong, H. Choi, H.N. Han, Solid-state dissimilar joining of stainless steel 316L and Inconel 718 alloys by electrically assisted pressure joining, Materials Characterization, 154 (2019) 161-168.

[18] M.-G. Jo, T.A.N. Nguyen, S. Park, J.-Y. Suh, S.-T. Hong, H.N. Han, Electrically Assisted Solid-State Joining of CrMnFeCoNi High-Entropy Alloy, Metallurgical and Materials Transactions A 51(12) (2020) 6142-6148.

[19] T. Matsuda, H. Adachi, T. Sano, R. Yoshida, H. Hori, S. Ono, A. Hirose, High-frequency linear friction welding of aluminum alloys to stainless steel, Journal of Materials Processing Technology, 269 (2019) 45-51.

[20] M. Kimura, K. Suzuki, M. Kusaka, K. Kaizu, Effect of friction welding condition on joining phenomena and mechanical properties of friction welded joint between 6063 aluminium alloy and AISI 304 stainless steel, Journal of Manufacturing Processes, 26 (2017) 178-187.

[21] E. Taban, J.E. Gould, J.C. Lippold, Dissimilar friction welding of 6061-T6 aluminum and AISI 1018 steel: Properties and microstructural characterization, Materials & Design (1980-2015), 31 (2010) 2305-2311.

[22] K.P. Mehta, A review on friction-based joining of dissimilar aluminum–steel joints, Journal of Materials Research, 34 (2018) 78-96.

[23] P. Li, S. Chen, H. Dong, H. Ji, Y. Li, X. Guo, G. Yang, X. Zhang, X. Han, Interfacial microstructure and mechanical properties of dissimilar aluminum/steel joint fabricated via refilled friction stir spot welding, Journal of Manufacturing Processes, 49 (2020) 385-396.

[24] A. Gerlich, G. Avramovic-Cingara, T.H. North, Stir zone microstructure and strain rate during Al 7075-T6 friction stir spot welding, Metallurgical and Materials Transactions A, 37 (2006) 2773-2786.

[25] W. Jiang, H. Jiang, G. Li, F. Guan, J. Zhu, Z. Fan, Microstructure, Mechanical Properties and Fracture Behavior of Magnesium/Steel Bimetal Using Compound Casting Assisted with Hot-Dip Aluminizing, Metals and Materials International, (2020).

[26] H. Dong, Y. Li, P. Li, X. Hao, Y. Xia, G. Yang, Inhomogeneous microstructure and mechanical properties of rotary friction welded joints between 5052 aluminum alloy and 304 stainless steel, Journal of Materials Processing Technology, 272 (2019) 17-27.

[27] U. Shah, X. Liu, Effects of ultrasonic vibration on resistance spot welding of transformation induced plasticity steel 780 to aluminum alloy AA6061, Materials & Design, 182 (2019).

[28] M.-J. Kim, K. Lee, K.H. Oh, I.-S. Choi, H.-H. Yu, S.-T. Hong, H.N. Han, Electric current-induced annealing during uniaxial tension of aluminum alloy, Scripta Materialia 75 (2014) 58-61.

[29] H.-J. Jeong, J.-W. Park, K.J. Jeong, N.M. Hwang, S.-T. Hong, H.N. Han, Effect of Pulsed Electric Current on TRIP-Aided Steel, International Journal of Precision Engineering and Manufacturing-Green Technology 6(2) (2019) 315-327.

[30] J.-W. Park, H.-J. Jeong, S.-W. Jin, M.-J. Kim, K. Lee, J.J. Kim, S.-T. Hong, H.N. Han, Effect of electric current on recrystallization kinetics in interstitial free steel and AZ31 magnesium alloy. Materials Characterization 133 (2017) 70-76.

[31] H.-J. Jeong, M.-J. Kim, S.-J. Choi, J.-W. Park, H. Choi, V.-T. Luu, S.-T. Hong, H.N. Han, Microstructure reset-based self-healing method using sub-second electric pulsing for metallic materials. Applied Materials Today 20 (2020) 100755.

[32] Y.S. Sato, H. Kokawa, M. Enomoto, S. Jogan, Microstructural evolution of 6063 aluminum during friction-stir welding, Metallurgical and Materials Transactions A, 30 (1999) 2429-2437.

CHAPTER V

EFFECTIVENESS OF AN ADDITIVELY MANUFACTURED POROUS LAYER IN DISSIMILAR SOLID-STATE BULK JOINING OF ADDITIVELY MANUFACTURED MARAGING STEEL AND CONVENTIONAL AISI410 STEEL

5.1 INTRODUCTION

The growing demand for manufacturing hybrid components in the automobile and aerospace industries has motivated the development of advanced joining technology. Among various joining techniques, solid-state pressure joining can be an effective alternative to conventional fusion joining since it can avoid welding shrinkage and cracking, which are commonly observed in fusion-based welding techniques [1,2]. In solid-state pressure joining, plastic deformation with associated heating breaks the oxide layer and extrudes the virgin materials through the cracks to the contact, thus creating a solid-state joining. Electrically assisted pressure joining (EAPJ) is a novel solid-state pressure joining process that provides local and fast resistance heating, as well as enhanced atomic diffusion via the athermal effect of electric current (i.e., the electroplastic effect) [3-7]. The athermal effect of electric current has been reported to enhance the kinetics of metal atoms, thus accelerating or inducing annealing [3,4], microstructure healing [5], recrystallization [6], and aging [7], in addition to the well-known thermal effect of resistance heating. In EAPJ, interfacial bonding is established through atomic diffusion and recrystallization induced through the combination of elevated temperature (resistance heating), athermal effect of electric current, and plastic deformation [8-10]. Therefore, this solid-state joining technique is well suited for joining similar or dissimilar alloys.

Selective laser melting (SLM) is an additive manufacturing (AM) technique that is developed for rapid prototyping and manufacturing based on the powder-bed fusion (PBF) technique. During SLM-AM, the powder is deposited layer-by-layer and selectively melted using a laser source, followed by solidification under rapid cooling. As a result, this method can be used to fabricate functional products (such as hollow components, parts with an internal truss structure, and dies with cooling channel) that have complex shapes or geometries, which would be otherwise impossible using conventional methods. In addition, a type of AM technique known as directed energy deposition (DED) can be used to repair locally damaged components to return the value of the product and restore the part to its original shape and workable condition [11-16]. Nevertheless, additive manufacturing is suffering from surface roughness, anisotropy, residual stress as well as a relatively long time to fabricate a large component, which hinders its wide application. Maraging steel 1.2709 (commonly known as tool steel), which is primarily composed of Ni, Co, Mo, Ti, Al, and balanced Fe, is a promising high strength AM metal with very low carbon content. The microstructure of additively manufactured (AMed) maraging steel is characterized by soft nickel martensite and retained austenite due to the low carbon content and high element content of Ni [17]. The AM of maraging steels can be used to manufacture engine casings, forming tools, injection molding dies, and products with cooling channels after precipitation hardening treatment or solution annealing process owing to their high specific strength and good fracture toughness [18]. Commercialized AISI410 is a 12% chromium martensitic stainless steel with low carbon content that can be hardened by heat treatment to a lath martensite structure at a low cooling rate (air cooling). AISI410 is widely used to fabricate automobile components and medical instruments because of its high strength, corrosion

resistance, and high resistance to wear [19,20]. Bulk joining of AMed (typically by SLM) maraging steel and conventionally manufactured AISI410 can promote the application of hybrid material combinations in many industrial sectors, such as the gas turbine industry and the customization of plastic injection molding dies.

Several researchers have successfully achieved joining of dissimilar metal combinations using direct AM or a combination of AM and conventional joining methods and have characterized the microstructural evolution and mechanical behavior of the joints. Samei et al. [21] successfully printed Corrax steel on the AISI420 substrate using a laser powder bed fusion technique to validate the potential hybrid manufacturing of plastic injection molding dies. After printing, a hybrid heat treatment was used to improve the mechanical properties and metallurgical compatibility. Void nucleation and growth due to interfacial mechanical incompatibility and decohesion were observed. Bai et al. [22] deposited the maraging steel on the top of the cast CrMn steel using the SLM method. They characterized the microstructure of interfacial morphology of the hybrid component to study the metallurgical property and observed a 130 μm wide interface between the two dissimilar materials. Tabaie et al. [23] reported a hybrid joining method combining linear friction welding and SLM for joining SLM Inconel 718 and forged Ni-based superalloy AD730. Recently, Hong et al. [24] successfully demonstrated that the process efficiency can be improved through the use of a separately AMed porous interlayer in bulk solid-state joining (EAPJ) of cylindrical SUS316L specimens. Moreover, the EAPJ method is successfully applied to join the dissimilar materials combination of S45C and aluminum 6061 [2], SUS316L and Inconel 718 [25], and a similar materials combination of equiatomic CrMnFeCoNi-based high-entropy alloys [26].

In the present study, a hybrid joining method integrating AM and EAPJ was used to join a dissimilar material combination of SLM-AMed maraging steel 1.2709 and conventionally manufactured AISI410 stainless steel. In the SLM-AM of maraging steel specimens, a porous layer was also simultaneously fabricated on the joining surface of the specimens to overcome the deformation asymmetry by adjusting the deformation resistance, which enhances the virgin metals extrusion attributed to the sufficient surface enlargement in pressure joining. In the meantime, the porous layer was also considered to improve the process efficiency and resultant joint properties. The resultant joint properties were evaluated in detail by microstructural analysis and mechanical testing.

5.2 EXPERIMENTAL SET-UP

5.2.1 Material preparation and AM process

Cylindrical maraging steels 1.2709 specimens with a diameter of 16 mm and a height of 58 mm were AMed (simply, AM-MS1). The cylindrical AISI410 stainless steel specimens were prepared by conventional machining with identical dimensions to AM-MS1. The chemical compositions of the AM-MS1 and AISI410 are listed in Table 5.1.

Table 5.1. Chemical compositions of the materials (wt%)

Elements	C	Mn	Si	S	P	Cr	Ni	Al	Mo	Co	Ti	Fe
AM-MS1	0.03	0.1	0.1	0.01	0.01	-	18.0-19.0	0.05-0.15	4.7-5.2	8.5-9.5	0.5-0.8	Bal.
AISI410	0.11	0.5	0.5	0.01	0.03	12.3	0.75	-	0.07	0.03	-	Bal.

The AM process was conducted using a custom-made SLM machine (SLM 280HL, SLM solutions GmbH, Germany) equipped with twin 400 W fiber lasers and soft coating lips. Commercially available spherical-shaped MS1 powder (SLM Solutions Group AG, Germany) with a particle size range from 10–45 μm was used in the SLM-AM. The platform was maintained at 100 °C during AM to reduce residual stress. The build chamber was filled with argon gas (the oxygen content < 0.1%) to prevent oxidation during the AM process. The other printing parameters used during specimen fabrication are summarized in Table 5.2. After printing, the porosity was calculated using ImageJ software after grinding and polishing.

Table 5.2. SLM AM process parameters

AM-MS1	Laser power (W)	Hatch distance (μm)	Scanning speed (mm/s)	Layer thickness (μm)
High density: >99.5% (non-porous matrix)	250	100	850	50
Low density: 79% (porosity 21%)	160	100	850	50

Through AM of the MS1 specimens, two different types of samples (with or without a porous layer at the joining end) were prepared, as schematically shown in Fig. 5.1. For the MS1 specimens without a porous layer (simply, NPL-MS1 specimens), a height of 58 mm was AMed with high density (> 99.5%), which is nearly equivalent to the perfectly solid matrix. For the MS1 specimens with a porous layer (simply, PL-MS1 specimens), a height of 5 mm with low density, approximately 79% (porosity of 21%), was AMed first at the bottom of the cylindrical specimen, while the top side with a height of 53 mm was AMed continuously with high density (> 99.5%). The porous layer reduces the joining compressive

load and localizes the temperature elevation by increasing the local electrical resistance through intentionally induced geometrical defects (i.e., relatively high porosity). Also, since the high porosity in the porous layer reduces the mechanical strength of the joining end of the relatively hard MS1 specimen, more relatively symmetric deformation of the EAPJed specimens can be achieved.

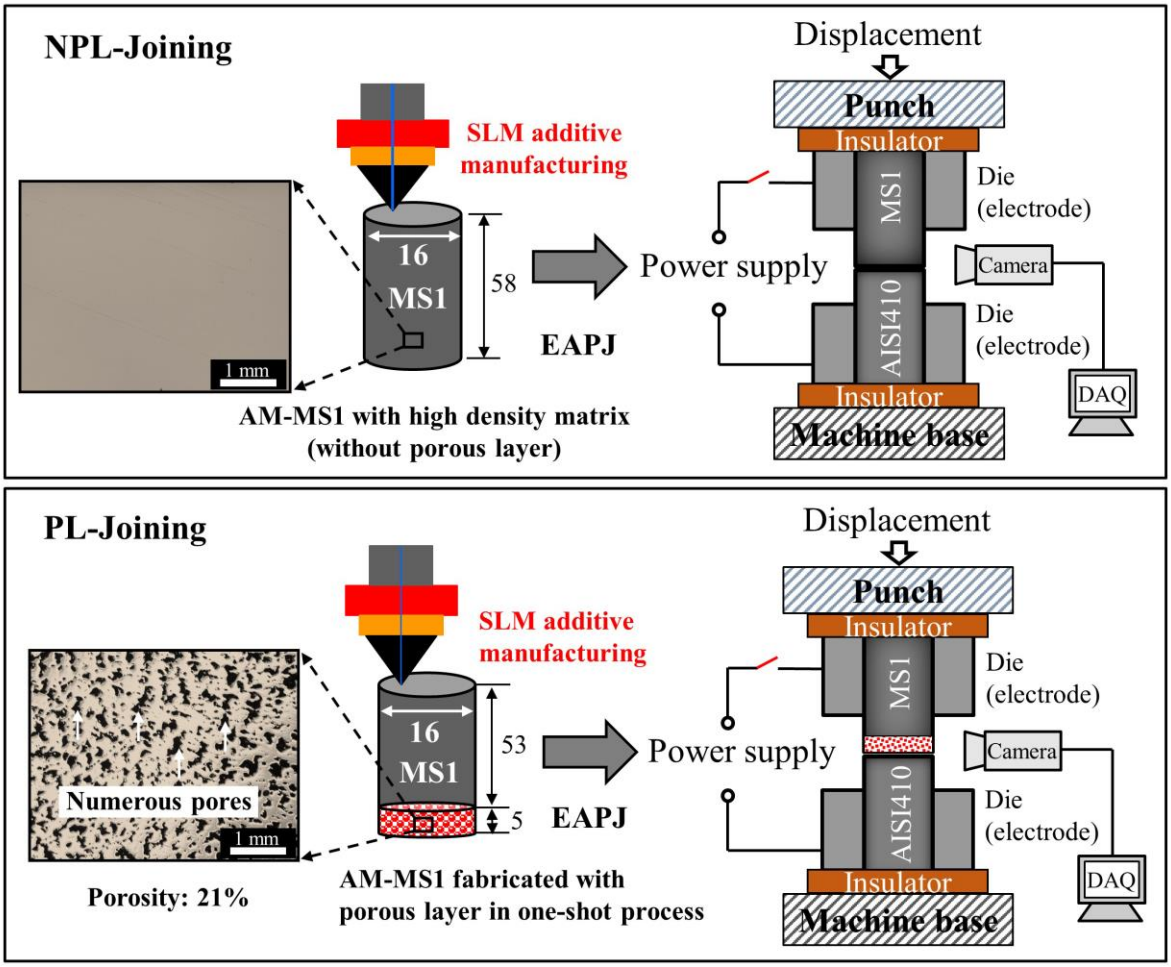

Fig. 5.1. Schematics of EAPJ: without porous layer (top) and with porous layer (bottom)

5.2.2 EAPJ process

EAPJ experiments were conducted on a universal servo press machine along the axial direction of specimen assembly with a custom-made fixture (Fig. 5.1) in the ambient air at room temperature. To ensure the stability of specimen assembly during joining, the AM-MS1 and AISI410 specimens were inserted into the top and bottom electrodes (40 mm deep for each side), respectively. According to the setup, each specimen can be divided into the unaffected region (inserted into the electrode during joining) and the heat-affected region (heated and deformed region between the joint interface and electrode). Two insulators made of Bakelite were inserted between the crosshead of the servo press machine and the electrode to protect the equipment. During EAPJ, an electric current generated by a controllable generator (SP-1000U, Hyosung, South Korea) and a maximum displacement of 15 mm with a constant displacement rate of 20.5 mm/min were simultaneously applied. The joining surface of the specimen was ground using sandpaper and cleaned with acetone before joining. The temperature variation was monitored by an infrared thermal imaging camera (FLIR-T621, FLIR, Sweden). The samples were painted with black thermal paint to stabilize the emissivity and improve the accuracy of the measured temperature. The maximum temperature during joining was used to present the temperature histories when the electric current was applied to the specimen assembly. The histories of the compressive displacement and load were also recorded by the DAQ system equipped in the universal servo press machine. The same parameters (Table 5.3), which were selected by separately conducted preliminary experiments, were adopted for the two different combinations (NPL-joining for NPL-MS1 and AISI410 and PL-joining for PL-MS1 and AISI410, Fig. 5.1). As illustrated in Fig. 5.2, the electric current pattern was designed as a combination of initial continuous electric current followed by pulsed

electric current. The continuous electric current was used for rapid heating initially during EAPJ, while a pulsed electric current was adopted to induce a holding time to maintain the elevated temperature during deformation, which also reduced the deformation resistance and enhanced interfacial diffusion. Five specimen assemblies were joined for each combination to verify repeatability.

Table 3. EAPJ process parameters

Displacement rate (mm/min)	Compressive displacement (mm)	Continuous current density* (A/mm^2)	Duration of continuous current (sec)	Pulsed current density* (A/mm^2)	Holding time (sec)	Total joining time (sec)
20.5	15	31.6	5	15.4	36	41

* : Current density was calculated based on the original cross-sectional area of the specimen without deformation.

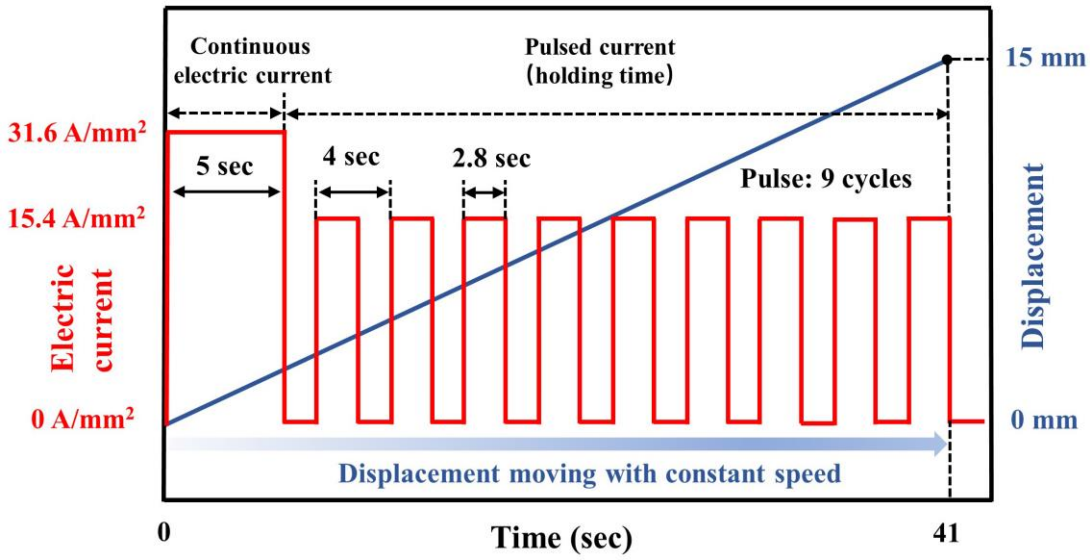

Fig. 5.2. The electric current and displacement during EAPJ

5.2.3 Microstructural analysis

After joining, the joints were cross-sectioned perpendicular to the joining interface along the joining direction (the yellow rectangular region in Fig. 5.5). The samples were initially ground to 1200 grit and polished with 1 and 0.25 μm diamond paste following standard metallographic preparation and then slightly etched (Cupric chloride 12 gm; Hydrochloric acid 20 ml; Alcohol 225 ml) for general observation. The joint interface was first observed by laser confocal microscopy (VK-X200, Keyence, Osaka, Japan) to assess the joint quality. The microstructure was characterized at the joint interface after a final polish with 0.5 μm colloidal silica suspension using a field emission scanning electron microscope (FE-SEM: SU5000, Hitachi, Japan) equipped with an electron backscatter diffractometer (EBSD: TSL Hikari Super, TSL, USA). Elemental diffusion was evaluated by an energy dispersive spectrometer (EDS: X-Max50, Horiba, Japan) at 25000× magnification. For the EBSD analysis, the accelerating voltage, probe current, and tilt angle was set to 20 eV, 14 nA, and 70°, respectively. The step sizes of 0.12 μm for the base metal and 32 nm for the joint interface and a working distance of 15–18 mm were used during the analysis. A grain tolerance angle of 5° was used for grain identification. The grain size, inverse pole figure (IPF) maps, image quality (IQ) maps with grain boundaries, kernel average misorientation (KAM) maps, and grain average image quality (GAIQ) maps were used to analyze the microstructure evolution during EAPJ. In IQ maps, the misorientation angle of 2°–15° was defined as the low-angle grain boundary (LAGB), while the high-angle grain boundary (HAGB) was defined as angles greater than 15°.

5.2.4 Mechanical testing

The mechanical properties of the joints were evaluated by quasi-static tensile tests and microhardness testing. The microhardness (HV) was measured (1 N, 10 sec) across the joint interface (200 μm from the joint interface to the BM for each side) using a Vickers indenter (HM-200, Mitutoyo, Japan). The joints were machined to a "dog-bone" shape (ASTM E8/E8M) with a gauge length of 30 mm and a diameter of 8 mm for quasi-static tensile tests. The tensile tests were performed on a universal tensile machine with a constant displacement rate of 1 mm/min. After testing, the fracture surfaces were also examined to evaluate the fracture mechanism during tension.

5.3 RESULTS AND DISCUSSION

5.3.1 Process response during EAPJ and joint appearance

For both NPL and PL joining, the temperature histories showed a rapid rise under the initial continuous electric current and a near plateau under the following pulsed electric current (Fig. 5.3(a)), even though a slight decrease of temperature near the completion of joining process was observed for both cases. The temperature during NPL joining was consistently lower than that of PL joining through the entire joining process. The average temperature during the holding time was 900 and 1010 °C for the NPL and PL joining, respectively. Notably, the experimental parameters used in EAPJ were the same for these two joints. The differences in temperature histories are due to the significantly increased electrical resistance at the porous layer with geometrically induced defects (a porosity of 21%).

The instantaneous temperature distribution (Figs. 5.3(c) and (d)) along the axial direction of the heat-affected region suggests that the temperature increase was highly

localized on the porous layer (approximately, the region in pink in Fig. 5.3(d)) during PL joining. In contrast, the NPL joining shows a relatively even temperature distribution. Furthermore, the peak force for PL joining was significantly reduced by 44% compared with that for NPL joining, as indicated in Fig. 5.3(b). The significantly reduced peak force was attributed to a combined effect of both higher temperature and lower strength of the porous layer.

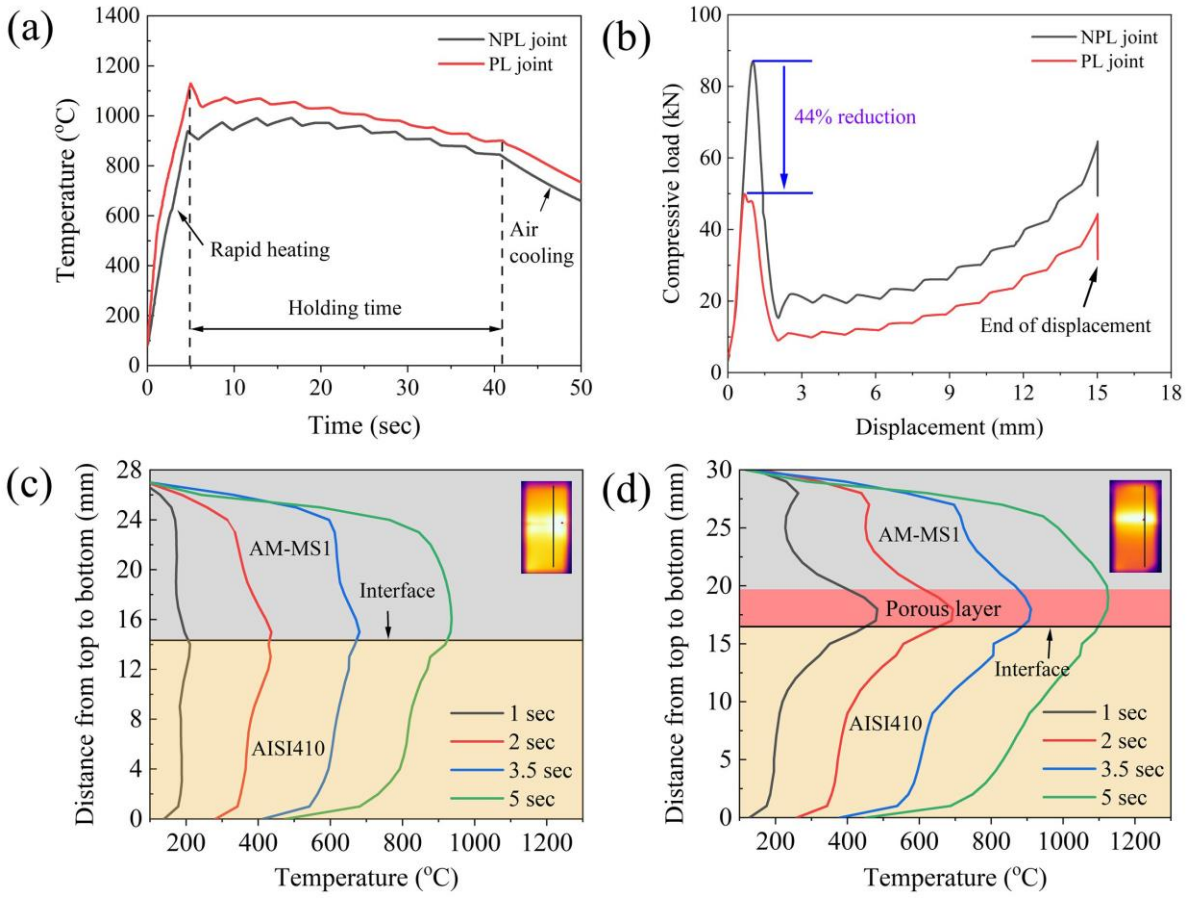

Fig. 5.3. Process response during EAPJ: (a) temperature histories and (b) compressive load histories; temperature distribution along the axial direction for (c) the NPL joint and (d) the PL joint

A different deformation morphology for the NPL and PL joints was observed after EAPJ, as exhibited in Fig. 5.4. The asymmetric deformation with respect to the NPL joint interface (Fig. 5.4(a)) indicates a huge difference in mechanical properties of AM-MS1 and AISI410 at the joining temperature during EAPJ, which resulted in major deformation on the AISI410 side. As a result of asymmetric deformation, AISI410 was overlaid on AM-MS1 while AM-MS1 was gradually deformed in the whole heat-affected region. For the PL joint (Fig. 5.4(b)), the porous layer was majorly squeezed out during deformation and formed a relatively symmetric shape with respect to the interface. Note that the cross-section of the porous layer was significantly enlarged during EAPJ, while the region above the porous layer to the electrode was not significantly deformed. Therefore, deformation was concentrated in the porous layer and the base matrix (AM-MS1 with high density) was effectively protected. The deformed shape of the joint manifests that using a porous layer in solid-state joining can reduce the deformation asymmetry by adjusting the deformation resistance, which can be a crucial factor (sufficient surface enlargement for virgin metals extrusion) in pressure joining.

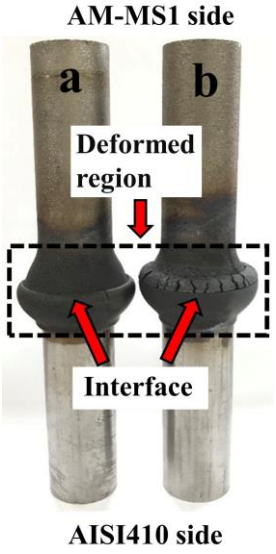

Fig. 5.4. The appearance of the joints: (a) NPL joint and (b) PL joint

5.3.2 Optical and scanning electron microscopy

The optical microscope images of the cross-sections observed from the interface of both NPL and PL joints show that macroscopically defect-free joints were fabricated by EAPJ (Figs. 5.5(a) and (b)). For the PL joint, the pores of the AMed porous layer were completely eliminated during EAPJ. The metallurgical bonding formed through diffusion was evidenced by the EDS mapping, as presented in Figs. 5.5(c) and (d). The major elements (Fe, Ni, Cr, Co, and Mo) distributed homogenously across the interface without obvious chemical segregation suggest that a sound bonding was established under rapid heating and severe plastic deformation during EAPJ.

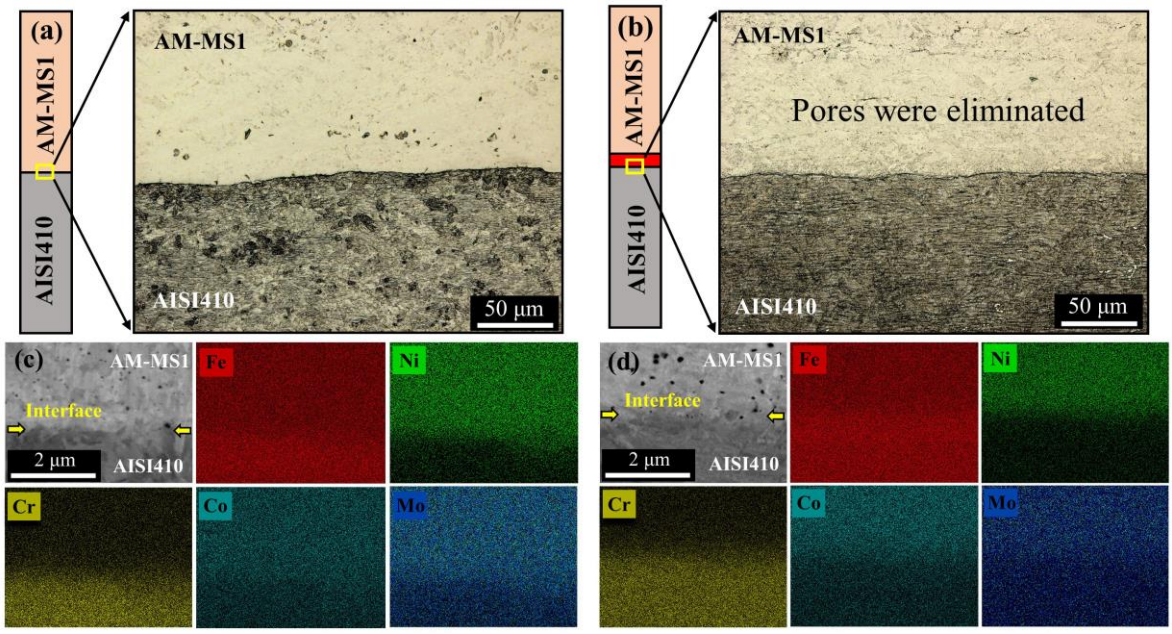

Fig. 5.5. Optical micrographs of the AM-MS1/AISI410 interface for (a) the NPL joint and (b) the PL joint; SEM images of the interface and its relevant EDS mapping of the major elements for (c) the NPL joint and (d) the PL joint

The quantitative evaluation of the diffusion thickness across the joint interface in Fig. 6 shows that the diffusion thickness of the NPL and PL joints was 1.3 μm and 1.9 μm, respectively. An approximately 46% increase in diffusion thickness was achieved in the PL joint with the porous layer. Note that the increased diffusion thickness in solid-state joining corresponds to a higher interfacial joint strength [27-29]. The results of the point analysis on the spherical black dots (points A and B in Fig. 5.6) presented chemical compositions (Table 5.4) similar to that of the MS1 powder, which suggests the formation of the nanosized particles. During the fabrication of AM-MS1 with millimeter-sized pores by SLM-AM, unmelted MS1 powder can be trapped inside the pores. In EAPJ with large plastic deformation and heat input, the trapped MS1 powder formed micro-welded particles, while the original millimeter-sized pores were closed and eliminated.

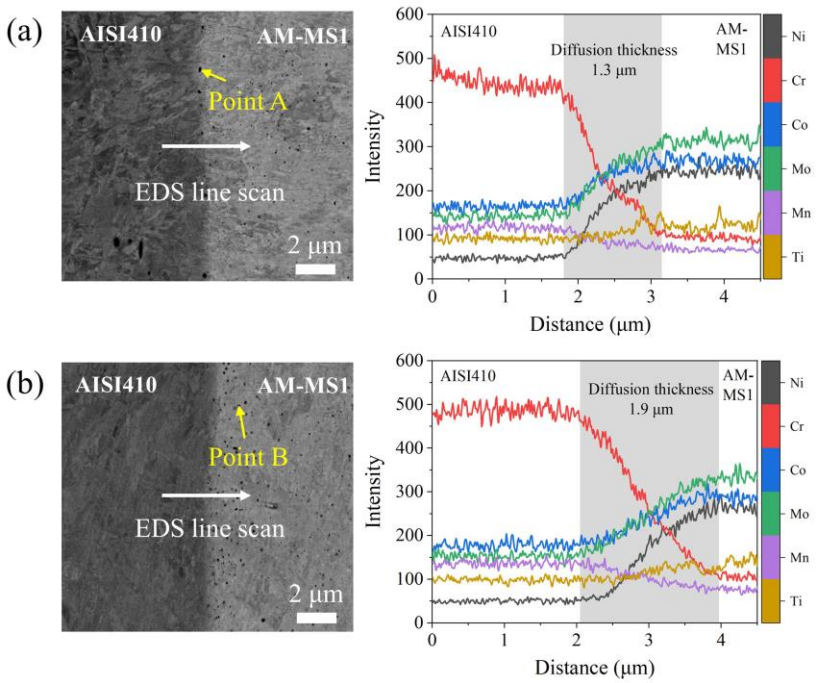

Fig. 5.6. EDS line scan analysis with a length of 4.5 μm for major elements traces: (a) NPL joint and (b) PL joint

Table 5.4. Chemical compositions of points A and B (wt%)

Elements	Cr	Ni	Mo	Co	Ti	Fe
Point A	0.60	18.40	5.30	9.02	0.64	66.03
Point B	1.15	16.6	5.38	7.53	4.91	64.44

5.3.3 EBSD analysis

Equiaxed and homogeneously orientated grains with an average grain size of 7.9 ± 4.0 μm for AISI410 BM were obtained, while the AM-MS1 had more heterogeneous grains with a preferred orientation and average grain size of 4.4 ± 6.0 μm in the as-built condition, as shown in the EBSD IPF maps in Figs. 5.7(a) and (b). After joining, the grains were significantly refined from 7.9 ± 4.0 μm to 2.6 ± 2.4 μm for AISI410 and from 4.4 ± 6.0 μm to 1.5 ± 1.2 μm for AM-MS1 in the NPL joint as a result of the dynamic recrystallization (Fig. 5.7(c)). The resultant average grain size of AM-MS1 for the PL joint (2.4 ± 1.9 μm) was slightly larger than that for the NPL joint (1.5 ± 1.2 μm) since it experienced higher temperature during joining (Fig. 5.7(d)). The large difference in grain size distribution indicates that partial dynamic recrystallization occurred on both sides of NPL and PL joints [30]. Additionally, slightly more compressed grains on the AM-MS1 side of the PL joint correspond to the fact that the deformation of the AM-MS1 specimen was more concentrated in the porous layer for the PL joint, as shown in the joint morphology (Fig. 5.4).

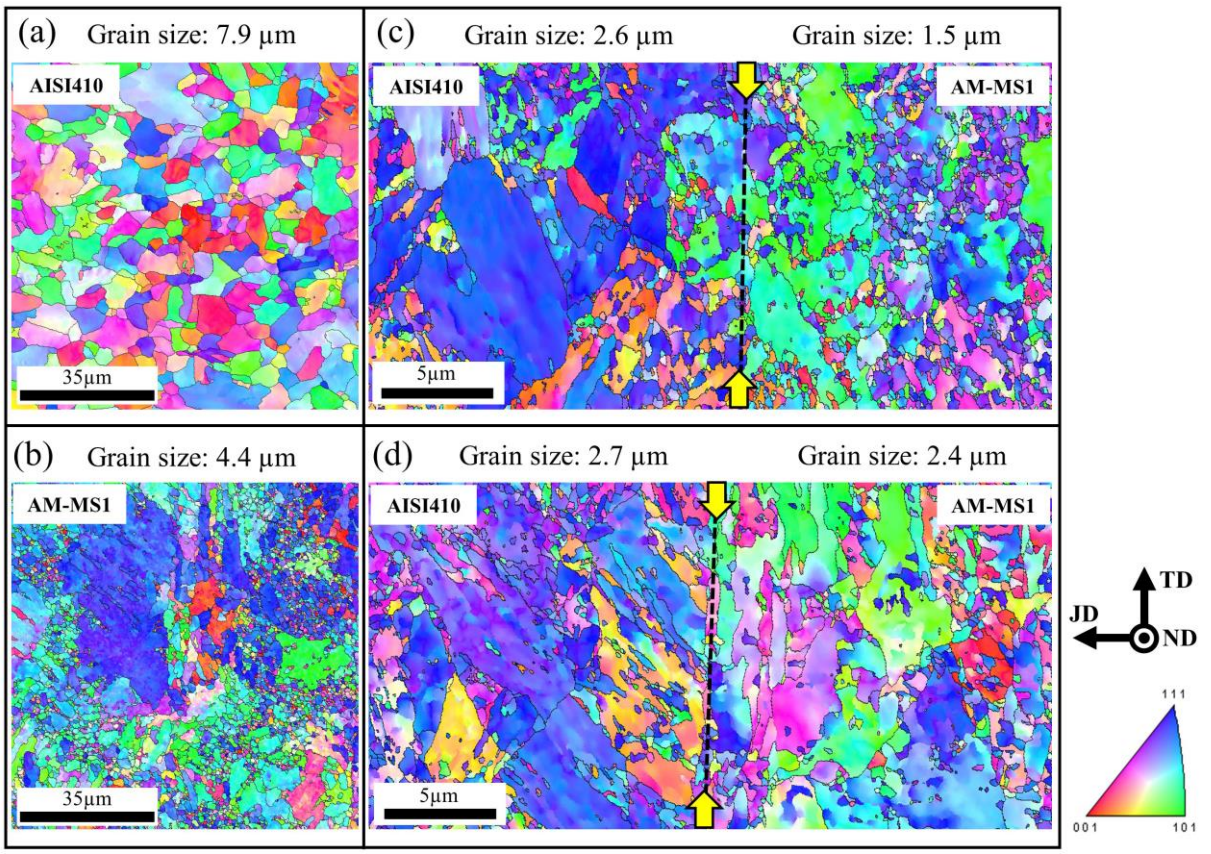

Fig. 5.7. EBSD IPF maps and the grain size: (a) the AISI410 BM, (b) the AM-MS1 BM, (c) each side for the NPL joint, and (d) each side for the PL joint (JD-joining direction; TD-transverse direction; ND-normal direction)

To better understand the microstructure evolution during EAPJ, the grain boundary and KAM maps were obtained, as presented in Fig. 8. In the grain boundary maps (Figs. 5.8(a)-(c)), the fractions of the HAGBs and LAGBs are given as a percentage of the total grain boundaries for BMs and each side of the joints. The fractions of HAGBs were dominantly high in both AISI410 and AM-MS1 BMs, which is essential for the strengthening mechanism [31]. After joining, both joints exhibited a higher ratio (NPL AISI410: 1.0; NPL AM-MS1:

1.2; PL AISI410: 0.9; PL AM-MS1: 0.8) of LAGBs to HAGBs than the BMs (AISI410 BM: 0.3; AM-MS1 BM: 0.17), which is the result of plastic deformation experienced during EAPJ. Furthermore, the fraction of HAGBs for both the AISI410 and AM-MS1 sides of the PL joint is slightly higher than that of the NPL joint as a result of the relatively high plastic deformation in the PL joint. The very high average KAM value for the AM-MSI BM (2.68) indicates that high residual stress was induced during the AM by steep thermal gradient from the instant melting and rapid solidification with a high cooling rate [17], as presented in

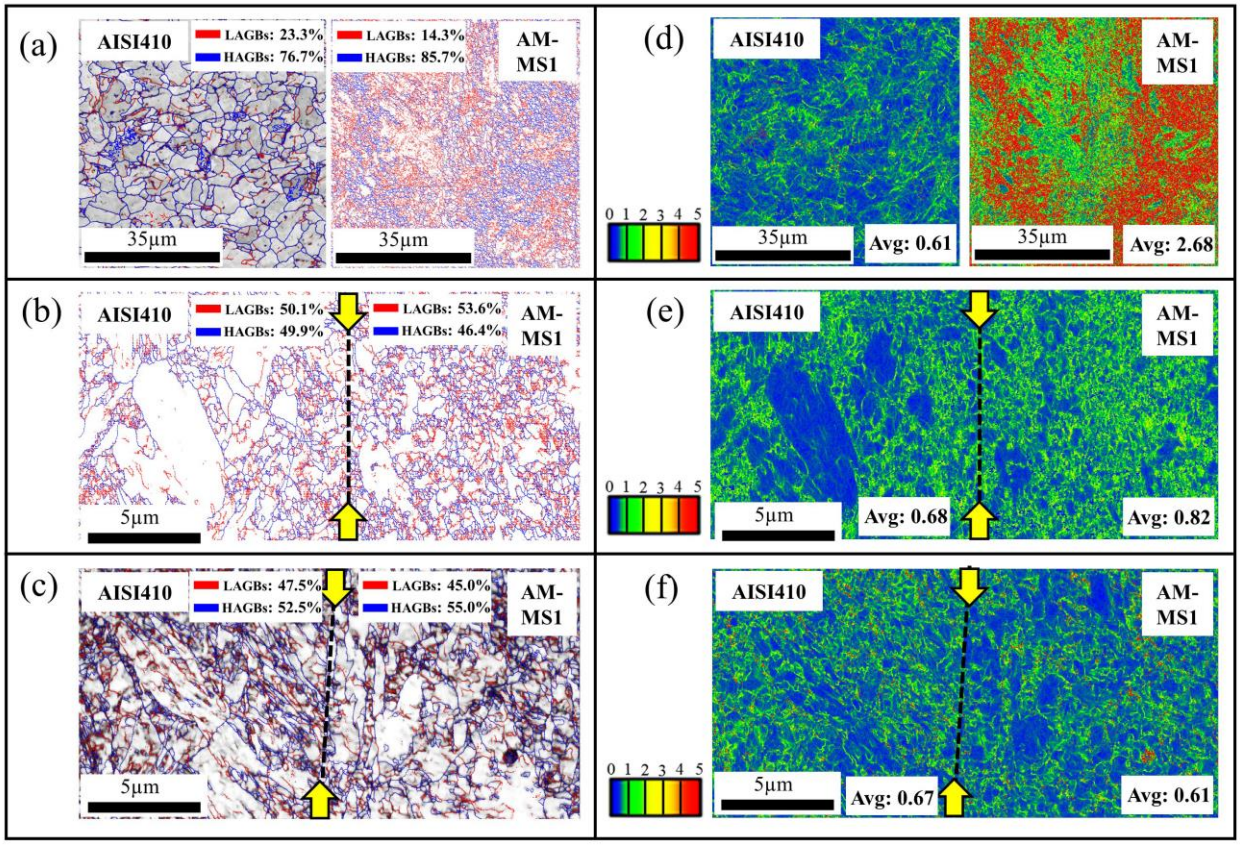

Fig. 5.8. IQ maps overlaid with grain boundaries: (a) the BMs, (b) the NPL joint, and (c) the PL joint; KAM maps: (d) the BMs, (e) the NPL joint, and (f) the PL joint (the fractions of HAGBs and LAGBs are given in IQ maps; the average KAM values are given in KAM maps)

Fig. 5.8(d). The significantly reduced KAM value (Figs. 8(e) and (f)) in the AM-MS1 side for both NPL and PL joints compared with the BM suggests that the residual stress from the AM process was greatly relieved. The further reduced KAM value in the AM-MS1 side (from 0.82 to 0.61) for the PL joint can be understood as a result of the further increased temperature via the porous layer. On the contrary, the AISI410 shows only a slight variation in the KAM value [BM: 0.61; NPL joint: 0.68; PL joint: 0.67] after joining.

To quantitatively evaluate the phase change during EAPJ for both AISI410 and AM-MS1, the IQ parameter can be used to differentiate the phases based on the lattice imperfection [32-34]. The crystal lattice of martensite has more defects and a lower IQ value, while the relatively perfect crystal lattice of ferrite and austenite has a higher IQ value. In the present study, the IQ value of 5000 was used to differentiate the martensite from ferrite and austenite [34]. In the case of BMs (Figs. 5.9(a) and (c)), AISI410 was dominated by the phases with an IQ value greater than 5000 (annealed ferrite structure [35]), while the AM-MS1 was majorly comprised of martensite with an

IQ value lower than 5000. A significant increase in martensite fraction was detected in the AISI410 side for both the NPL and PL joints, which is evidenced by the fraction of IQ values less than 5000 (Figs. 5.9(b) and (d)). This martensite formation in air cooling for both joints can be compared with the report of Tsai et al. [36], where they showed that dislocated lath martensite can form at a very low cooling rate by air cooling using a series of continuous heating and cooling processes for AISI410. In the as-built condition of AM-MS1 (Fig. 5.9(c)), a small number of phases with an IQ value greater than 5000 was attributed to the retained austenite, which is consistent with reports on AM maraging steel [37]. For the AM-MS1 side, the austenite fraction slightly increased in the NPL joint, while a dramatic increase of

austenite content occurred in the PL joint, as indicated in both the GAIQ map and its relevant area distribution of IQ value in Fig. 5.9(d).

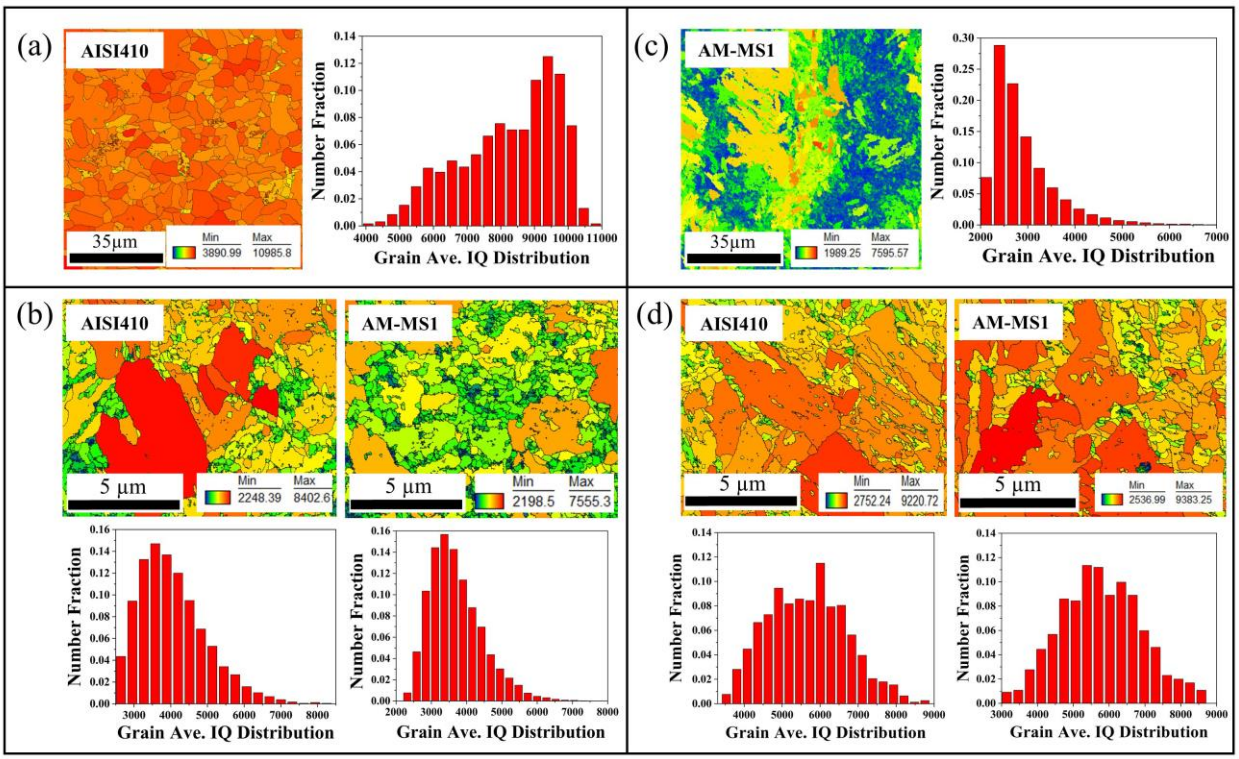

Fig. 5.9. GAIQ maps and relevant distributions of area fraction: (a) the AISI410 BM, (b) the NPL joint, (c) the AM-MS1 BM, and (d) the PL joint

The significantly increased fraction of austenite suggests that the reverted austenite formed during EAPJ [38]. For the PL joint, a higher temperature was achieved more rapidly and was maintained for a longer time, which significantly increased the austenite transformation. Note that the areas with higher solute levels due to the heterogeneous distribution of the elements during AM provided an ideal nucleation site for austenite transformation [38].

3.4 Mechanical properties

The microhardness measurements of the cross-sections of the joints across the joint interface with intervals of 50 μm are presented in Fig. 5.10. The average microhardness of the as-built AM-MS1 was approximately 340 HV. After EAPJ, the microhardness in the AM-MS1 side for both joints decreased, owing to the release of residual stress. The decrease of microhardness agrees with the significantly reduced KAM value, as shown in Fig. 5.8. A significant increase in the microhardness in the AISI410 side for both joints (from BM: 210 HV to joints with about 500 HV) was a result of the high formation amount of martensite during EAPJ, which is supported by the GAIQ values in Fig. 5.9. Note that the microhardness of the AM-MS1 side in the PL joint is somewhat lower than that of the AM-MS1 side in the NPL joint, while the inversed result is observed for the AISI410 side. The reduction of the microhardness for the AM-MS1 side in the PL joint resulted from the higher fraction of the

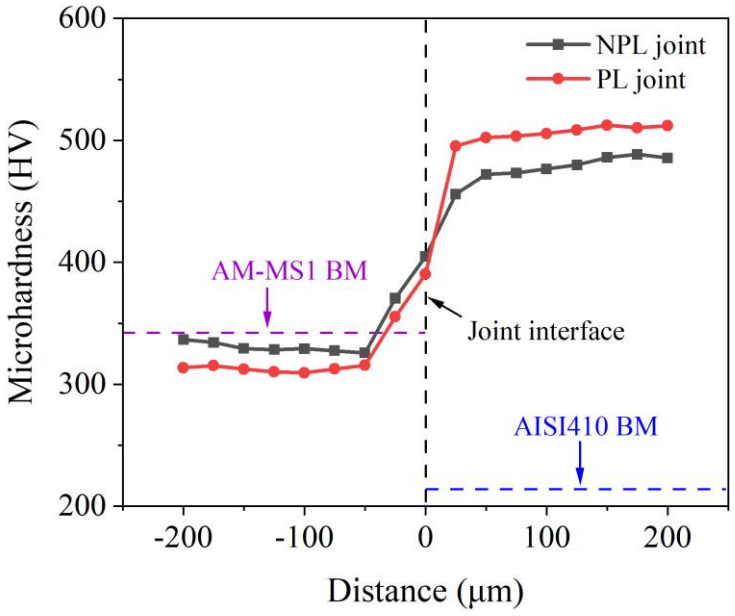

Fig. 5.10. Microhardness profiles across the interface (measurement distance of 400 μm)

retained austenite developed in this side compared to that in the AM-MS1 side of the NPL joint (Figs. 5.9(b) and (d)). The improvement of the microhardness for the AISI410 side in the PL joint compared with the NPL joint can be explained by the dislocation stabilization related to the formation of stable lath martensite structure due to the combined effects of higher temperature and deformation-induced work hardening [39,40].

The engineering stress-strain curves (Fig. 5.11) for both the NPL joint and PL joint exhibited similar ultimate tensile strengths and elongation during the quasi-static tensile test. Both joints fractured at the AISI410 side, as shown in Fig. 5.11. The similar mechanical performances of NPL and PL joints confirm the effectiveness of using porous interlayer during EAPJ of a dissimilar material combination. For both NPL and PL joints, the tensile fracture occurred in the transition region between the heat-affected region and the unaffected region. Note that the unaffected region was inserted into the electrode during joining and its mechanical property is expected to be nearly identical to that of BM. As presented above, the AISI410 side showed a significant increase in martensite content, which significantly strengthens the heat-affected region after joining. However, the unaffected region still has a mechanical strength similar to that of BM, resulting in the fracture at the transition region. The fracture surfaces of the central regions (Fig. 5.12) for the NPL and PL joints exhibited a completely ductile fracture indicated by numerous dimples, which are commonly formed through nucleation, growth, and coalescence of micro-voids. On the contrary, combined fracture characteristics of brittle and ductile fracture at the margin areas for the NPL and PL joints were characterized by the occurrence of both cleavage facets and dimples.

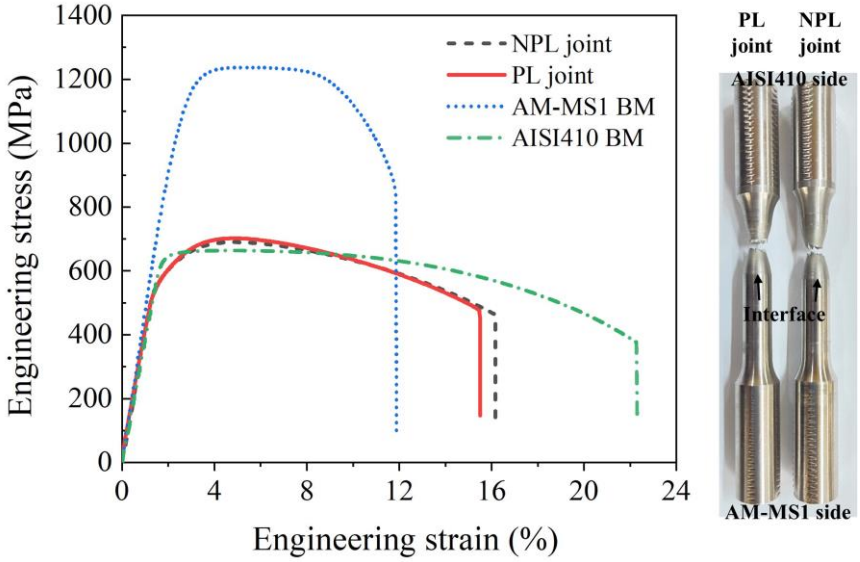

Fig. 5.11. Engineering stress-strain curves and the fracture appearance of the joints

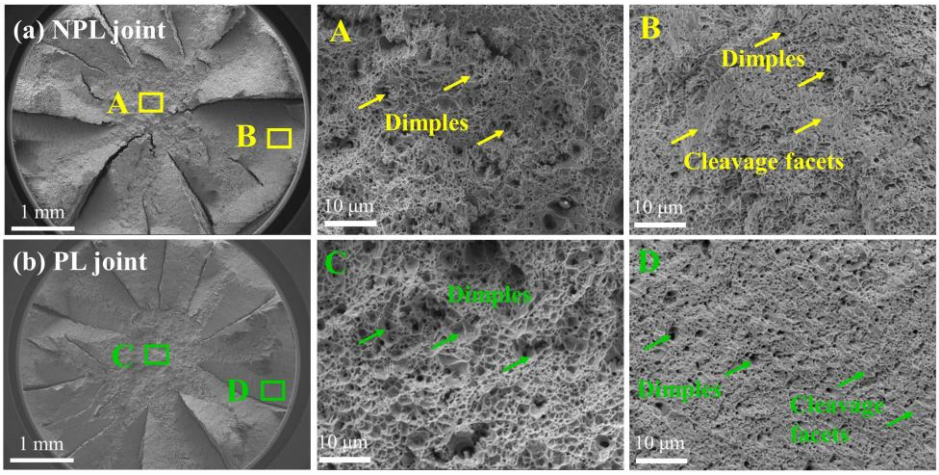

Fig. 5.12. Fracture surface of the representative joint (PL joint)

5.4 CONCLUSIONS

In the present study, AMed maraging steel and conventional martensite stainless steel (AISI410) cylindrical specimens were solid-state joined through EAPJ. The effectiveness of the AMed porous layer on the joining was verified by comparing NPL joining with PL joining.

The process response during EAPJ, interfacial characteristics, and mechanical behavior were discussed. The AMed porous layer effectively and locally increased the electrical resistance at the joining interface, which dramatically increased the maximum temperature and significantly reduced the joining load. The result shows that the porous layer also significantly increased the diffusion thickness, which can strengthen the interfacial joint strength. For both the NPL and PL joints, the microhardness reduction in the AM-MS1 side was attributed to the release of the high residual stress from AM, while the high amount of martensite formation in the AISI410 side resulted in a dramatic increase in microhardness. Both joints were fractured in the transition region between the heat-affected region and unaffected region of the AISI410 side. The approach suggested in the present study can enhance the efficiency of EAPJ, which can be an effective alternative to conventional fusion joining or other high-cost and time-consuming solid-state joining techniques, such as diffusion joining in a furnace or friction welding.

The present study clearly demonstrates the benefits of using a AMed porous layer during EAPJ of a dissimilar material combination. The temperature can be more effectively and locally controlled, thus the material flow can be more properly controlled at the expected local area to achieve more asymmetric deformation with respect to the interface. The control of material flow is especially crucial in the solid-state joining of a dissimilar material combination with highly different mechanical properties. Additionally, the joining load can be dramatically decreased, which reduces the required capacity of the joining facility in practical applications.

REFERENCES

[1] N. Chen, H.-P. Wang, M. Wang, B.E. Carlson, D.R. Sigler, Schedule and electrode design for resistance spot weld bonding Al to steels, Journal of Materials Processing Technology 265 (2019) 158-172.

[2] S. Zhang, K. Gao, S.-T. Hong, H. Ahn, Y. Choi, S. Lee, H.N. Han, Electrically assisted solid state lap joining of dissimilar steel S45C and aluminum 6061-T6 alloy, Journal of Materials Research and Technology 12 (2021) 271-282.

[3] H.-J. Jeong, J.-w. Park, K.J. Jeong, N.M. Hwang, S.-T. Hong, H.N. Han, Effect of Pulsed Electric Current on TRIP-Aided Steel, International Journal of Precision Engineering and Manufacturing-Green Technology 6(2) (2019) 315-327.

[4] M.-J. Kim, S. Yoon, S. Park, H.-J. Jeong, J.-W. Park, K. Kim, J. Jo, T. Heo, S.-T. Hong, S.H. Cho, Y.-K. Kwon, I.-S. Choi, M. Kim, H.N. Han, Elucidating the origin of electroplasticity in metallic materials, Applied Materials Today 21 (2020).

[5] H.-J. Jeong, M.-J. Kim, S.-J. Choi, J.-W. Park, H. Choi, V.T. Luu, S.-T. Hong, H.N. Han, Microstructure reset-based self-healing method using sub-second electric pulsing for metallic materials, Applied Materials Today 20 (2020).

[6] J.-W. Park, H.-J. Jeong, S.-W. Jin, M.-J. Kim, K. Lee, J.J. Kim, S.-T. Hong, H.N. Han, Effect of electric current on recrystallization kinetics in interstitial free steel and AZ31 magnesium alloy, Materials Characterization 133 (2017) 70-76.

[7] M.-J. Kim, M.-G. Lee, K. Hariharan, S.-T. Hong, I.-S. Choi, D. Kim, K.H. Oh, H.N. Han, Electric current–assisted deformation behavior of Al-Mg-Si alloy under uniaxial tension, Int. J. Plast. 94 (2017) 148-170.

[8] M.-K. Ng, L. Li, Z. Fan, R.X. Gao, E.F. Smith, K.F. Ehmann, J. Cao, Joining sheet metals by electrically-assisted roll bonding, CIRP Annals 64(1) (2015) 273-276.

[9] Y.-F. Li, H. Das, S.-T. Hong, J.-W. Park, H.N. Han, Electrically assisted pressure joining of titanium alloys, Journal of Manufacturing Processes 35 (2018) 681-686.

[10] S.Y. Anaman, S. Ansah, Y.-F. Li, H.-H. Cho, J.-S. Lee, H.N. Han, S.-T. Hong, Experimental and numerical studies on the electrochemical properties of an electrically assisted pressure joint of austenitic stainless steel and Ni-based superalloy, Materials Characterization 165 (2020).

[11] A. Saboori, A. Aversa, G. Marchese, S. Biamino, M. Lombardi, P. Fino, Application of Directed Energy Deposition-Based Additive Manufacturing in Repair, Applied Sciences 9(16) (2019).

[12] C. Molina, A. Araujo, K. Bell, P.F. Mendez, M. Chapetti, Fatigue life of laser additive manufacturing repaired steel component, Eng. Fract. Mech. 241 (2021).

[13] Y. Yao, K. Wang, X. Wang, L. Li, W. Cai, S. Kelly, N. Esparragoza, M. Rosser, F. Yan, Microstructural heterogeneity and mechanical anisotropy of 18Ni-330 maraging steel fabricated by selective laser melting: The effect of build orientation and height, J. Mater. Res. 35(15) (2020) 2065-2076.

[14] E. Cyr, H. Asgari, S. Shamsdini, M. Purdy, K. Hosseinkhani, M. Mohammadi, Fracture behaviour of additively manufactured MS1-H13 hybrid hard steels, MatL 212 (2018) 174-177.

[15] T. Allam, K.G. Pradeep, P. Köhnen, A. Marshal, J.H. Schleifenbaum, C. Haase, Tailoring the nanostructure of laser powder bed fusion additively manufactured maraging steel, Additive Manufacturing 36 (2020).

[16] L. Kučerová, I. Zetková, Š. Jeníček, K. Burdová, Hybrid parts produced by deposition of 18Ni300 maraging steel via selective laser melting on forged and heat treated advanced high strength steel, Additive Manufacturing 32 (2020).

[17] L. Kučerová, I. Zetková, A. Jandová, M. Bystrianský, Microstructural characterisation and in-situ straining of additive-manufactured X3NiCoMoTi 18-9-5 maraging steel, Materials Science and Engineering: A 750 (2019) 70-80.

[18] J. Lee, J. Choe, J. Park, J.-H. Yu, S. Kim, I.D. Jung, H. Sung, Microstructural effects on the tensile and fracture behavior of selective laser melted H13 tool steel under varying conditions, Materials Characterization 155 (2019).

[19] J. Zhang, Z. Liu, J. Sun, H. Zhao, Q. Shi, D. Ma, Microstructure and mechanical property of electropulsing tempered ultrafine grained 42CrMo steel, Materials Science and Engineering: A 782 (2020).

[20] B. Vamsi Krishna, A. Bandyopadhyay, Surface modification of AISI 410 stainless steel using laser engineered net shaping (LENSTM), Materials & Design 30(5) (2009) 1490-1496.

[21] J. Samei, H. Asgari, C. Pelligra, M. Sanjari, S. Salavati, A. Shahriari, M. Amirmaleki, M. Jahanbakht, A. Hadadzadeh, B.S. Amirkhiz, M. Mohammadi, A hybrid additively manufactured martensitic-maraging stainless steel with superior strength and corrosion resistance for plastic injection molding dies, Additive Manufacturing 45 (2021).

[22] Y. Bai, C. Zhao, Y. Zhang, H. Wang, Microstructure and mechanical properties of additively manufactured multi-material component with maraging steel on CrMn steel, Materials Science and Engineering: A 802 (2021).

[23] S. Tabaie, F. Rézaï-Aria, B.C.D. Flipo, M. Jahazi, Dissimilar linear friction welding of selective laser melted Inconel 718 to forged Ni-based superalloy AD730™: Evolution of strengthening phases, Journal of Materials Science & Technology 96 (2022) 248-261.

[24] S.-T. Hong, Y.-F. Li, J.-W. Park, H.N. Han, Effectiveness of electrically assisted solid-state pressure joining using an additive manufactured porous interlayer, CIRP Annals 67(1) (2018) 297-300.

[25] Y.-F. Li, S.-T. Hong, H. Choi, H.N. Han, Solid-state dissimilar joining of stainless steel 316L and Inconel 718 alloys by electrically assisted pressure joining, Materials Characterization 154 (2019) 161-168.

[26] M.-G. Jo, T.A.N. Nguyen, S. Park, J.-Y. Suh, S.-T. Hong, H.N. Han, Electrically Assisted Solid-State Joining of CrMnFeCoNi High-Entropy Alloy, MMTA 51(12) (2020) 6142-6148.

[27] H. Shi, S. Qiao, R. Qiu, X. Zhang, H. Yu, Effect of Welding Time on the Joining Phenomena of Diffusion Welded Joint between Aluminum Alloy and Stainless Steel, MMP 27(12) (2012) 1366-1369.

[28] S. Rajakumar, V. Balasubramanian, Diffusion bonding of titanium and AA 7075 aluminum alloy dissimilar joints—process modeling and optimization using desirability approach, The International Journal of Advanced Manufacturing Technology 86(1-4) (2016) 1095-1112.

[29] G. Mahendran, S. Babu, V. Balasubramanian, Analyzing the Effect of Diffusion Bonding Process Parameters on Bond Characteristics of Mg-Al Dissimilar Joints, Journal of Materials Engineering and Performance 19(5) (2009) 657-665.

[30] G.M. Castro Güiza, C.A.S. Oliveira, Microstructural changes produced by hot forging in a C300 Maraging Steel, Materials Science and Engineering: A 655 (2016) 142-151.

[31] R. Song, D. Ponge, D. Raabe, R. Kaspar, Microstructure and crystallographic texture of an ultrafine grained C–Mn steel and their evolution during warm deformation and annealing, AcMat 53(3) (2005) 845-858.

[32] A.K. Pramanick, H. Das, J.-W. Lee, Y. Jung, H.-H. Cho, S.-T. Hong, M. Shome, A.K. Pramanick, Texture analysis and joint performance of laser-welded similar and dissimilar dual-phase and complex-phase ultra-high-strength steels, Materials Characterization 174 (2021).

[33] K. Radwański, Structural characterization of low-carbon multiphase steels merging advanced research methods with light optical microscopy, Archives of Civil and Mechanical Engineering 16(3) (2016) 282-293.

[34] A. Ramazani, P.T. Pinard, S. Richter, A. Schwedt, U. Prahl, Characterisation of microstructure and modelling of flow behaviour of bainite-aided dual-phase steel, Computational Materials Science 80 (2013) 134-141.

[35] V. Tsisar, M. Kondo, T. Muroga, T. Nagasaka, I. Matushita, Morphological and compositional features of corrosion behavior of SUS410–SUS410, SUS316–SUS316 and SUS410–SUS316 TIG welded joints in Li, Fusion Eng. Des. 87(4) (2012) 363-368.

[36] M. Tsai, C. Chiou, J. Du, J.J.M.S. Yang, E. A, Phase transformation in AISI 410 stainless steel, 332(1-2) (2002) 1-10.

[37] C. Chen, X. Yan, Y. Xie, R. Huang, M. Kuang, W. Ma, R. Zhao, J. Wang, M. Liu, Z. Ren, H. Liao, Microstructure evolution and mechanical properties of maraging steel 300 fabricated by cold spraying, Materials Science and Engineering: A 743 (2019) 482-493.

[38] L. Kučerová, K. Burdová, Š. Jeníček, I. Chena, Effect of solution annealing and precipitation hardening at 250 °C–550 °C on microstructure and mechanical properties of additively manufactured 1.2709 maraging steel, Materials Science and Engineering: A 814 (2021).

[39] Y. Yano, T. Tanno, Y. Sekio, H. Oka, S. Ohtsuka, T. Uwaba, T. Kaito, Tensile properties and hardness of two types of 11Cr-ferritic/martensitic steel after aging up to 45,000 h, Nuclear Materials and Energy 9 (2016) 324-330.

[40] A. Belyakov, Y. Kimura, Y. Adachi, K. Tsuzaki, Microstructure Evolution in Ferritic Stainless Steels during Large Strain Deformation, Materials Transactions 45(9) (2004) 2812-2821.

CHAPTER VI

MICROSTRUCTURE EVOLUTION AND FATIGU PERFORMANCE OF DISSIMILAR SOLID-STATE JOINTS OF SUS316L AND SUS410

6.1 INTRODUCTION

Joining dissimilar metals is becoming an important manufacturing technology to fabricate structures with integrated mechanical properties and high economic efficiency in various industrial applications [1]. Stainless steel 316L (SUS316L) is widely used to fabricate automobile components and medical instruments due to its high corrosion resistance, good workability, and high-temperature mechanical properties [2]. Stainless steel 410 (SUS410) is extensively used, owing to the excellent balance of high strength, corrosion resistance, and high resistance to wear [3,4]. However, these materials are also different in terms of chemical components, crystal structure, and coefficient of thermal expansion, causing high residual stress and shrinkage voids during melting and solidification in conventional fusion joining [5,6].

As an alternative to conventional fusion joining, solid-state joining is considered as a promising method in similar and dissimilar joining of metals due to its high joining efficiency and resultant joint strength. In general, solid-state joining can efficiently join metallic materials in solid-state through elemental diffusion under plastic deformation and associated heat input [7], thus avoiding microstructural defects, which frequently occur during fusion joining. Among various solid-state joining processes, pressure joining is one of the classical joining processes, which has been successfully utilized to join similar or dissimilar materials, generally at an elevated temperature with plastic deformation [8-11]. The most accepted

mechanism of pressure joining is the film theory, which was proposed by Bay [12] as follows: the plastic deformation breaks the oxide layer, which extrudes the virgin metal through micro-cracks and forms an intimate contact at the interface until bonding is established. Peter et al. [13] successfully joined carbon steel C15 with aluminum alloy EN AW6082 using cold pressure joining and explained the bonding mechanism using the extended Bay model at the atomic level. Pawlicki et al. [10] investigated the possibility of joining pure copper M1E to pure aluminum EN AW1100 and aluminum AW1100 to aluminum AW1100 using a cold upset forging process under different surface preparation. Except in cold pressure joining, elevated temperature plays a vital role in pressure joining since it can enhance elemental diffusion and reduce the required force during plastic deformation. In conventional hot pressure joining, the specimens need to be pre-heated in a furnace for a few hours. Additionally, the thermal energy is applied to the entire specimen assembly, causing unavoidable microstructural changes to the whole specimen assembly. Therefore, it is crucial to develop a controllable and more efficient heating method to improve the joining efficiency and minimize the damage to the surrounding area of the joint interface.

Electrically assisted pressure joining (EAPJ) provides not only the advantages of faster and localized heating but also the athermal effect (so-called electroplastic effect) of electric current. The athermal effect of electric current has been reported to enhance the kinetics of metal atoms, thus accelerating or inducing annealing [14,15], aging [15], recrystallization [16], and microstructure healing [17], in addition to the well-known thermal effect of resistance heating. Kim et al. [18] recently demonstrated that the athermal effect of electric current could be explained by the weakening of atomic bonding due to a charge imbalance near defects. Peng et al. [7] established a prediction model of shear strength for EAPJ by successfully

joining stainless steel and brass sheets using electrically assisted solid-state welding. Hong et al. [19] joined SUS316L by EAPJ using an additive manufactured porous interlayer and analyzed the microstructural change. Li et al. [20] experimentally investigated the joining of SUS316L and Inconel 718 and observed the base metal fracture during the tensile test. Moreover, Zhang et al. [21] successfully joined dissimilar steel S45C and aluminum 6061-T6 alloy in solid state by means of EAPJ and investigated the effect of current density on joint performance. They concluded that the different interfacial joint strengths were due to the formation of different IMCs having a different relative thickness for the given material combination.

Even with recent successful studies on EAPJ joining, most of the studies have investigated the static mechanical behavior and the microstructural changes of joints. The dynamic fatigue performance of EAPJ joints has been reported rarely. However, joints can have significantly different behavior under cyclic loading conditions due to their specific microstructures or defect formation in the joining area [22-24]. Therefore, investigating the fatigue performance of the EAPJ joints and their failure mechanism is crucial for the reliable application of the products during service time.

In the present study, the feasibility of EAPJ of SUS316L and SUS410 was investigated and the effects of electric current density on the joining performance were analyzed by static and dynamic mechanical testing and microstructural analysis. Specifically, the fatigue life was statistically analyzed using two-parameter Weibull distribution at a certain confidence level. The mechanism of fatigue failure was also characterized by observation of the fracture surface.

6.2 EXPERIMENTAL SET-UP

Cylindrical SUS316L and SUS410 specimens (Fig. 6.1) with identical dimensions (diameter: 16 mm; height: 58 mm) were used in the EAPJ experiment. The chemical composition and mechanical properties of the SUS316L and SUS410 base metals (BMs) are listed in Table 6.1 and Table 6.2, respectively. The EAPJ experiment with custom-made fixtures acting as electrodes was carried out on the custom-made servo press machine (DTU-800SP, Daekyung Teck & Testers, South Korea), as described in Fig. 6.1. The electric current was applied by a controllable generator during compression to provide resistance heating and induce the athermal effect of the electric current. A pair of insulators made of Bakelite was inserted between the crosshead of the servo press machine and the electrodes to protect the testing system. The specimens were ground using sandpaper and then cleaned by acetone to remove the oxide layer and contaminant from the surface before joining. During joining, the temperature variation was monitored by an infrared thermal imaging camera (FLIR-T621, FLIR, Sweden) and the load histories were recorded by the DAQ system equipped in the servo press machine.

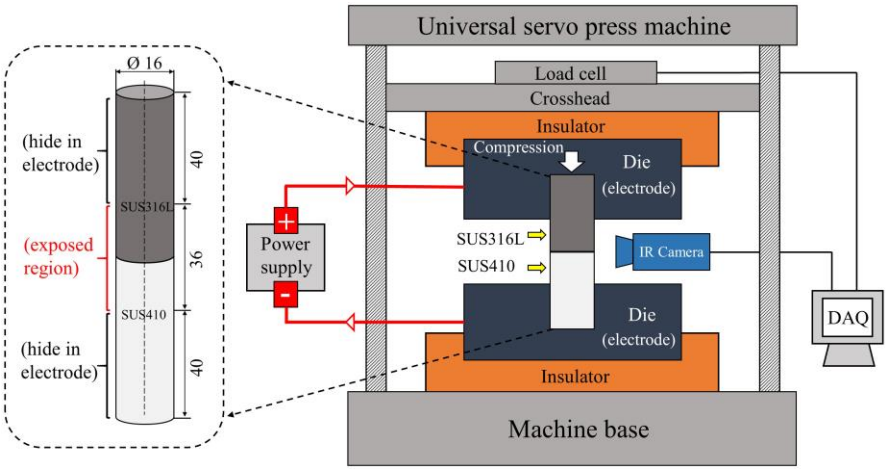

Fig. 6.1. Schematic of EAPJ experiment

Table 6.1. Chemical compositions of the materials (in wt%).

Elements	C	Mn	Si	S	P	Cr	Ni	Cu	Mo	Co	N	Fe
SUS316L	0.024	1.59	0.4	0.023	0.036	16.72	10.06	0.46	2.03	0.17	0.074	Bal.
SUS410	0.105	0.5	0.5	0.015	0.033	12.3	0.75	0.18	0.07	0.03	0.036	Bal.

Table 6.2. Mechanical properties of the materials.

Materials	UTS (MPa)	Yield strength (MPa)	Elongation (%)
SUS316L	714	620	45
SUS410	675	625	21

Continuous electric current (5 sec) was applied initially to the specimen assembly for rapid heating. The holding time (32.8 sec) with a pulsed electric current was utilized to maintain the elevated temperature, to enhance the diffusion, and to reduce the compressive force during compression, as shown in Fig. 6.2. After the electric current was turned off, the joint was cooled in the air. The displacement rate (24.7 mm/min) was kept constant during the EAPJ experiment. As listed in Table 6.3, three different initial continuous electric current densities (27.5, 32, and 34.5 A/mm^2) were adopted to investigate the effect of electric current density on the joint performance, while the current density for a pulsed electric current (14.2 A/mm^2) was consistent for all three conditions. Note that the electric current density used in the present study was calculated as the nominal electric current density, which is based on the original cross-sectional area of the specimen without deformation. For simplicity, the joints fabricated at different initial continuous electric current densities were labeled as J-27.5, J-32, and J-34.5. The other detailed parameters used in the EAPJ experiment are also summarized

in Table 6.3. At least three specimen assemblies were joined for each parameter set to verify the repeatability.

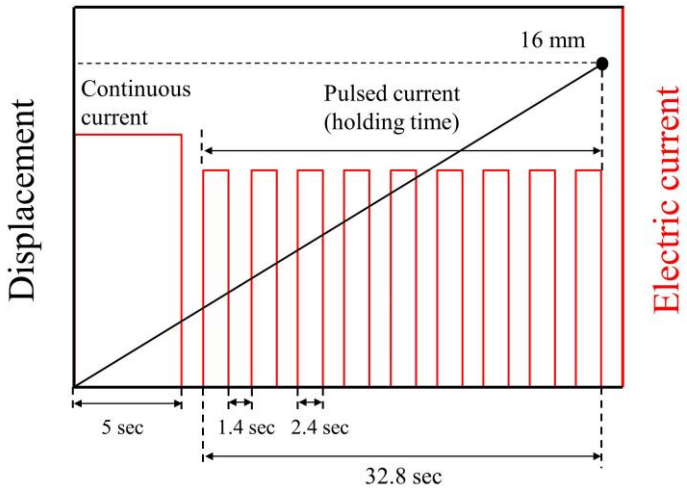

Fig. 6.2. Schematic of electric current and displacement histories during EAPJ

Table 6.3. Joining parameters of EAPJ.

Displacement rate (mm/min)	Compressive displacement (mm)	Continuous current density* (A/mm^2)	Duration of continuous current (sec)	Pulsed current density* (A/mm^2)	Holding time (sec)	Total joining time (sec)
24.7	16	27.5 32.0 34.5	5	14.2	32.8	39.2

* : Nominal value calculated based on the original cross-sectional area of the specimen without deformation.

Microstructure observation and mechanical tests for the joints were performed to assess the joining performance. Optical microscopy (OM) was used initially to evaluate the soundness of the joint interface. For OM, the cross section of the joint was ground to 1200 grit and polished with 1 μm and 0.25 μm diamond paste suspensions until a mirror-like final surface was achieved. The microstructure of each joint was examined at the interface using a field emission scanning electron microscope (FE-SEM: SU5000, Hitachi, Japan) equipped

with an energy dispersive spectrometer (EDS: X-Max50, Horiba, Japan) and electron backscatter diffractometer (EBSD: TSL Hikari Super, TSL, USA). The elemental diffusion across the interface was evaluated by SEM-EDS line scan, which indirectly indicates the joint strength. The operating conditions used in the EBSD analysis were an accelerating voltage of 20 eV, a probe current of 14 nA, a tilt angle of 70°, a working distance of 10 – 18 mm, and a step size of 0.12 – 0.7 μm. The inverse pole figure (IPF) maps, average grain size, grain orientation spread (GOS) maps, image quality (IQ) maps with the grain boundaries, kernel average misorientation (KAM) maps, and grain average image quality (GAIQ) maps and relevant distribution of the area fraction were obtained from EBSD testing. Additionally, in IQ maps, the misorientation angle for the low-angle grain boundary (LAGB) was set between 2° and 15°, and the high-angle grain boundary (HAGB) was set at angles greater than 15°. Vickers hardness was also measured (1 N, 10 sec) on the cross section at the joining center along the axial direction using a Vickers indenter (HM-200, Mitutoyo, Japan).

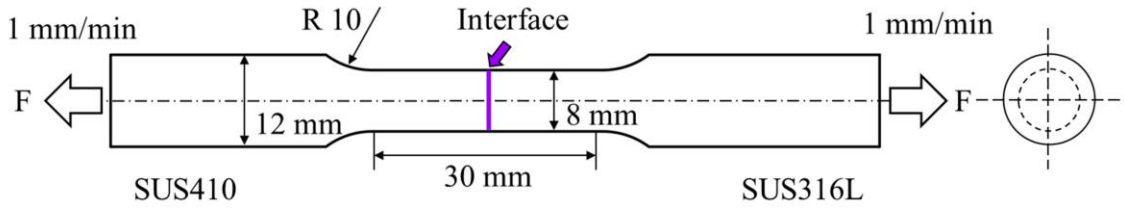

Fig. 6.3. Dimension of the specimen for quasi-static tensile test

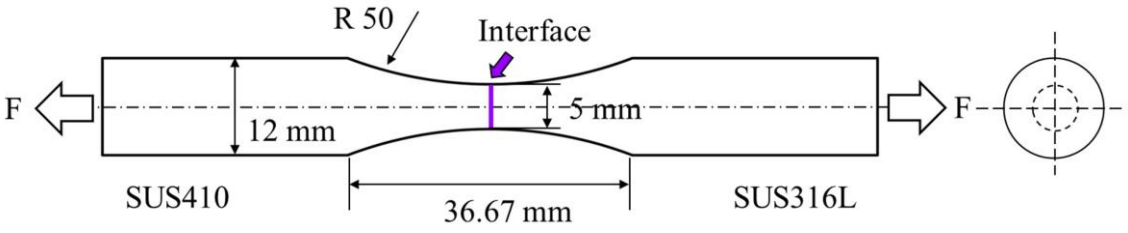

Fig. 6.4. Dimension of the specimen for fatigue test

To evaluate the joint strength, the specimens in standard "dog-bone" shape (ASTM E8/E8M) were prepared for quasi-static tensile tests with a constant displacement rate of 1 mm/min, as provided in Fig. 6.3. In fatigue tests, the force-controlled axial fatigue tests were conducted using the servo-hydraulic fatigue machine (MTS-322, MTS, USA) with a capacity of 100 kN to assess the fatigue behavior of the EAPJ joints. The joint was machined to a cylindrical shape (ASTM E466) with a continuous radius between ends to induce interfacial fracture, thus quantitatively assessing the fatigue behavior of the joint interface rather than BMs, as shown in Fig. 6.4. Prior to the fatigue test, the surfaces of specimens were ground using sandpaper up to the grade of #1200 to minimize the effects of machining scratches and surface roughness. In the fatigue test, the load frequency and stress ratio (R) were set to be 20 Hz and 0.1, respectively. The cut-off cycle of 8 million cycles was adopted as the infinite life or fatigue limit for EAPJ joints. The fracture surfaces from the failed specimens were examined using SEM to understand the failure mechanism under cyclic loading conditions.

In the statistical analysis of fatigue life, two-parameter Weibull distribution [25] was utilized to analyze the distribution of fatigue life at a certain confidence level. The well-known definition of the probability density function (PDF) f(N) in two-parameter Weibull distribution is given as

$$f(N) = \frac{\beta}{\alpha}\left(\frac{N}{\alpha}\right)^{\beta-1} e^{-\left(\frac{N}{\alpha}\right)^{\beta}} \quad (1)$$

where α represents the scale parameter or characteristic life and β represents the shape parameter or Weibull modulus [26]. Further, N is the fatigue life in the present study. By integrating the PDF, the cumulative density function (CDF) $F_f(N)$ can be written as

$$F_f(N) = 1 - e^{-\left(\frac{N}{\alpha}\right)^{\beta}} \quad (2)$$

where $F_f(N)$ represents the probability of failure at a given stress (0<F<1). Thus, the reliability function can be defined as

$$R(N) = 1 - F_f(N) = e^{-\left(\frac{N}{\alpha}\right)^{\beta}} \quad (3)$$

The following Eq. (4) can be obtained by taking the natural logarithm of both sides of Eq. (2).

$$\ln\ln\frac{1}{1-F_f(N)} = \beta \ln N - \beta \ln \alpha \quad (4)$$

Obviously, Eq. (4) describes the linear relationship between $\ln\ln\frac{1}{1-F_f(N)}$ and $\ln N$. The probability of failure $F_f(N)$ can be obtained by ranking the fatigue life from specimen number $i = 1$ to $i = n$, where i is the failure serial number and n is the total number of the specimens, as presented by Benard's Median Rank in Eq. (5) [27].

$$MR = F_f(N_i) = \frac{i-0.3}{n+0.4} \quad (5)$$

Hence, α and β can be calculated by linear regression in Eq. (4).

In Eq. (2), when $N = \alpha$, the probability that the fatigue life equals the characteristic life can be obtained as,

$$F(N) = 1 - e^{-(1)^{\beta}}$$

$$F(N) = 1 - 0.368$$

$$R(N) = 1 - F(N) = 0.368$$

where 36.8% is the reliability of the characteristic life. The fatigue life under different reliability at a certain stress can be calculated from Eq. (6).

$$N_{R(N)} = \alpha(-\ln R(N))^{\frac{1}{\beta}} \quad (6)$$

where $N_{R(N)}$ is the fatigue life considering the reliability R(N). In the present study, S-N curves with the reliability of 10, 36.8, 50, and 90% were calculated to guide the engineering application.

The mean time to failure (mean life, MTTF), standard deviation (SD), and coefficient of variation (CV) of two-parameter Weibull distribution were obtained from the following Eqs. (7)-(9), respectively.

$$\mathrm{MTTF} = \alpha\Gamma\left(1+\frac{1}{\beta}\right) \tag{7}$$

$$\mathrm{SD} = \alpha\sqrt{\Gamma\left(1+\frac{2}{\beta}\right) - \Gamma^2\left(1+\frac{1}{\beta}\right)} \tag{8}$$

$$CV = \frac{\mathrm{SD}}{\mathrm{MTTF}} = \frac{\alpha\sqrt{\Gamma\left(1+\frac{2}{\beta}\right)-\Gamma^2\left(1+\frac{1}{\beta}\right)}}{\alpha\Gamma\left(1+\frac{1}{\beta}\right)} \tag{9}$$

Here, Γ () is the gamma function [28].

6.3 RESULTS AND DISCUSSION

In EAPJ, the peak temperature was reached in 5 sec and then was maintained for 32.8 sec (holding time) at the elevated temperature by applying a pulsed current (Fig. 6.5(a)). During joining, due to the different electrical resistances of SUS316L and SUS410, the temperature distribution became asymmetric with respect to the joining interface, as shown in the exemplary temperature distribution along the axial direction (from A to B, SUS410 side to SUS316L side) in the inset of Fig. 6.5(a). In addition to the asymmetric temperature distribution, the different high-temperature mechanical properties of those two alloys resulted in asymmetric deformation with respect to the joining interface, which again exacerbated the

asymmetry of temperature distribution. Due to the asymmetric temperature distribution, the temperature histories in Fig. 6.5(a) were constructed using the maximum temperature in the exposed region at each instant, which always occurred on the SUS316L side. As shown in the temperature histories in Fig. 6.5(a), the initial peak temperature during joining increased with the increase of the nominal electric current density. Initial peak temperatures of about 800 °C, 1000 °C, and 1180 °C were obtained (in the SUS316L side) at nominal electric current densities of 27.5 A/mm^2, 32 A/mm^2, and 34.5 A/mm^2, respectively. During the holding time, the elevated temperature was maintained at a nearly constant value for 27.5 A/mm^2 or slowly decreased for 32 A/mm^2 and 34.5 A/mm^2.

The compressive load histories (Fig. 6.5(b)) during EAPJ show that the compressive load increased rapidly in the first few seconds and then dropped abruptly to a very low value. The sharply reduced compressive load indicates that the material deformation resistance was significantly reduced due to the combined effect of the direct thermal softening from resistance heating and the athermal effect of electric current [15,29]. As expected, with the increase of nominal electric current density, the load history showed a softer behavior (i.e., a lower initial peak load and lower loads during holding time). Naturally, for all three nominal electric current densities, with further increase of compressive displacement, the compressive load gradually increased. After EAPJ, asymmetric deformation was observed for the J-27.5 joint, while both the J-32 and J-34.5 joints exhibited relatively symmetric deformation (Fig. 6.6).

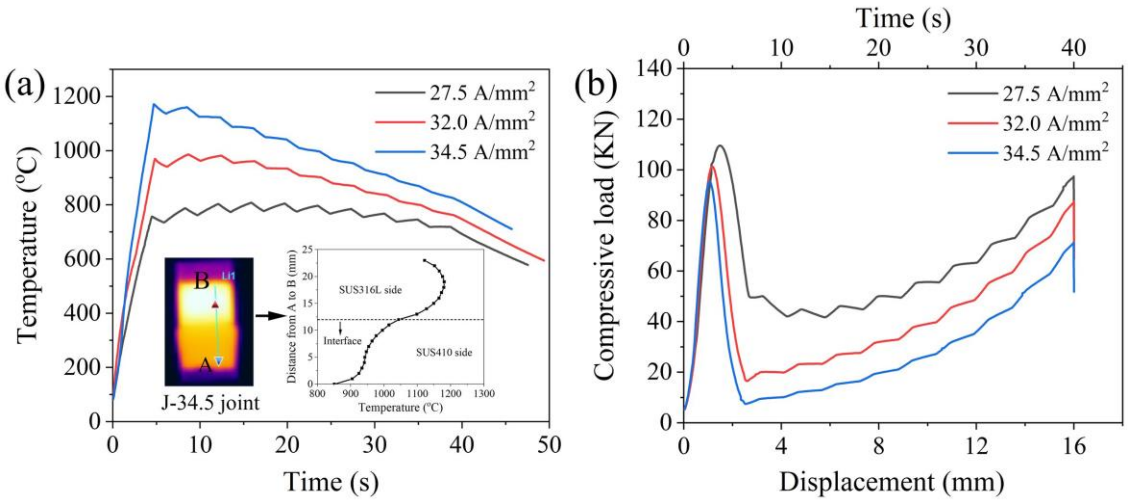

Fig. 6.5. Process response during EAPJ: (a) temperature histories and (b) load histories

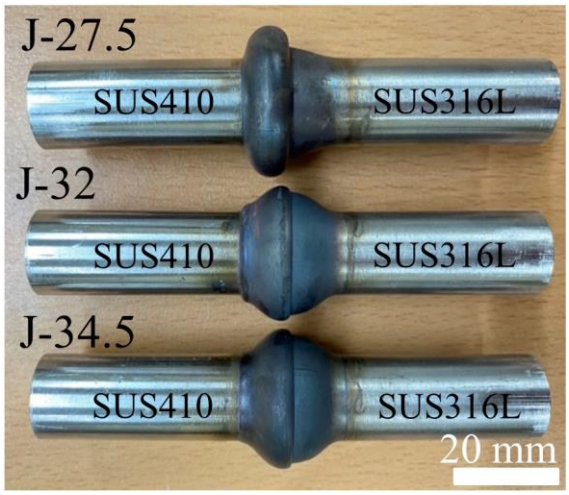

Fig. 6.6. The appearance of the EAPJ joints

The OM images of the cross sections of the joints from the center region along the axial direction suggest that sound solid-state joints were fabricated by EAPJ without macro-defects, as shown in Fig. 6.7. The asymmetric deformation of the J-27.5 joint suggests that the mechanical properties of SUS410 were much lower than those of SUS316L under the joining

condition with electric current density of 27.5 A/mm^2. Furthermore, SUS316L and SUS410 exhibit relatively symmetric deformation for both J-32 and J-34.5 joints, which suggested that the mechanical properties of both SUS316L and SUS410 became similar under the joining condition with higher electric current densities (32 and 34.5 A/mm^2).

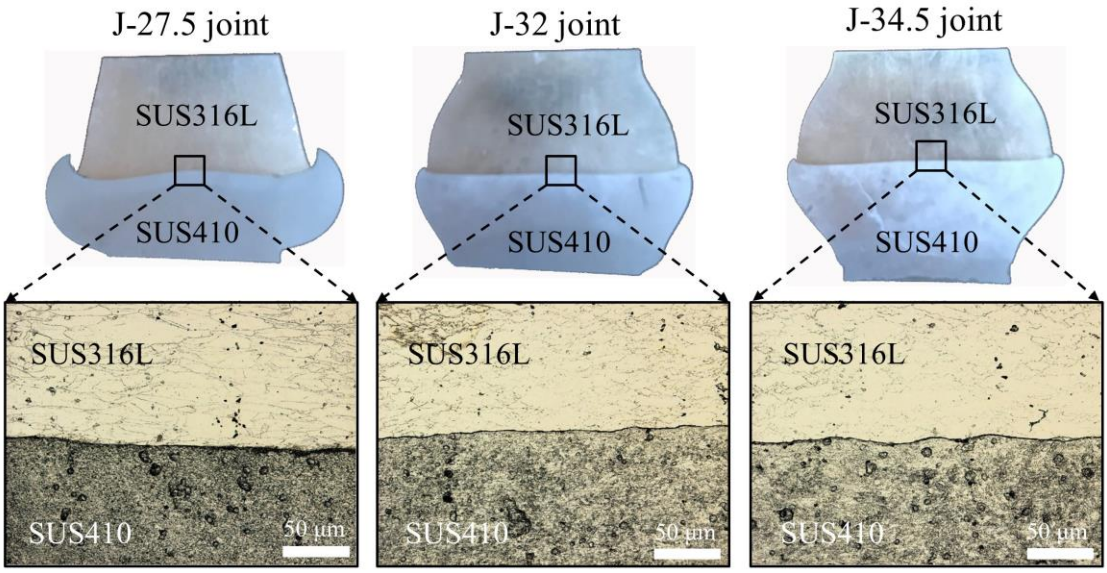

Fig. 6.7. The cross section and OM images of each joint

As indicated in the backscatter electron (BSE) images in Fig. 6.8, the elemental diffusion across the joint interface observed by EDS line scan shows that the diffusion thickness (marked by the short-dashed line) was highly affected by the applied electric current density. Note that the diffusion thickness was measured using the intensity changes of Mo and Ni since their concentration gradients were largest. As indicated in Fig. 6.8, the diffusion thickness was significantly increased by increasing the current density from 27.5 A/mm^2 to 32 A/mm^2. The increased diffusion thickness was attributed to the enhanced atomic diffusion

induced by the higher electric current density. However, further increasing the current density (from 32 to 34.5 A/mm^2) did not enhance the diffusion much further.

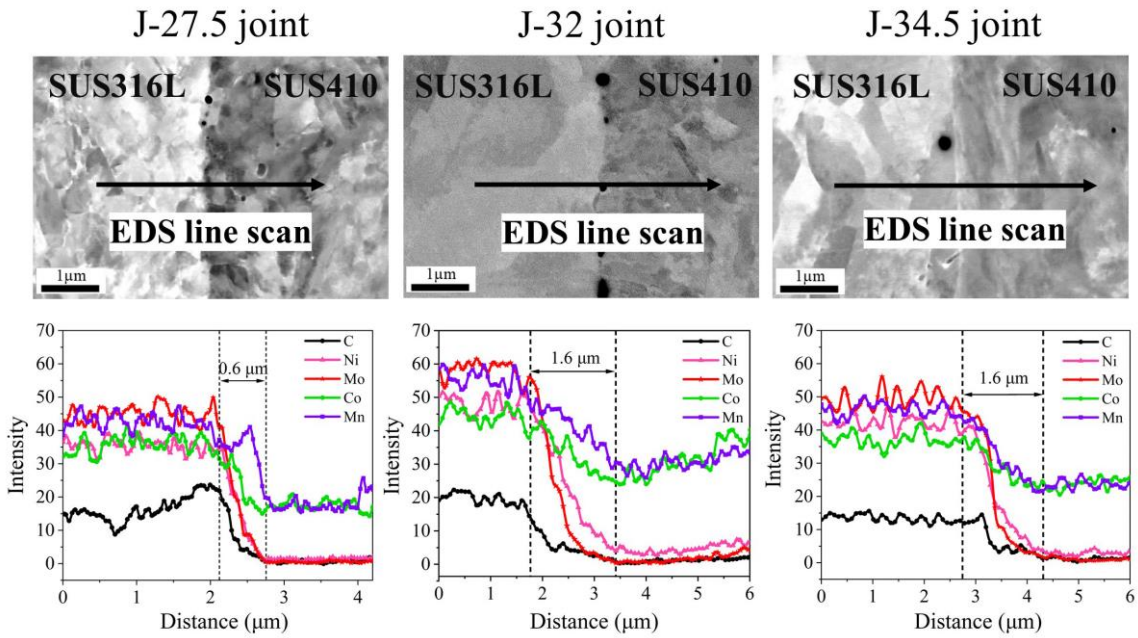

Fig. 6.8. The backscatter electron (BSE) images and results of EDS line scan across the interface

EBSD IPF and GOS maps observed from the center region of the interface for each joint and BMs are shown in Fig. 9. The IPF maps of BMs in Fig. 6.9(a) show that both SUS316L and SUS410 BMs are composed of equiaxed and homogeneously orientated grains (SUS316L BM: austenite; SUS410 BM: ferrite) [30,31]. For the J-27.5 joint (Fig. 6.9(c)), both the obviously deformed and equiaxed refined grains along the interface were observed at SUS316L and SUS410 sides, suggesting that the recrystallization occurred during EAPJ on both sides. As indicated in Figs. 6.9(c) and 10, the gradual increase of grain size suggests that the grain growth occurred with increased electric current density (for J-32 and J-34.5) for both

SUS316L and SUS410 sides of the joint. In particular, the lath-shaped grains in the SUS410 side of both J-32 and J-34.5 joints suggest the formation of martensite [32]. A similar result was observed by Tsai et al. [33] in the experiment of heat treatment for AISI410 stainless steels. They conducted a series of continuous heating and cooling processes and concluded that dislocated lath martensite can form at a very low cooling rate by air cooling. The GOS

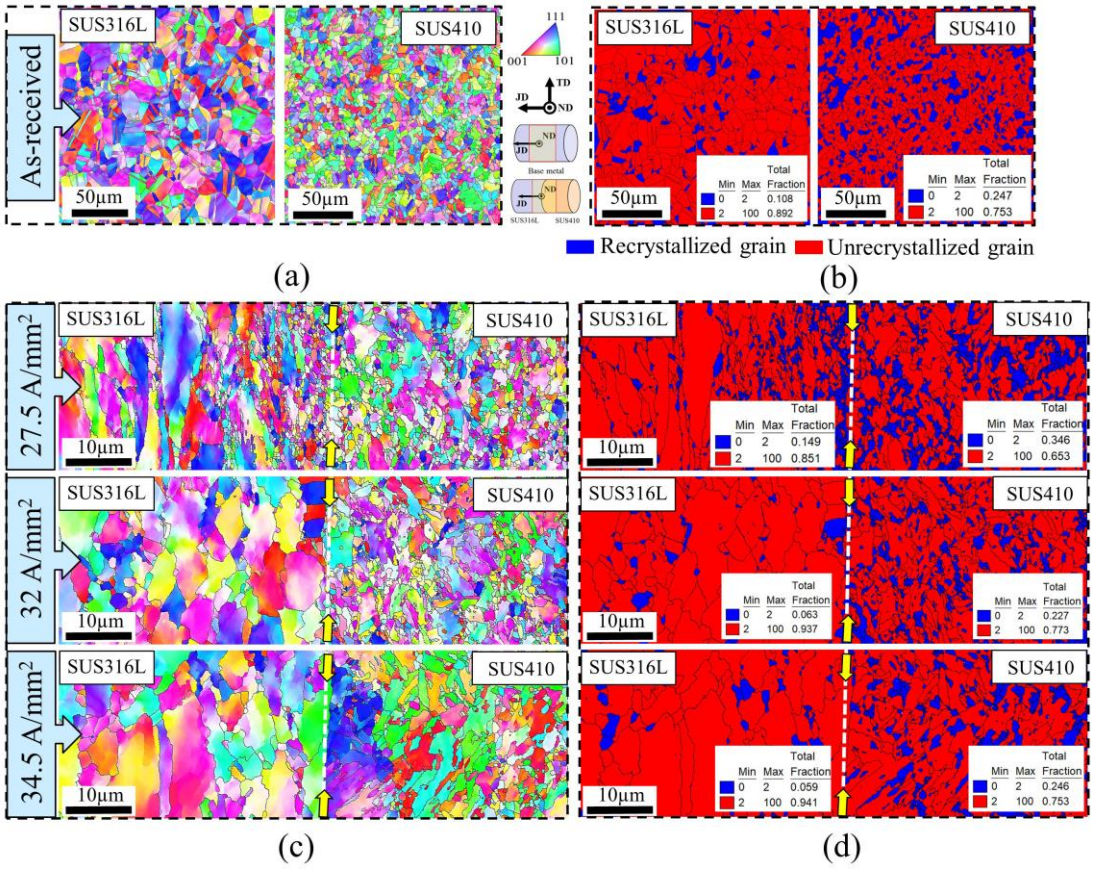

Fig. 6.9. EBSD IPF and GOS maps of both BMs and EAPJ joints: (a) IPF maps of the BMs; (b) GOS maps of the BMs; (c) IPF maps of the EAPJ joints; (d) GOS maps of the EAPJ joints. The blue and red color in the GOS maps indicate the recrystallized and unrecrystallized grains, respectively.

maps were used to quantitatively evaluate the recrystallization fraction. In the present study, grains with a GOS value of 0 – 2° were identified as the recrystallized grains, while grains with a GOS value > 2° were considered deformed grains [34]. The GOS maps (Figs. 6.9(b) and (d)) show that the recrystallized fraction of the J-27.5 joint for both sides significantly increased under the lowest electric current density of 27.5 A/mm^2 in comparison with BMs. This confirms the occurrence of recrystallization during the EAPJ under 27.5 A/mm^2. The lower fractions of recrystallization for the higher electric current densities (32 and 34.5 A/mm^2) can be explained by the recrystallization and following grain growth occurring much earlier than the completion of deformation under those higher electric current densities (or higher joining temperatures). Accordingly, the EDS line scan and EBSD analysis results confirm that the solid-state joining without micro-defects was formed through elemental diffusion and recrystallization during EAPJ.

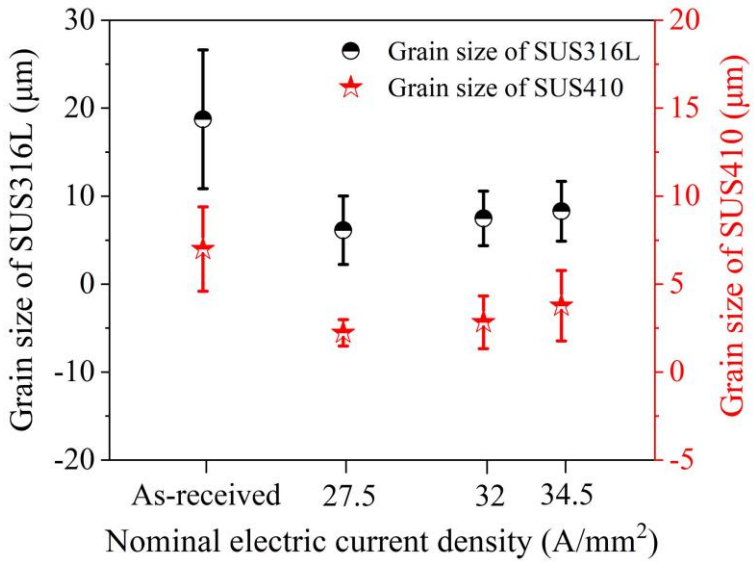

Fig. 6.10. The grain size change with the nominal electric current density

The annealing at each side of the joint was analyzed for all the joints using the variations of grain boundaries and the average KAM value (Fig. 6.11). The IQ maps with the distribution of HAGBs and LAGBs were obtained for both BMs (Fig. 6.11(a)) and both sides of joints (Fig. 6.11(c)). The IQ maps show that the HAGBs were dominant in both SUS316L and SUS410 BMs, while the joints had different distributions of HAGBs and LAGBs compared with the BMs for all three joints. The KAM maps of the BMs and EAPJ joints (Figs. 6.11(b) and (d)) show that the average KAM value of SUS316L of the J-27.5 joint (0.87) is higher than that of the SUS316L BM (0.73), which suggests that the SUS316L was not much annealed and highly strained under the current density of 27.5 A/mm^2. This is due to the fact that the peak temperature recorded in the SUS316L side (800 °C) during the joining with 27.5 A/mm^2 was significantly lower than the annealing temperature of SUS316L (1040 – 1175 °C [35]), even for the electrically induced annealing [17,36]. However, the average KAM values of SUS316L of the J-32 and J-34.5 joints (0.58 and 0.54, respectively) are significantly lower than that of the SUS316L BM, which indicates the occurrence of annealing in the SUS316L side of the J-32 and J-34.5 joints. The higher HAGBs-to-LAGBs ratios of the SUS316L of the J-32 and J-34.5 joints [1.01 and 0.93, respectively] in comparison with that of the J-27.5 joint [0.81] also confirms the occurrence of annealing. The average KAM values of the SUS410 side for all three joints are lower than that of the SUS410 BM, which suggests the occurrence of annealing in the SUS410 side for all three different EAPJ conditions. Once again, the annealing is confirmed by the fact that the HAGBs-to-LAGBs ratios of the SUS410 side for all three joints [J-27.5: 1.83; J-32: 1.76; J-34.5: 1.86] are higher than that of the SUS410 BM [1.55].

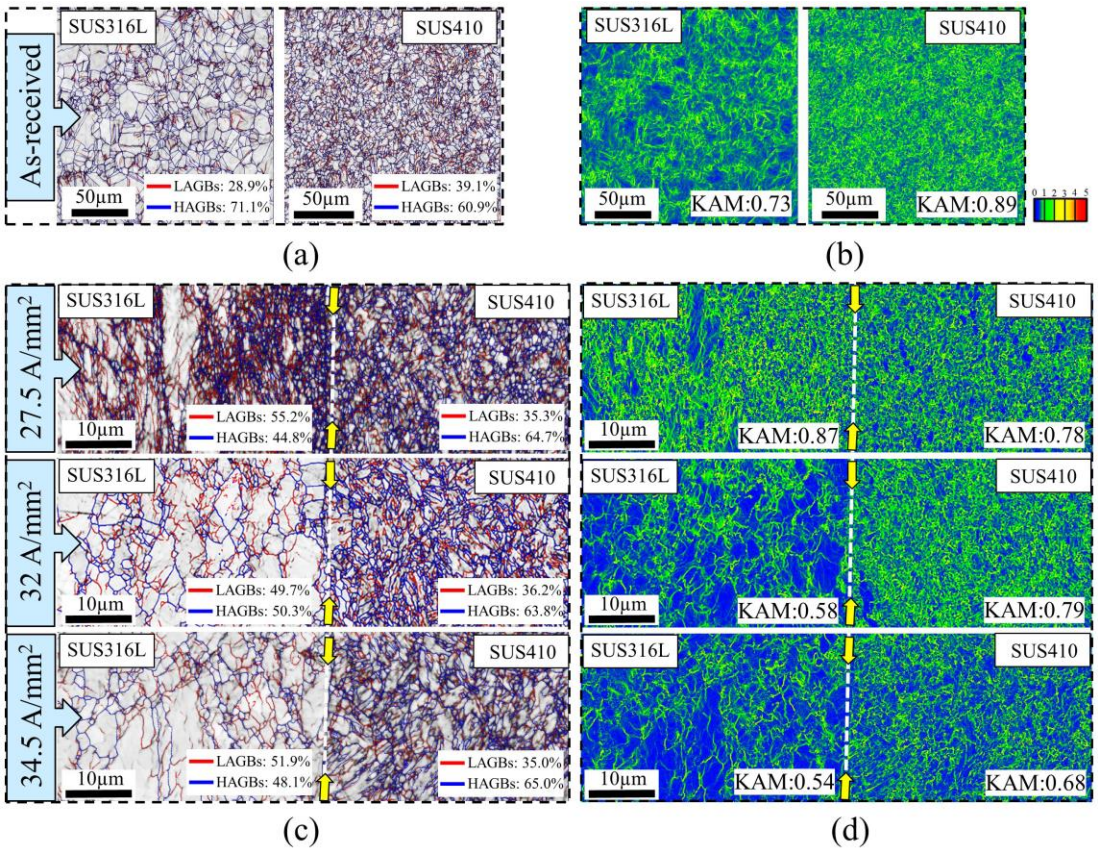

Fig. 6.11. IQ (overlaid with grain boundaries) maps and KAM maps of BMs and EAPJ joints: (a) IQ maps of the BMs; (b) KAM maps of the BMs; (c) IQ maps of the EAPJ joints; (d) KAM maps of the EAPJ joints

For the validation of the formation of lath-shaped martensite on the SUS410 side, the image quality (IQ) parameter is one way to differentiate the phases based on the degree of the lattice imperfection [37-39]. A crystal lattice with a higher amount of defects (for example, martensite) will show a lower IQ value, while the relatively perfect lattice of ferrite shows a higher IQ value. Ramazani [38] reported that grains with an average image quality lower than 4000 could be segmented as martensite in the GAIQ map while characterizing the

microstructure of bainite-aided dual-phase steel. In the present study, a GAIQ value of 5000 was adopted to distinguish the martensite from the ferrite matrix on the SUS410 side. The GAIQ maps and their relevant area fraction (Fig. 6.12) of the BMs show that the BMs are composed of nearly pure austenite and ferrite matrix, with a very small amount of martensite.

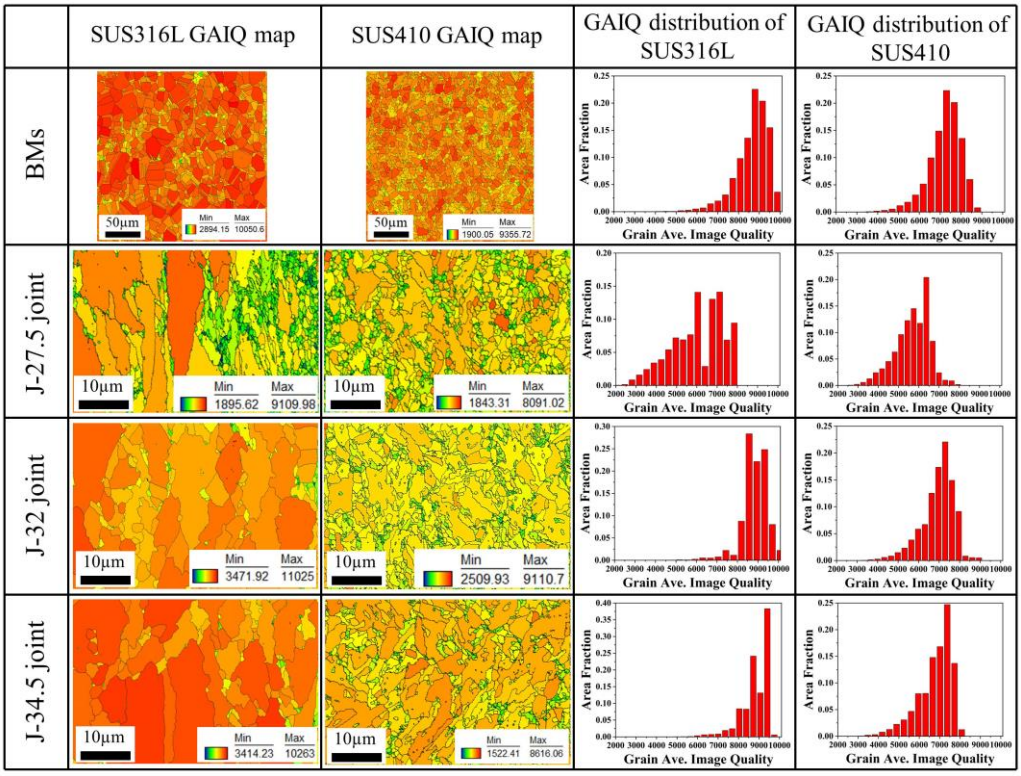

Fig. 6.12. Grain average image quality (GAIQ) maps and relevant distribution of area fraction for the BMs and EAPJ joints

For the J-27.5 joint, refined and nearly equiaxed grains with lower GAIQ values near the interface were observed, which indicates that some amount of martensite formed at the interface and embedded at the boundary of the large austenite and ferrite grains. Note that for

the J-27.5 joint, the area fraction of the martensite for the SUS316L side is higher than the SUS410 side, which can be seen by comparing the area fractions with a GAIQ value lower than 5000 in the distribution histogram. For both J-32 and J-34.5 joints, a nearly martensite-free phase was observed on the SUS316L side, while the SUS410 side still has the formation of the martensite. It is interesting to point out that the average grain sizes for J-32 and J-34.5 joints are higher than that for the J-27.5 joint on the SUS410 side. This may affect their relevant hardness and will be discussed below.

The microhardness distribution in Fig. 13 exhibits significant differences on SUS316L and SUS410 sides. In particular, the significantly increased hardness up to above 500 HV was observed for the J-32 and J-34.5 joints on the SUS410 side, while the J-27.5 joint shows a lower hardness value of about 300-350 HV. As reported by Jahromi et al. [40], the AISI410 stainless steel exhibits three different microstructures: fine ferrite, fine martensite, and coarse martensite after conventional heat treatment. They concluded that the fine martensite leads to a hardness value of about 347±8 HV, and coarse martensite leads to a hardness value of about 495±9 after quenching in air and oil, respectively. Thus, it can be speculated that the hardness obtained from the J-27.5 joint on the SUS410 side can be understood as the results of the formation of refined and nearly equiaxed martensite grains. With the grain growth (Fig. 6.10), the SUS410 for the J-32 and J-34.5 joints are hardened to above 500 HV due to the coarsening martensite. The increased hardness of the SUS316L side for the J-27.5 joint compared to the hardness of the SUS316L BM can be explained by the combination of grain refinement by recrystallization and the formation of fine martensite at the interface. However, with the increase of the current density, the grain growth of austenite and disappearance of martensite resulted in slight reduction of the hardness on the SUS316L side, as shown in Fig. 6.13.

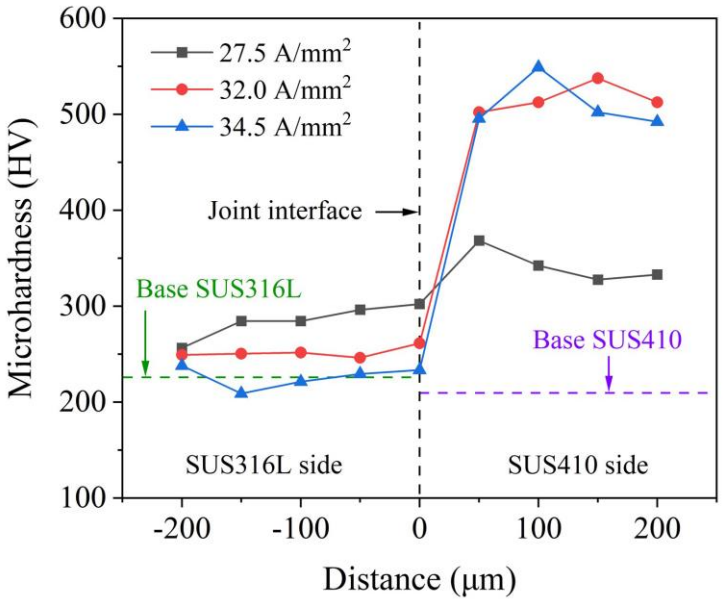

Fig. 6.13. Microhardness profiles of the EAPJ joints across the interface

In the tensile tests, three different fracture modes (interface fracture, SUS410 BM fracture, and SUS316L BM fracture) were observed depending on the joining parameters, as provided in Fig. 6.14. For the J-27.5 joint, interface fracture was observed during tension due to the insufficient diffusion (0.6 μm) under low current density. For both J-32 and J-34.5 joints, the increased diffusion thickness significantly increased the interfacial joint strength and resulted in the BM fracture. The maximum fracture strength of 676 MPa with SUS410 BM fracture was observed for the J-32 joint, while the J-34.5 joint with SUS316L BM fracture mode exhibited slightly lower fracture strength of 663 MPa. For the J-32 and J-34.5 joints, the different BM fracture modes can be explained by the competition of mechanical properties of the unaffected SUS410 BM, which was inserted inside the electrode during joining, and the heat-affected SUS316L, which was heated during joining (between the joint interface and the electrode). For the J-32 joint, the fracture occurred in the unaffected SUS410 BM, which was

inserted in the electrode during joining and consequently was not affected by joining. It suggests that the heat-affected SUS316L between the joint interface and the electrode was still stronger than the unaffected SUS410 BM. However, for the J-34.5 joint, the softening of the heat-affected SUS316L was severe enough to make the heat-affected SUS316L the weakest region, which generated a ductile fracture with UTS lower than that of the original (or unaffected) SUS316L BM.

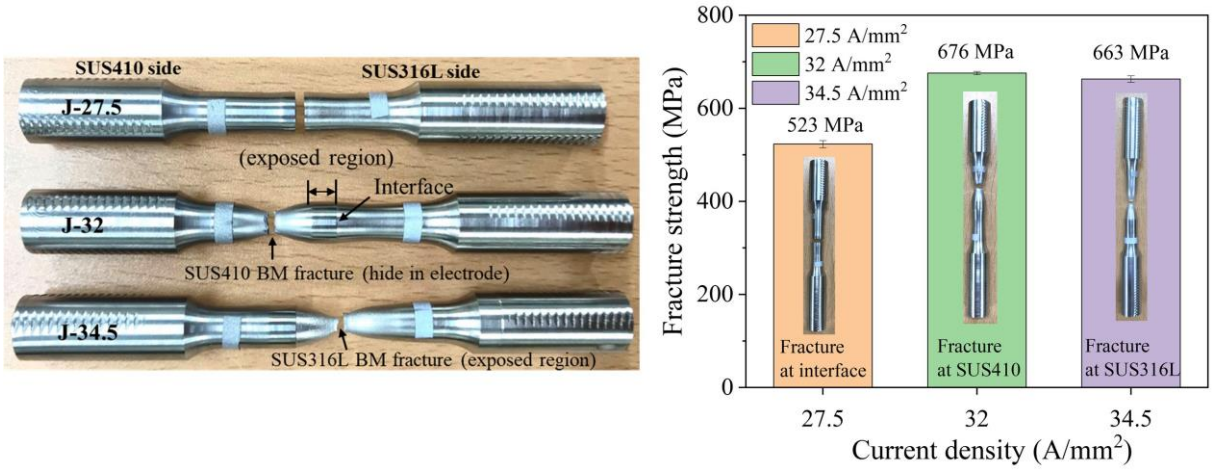

Fig. 6.14. Quasi-static tensile results of the EAPJ joints

The J-32 joints, which showed the maximum fracture strength with a fracture in the unaffected SUS410 BM in quasi-static tensile tests, were used for fatigue tests. The fatigue tests were performed under four different maximum cyclic stress levels (600, 580, 567, and 540 MPa) with a stress ratio of 0.1. Five results at each stress level were adopted for statistical analysis. The fatigue life N under each stress level and their corresponding $\ln N$ and $\ln \ln \frac{1}{1-F_f(N)}$ are presented in Table 6.4. The fatigue life range for 600, 580, and 567 MPa were 104, 105, and 106 orders of magnitude, respectively, as the symbol figure indicated in

Fig. 6.15. For 540 MPa tests, the specimens experienced 8 million cycles without fracture, so the tests were stopped. Naturally, the specimens under the other three stress levels fractured along the joint interface (Fig. 6.16) since the specimen was prepared to have stress concentration at the joint interface according to ASTM E466. The Weibull plots for these three conditions were then plotted as shown in Fig. 6.17, which can be used to calculate the scale parameter (α) and shape parameter (β) by linear regression ($y= \ln\ln\frac{1}{1-F_f(N)}$; $x=\ln N$). At each stress level, the slope of linear regression is equal to the shape parameter (β) and the scale parameter (α) can be obtained using Eq. (2). The MTTF and CV were also calculated from Eqs. (7)-(9). The Weibull parameters for each stress level are summarized in Table 6.5. Note that CV is a scatter representing fluctuations of the fatigue life under each stress level. It can be seen that the highest maximum cyclic stress has the smallest fluctuation (CV: 0.285), while the smallest maximum cyclic stress resulted in the largest fluctuation (CV: 0.482).

Table 6.4. The results of fatigue tests for J-32 joint.

Maximum cyclic stress (MPa)	Amplitude (MPa)	Fatigue life (cycles)	Benard's Median Rank	ln N	$\ln\ln\frac{1}{1-F_f(N)}$
600	270	51610	0.130	10.852	-1.975
		57316	0.315	10.956	-0.973
		68188	0.500	11.130	-0.367
		80208	0.682	11.292	0.145
		97696	0.870	11.490	0.715
580	261	254244	0.130	12.446	-1.975
		344634	0.315	12.750	-0.973
		359356	0.500	12.792	-0.367
		422790	0.682	12.955	0.145
		572009	0.870	13.257	0.715
567		1568800	0.130	14.266	-1.975
		1877824	0.315	14.446	-0.973
		1983234	0.500	14.500	-0.367
		3782665	0.682	15.146	0.145
		4020391	0.870	15.207	0.715
540		$>8x10^{6}$ *			

* : 5 specimens were repeated and all of them survived 8 x 10^6 cycles.

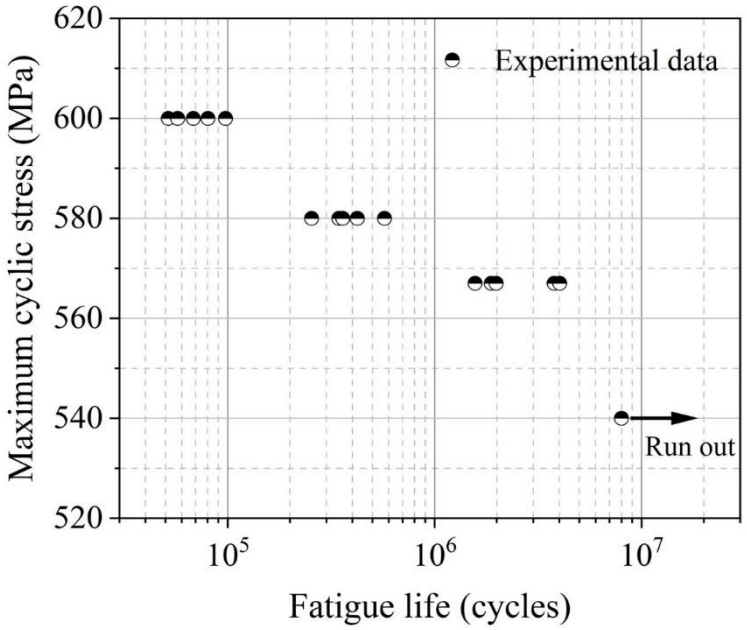

Fig. 6.15. The fatigue life obtained from experiments at different stress levels

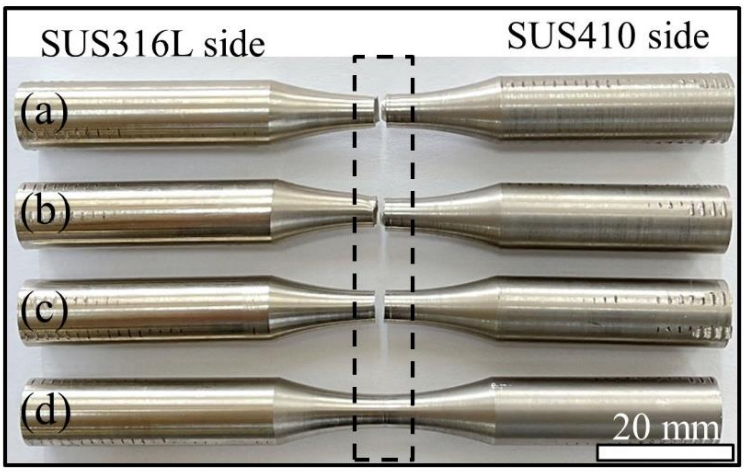

Fig. 6.16. Fatigue results at different stress levels: (a) 600 MPa; (b) 580 MPa; (c) 567 MPa; (d) 540 MPa

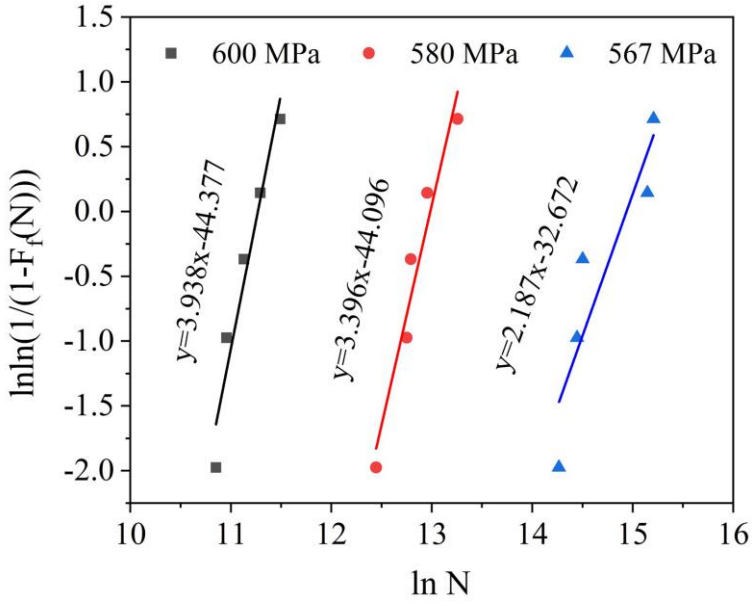

Fig. 6.17. Weibull plots for different maximum cyclic stress

Table 6.5. Weibull parameters, MTTF, and CV for each stress level

Maximum cyclic stress (MPa)	scale parameter (α)	shape parameter (β)	Mean fatigue life (MTTF) (cycles)	Coefficient of variation (CV)
600	78326	3.938	70932	0.285
580	435691	3.396	391393	0.325
567	3076139	2.187	2724264	0.482

Based on the parameters obtained from Weibull distribution analysis, the fatigue life considering the reliability levels can be calculated using Eq. (6). In the present study, the reliabilities of 10, 36.8, 50, and 90% were adopted to plot the S-N curves. For each reliability, the fatigue life was fitted by the following power function:

$$S_M = a\,(N)^b \qquad (10)$$

where SM represents the maximum cyclic stress. Further, a and b are both constants, which can be obtained by the least square fitting. The S-N curves with different reliabilities (Fig.

6.18) provide the possibility of fatigue life prediction, which is commonly required by the designer. Especially, the S-N curve with higher reliability (for example, 90%) is strongly recommended for industries requiring high safety levels.

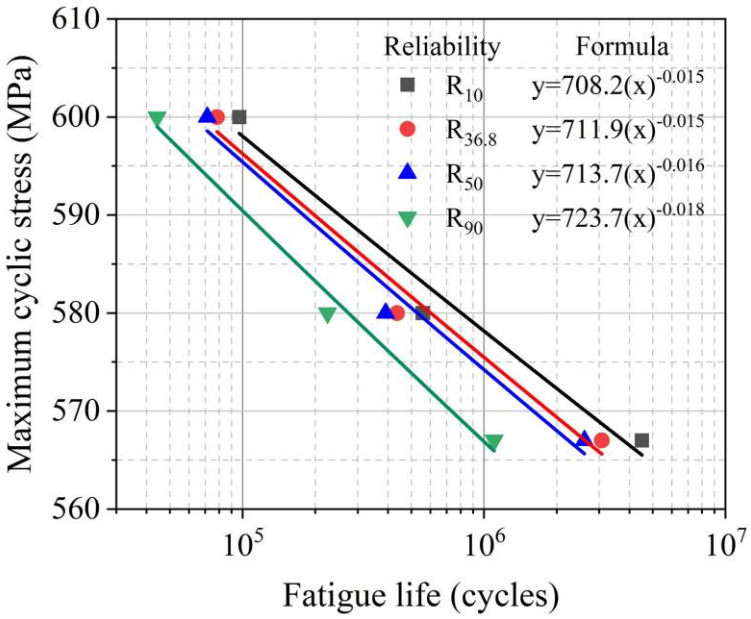

Fig. 6.18. S-N curves with different reliability levels

To understand the fracture mechanism of fatigue failure, the typical fracture appearance of the failed joints under the maximum cyclic stress of 600 and 567 MPa was observed using an SEM, as shown in Figs. 19 and 20. The fracture appearance (Fig. 6.19) failed under the cyclic stress level of 600 MPa (highest stress level) can be divided into two primary regions (A and C) according to their characteristics. Regions A and C are SUS316L BM and the joint interface, respectively. In region A, a huge amount of large dimples was observed on the fracture surface, indicating the occurrence of ductile fracture. Region C exhibits obvious fatigue striations, indicating the occurrence of fatigue crack propagation. The

transition boundary between regions A and C was identified as boundary B. As indicated in Fig. 6.19(B), fatigue cracks initiated from somewhere in region C and then propagated toward boundary B along the joint interface. Finally, the ductile fracture occurred in region A, where the remaining portion of the cross-section is made of SUS316L BM. Note that the heat-affected SUS316L BM has relatively low hardness compared to the heat-affected SUS410 BM, as shown in Fig. 6.13. Therefore, ductile fracture is more likely to occur in the SUS316L BM side under the maximum cyclic stress of 600 MPa.

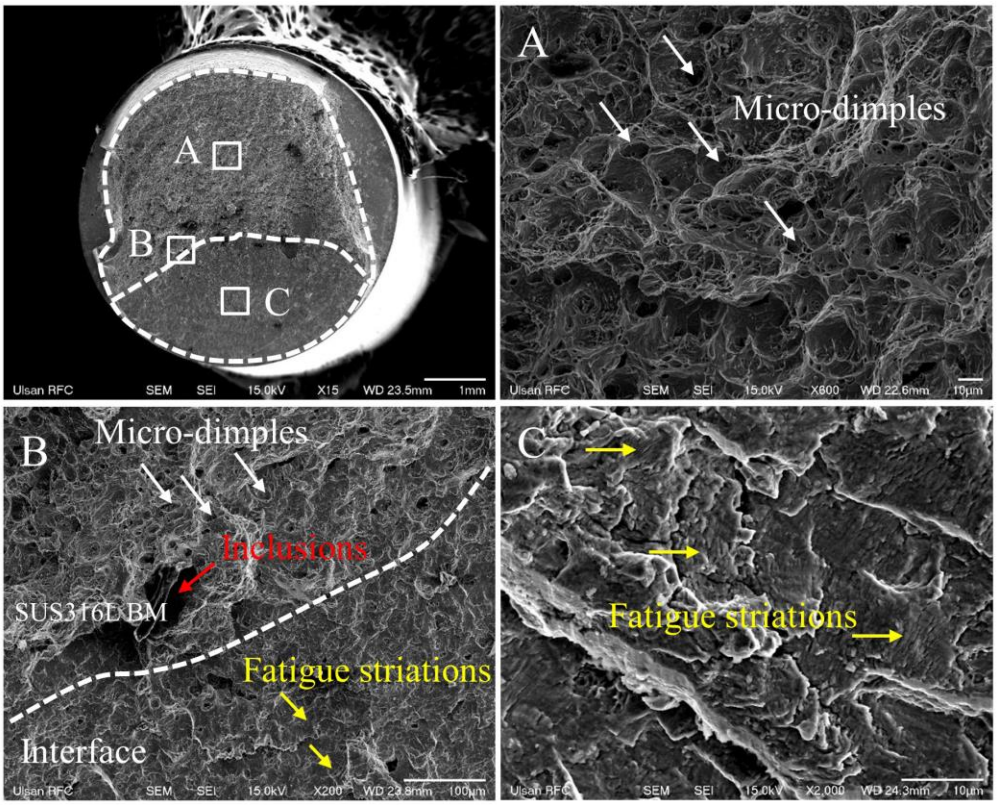

Fig. 6.19. Fracture appearance of the failed specimen under 600 MPa

In contrast, the fracture appearance of the specimen failed under the cyclic stress level of 567 MPa (lowest stress level with actual fatigue fracture) was somewhat different from that

presented in Fig. 6.19 and exhibited complete interfacial fracture (Fig. 6.20). The crack initiated from the surface region, marked by yellow dashed line, and then propagated into region A. The magnified view of region A shows both the fatigue striations and micro-cracks, which represents the occurrence of the fatigue crack propagations. Once the fatigue crack propagates into region B, the fracture mode changes from fatigue crack propagation to ductile fracture dominant mode. The magnified views of regions B and C show both the small-dimples and fatigue striations. Note that the fatigue striations can be seen only in a small portion of region B. As shown here, the fatigue behavior of the dissimilar EAPJ joint can vary significantly depending on not only the properties of the joint interface, but also the given cyclic stress level and the property of the heat-affected region near the joint interface.

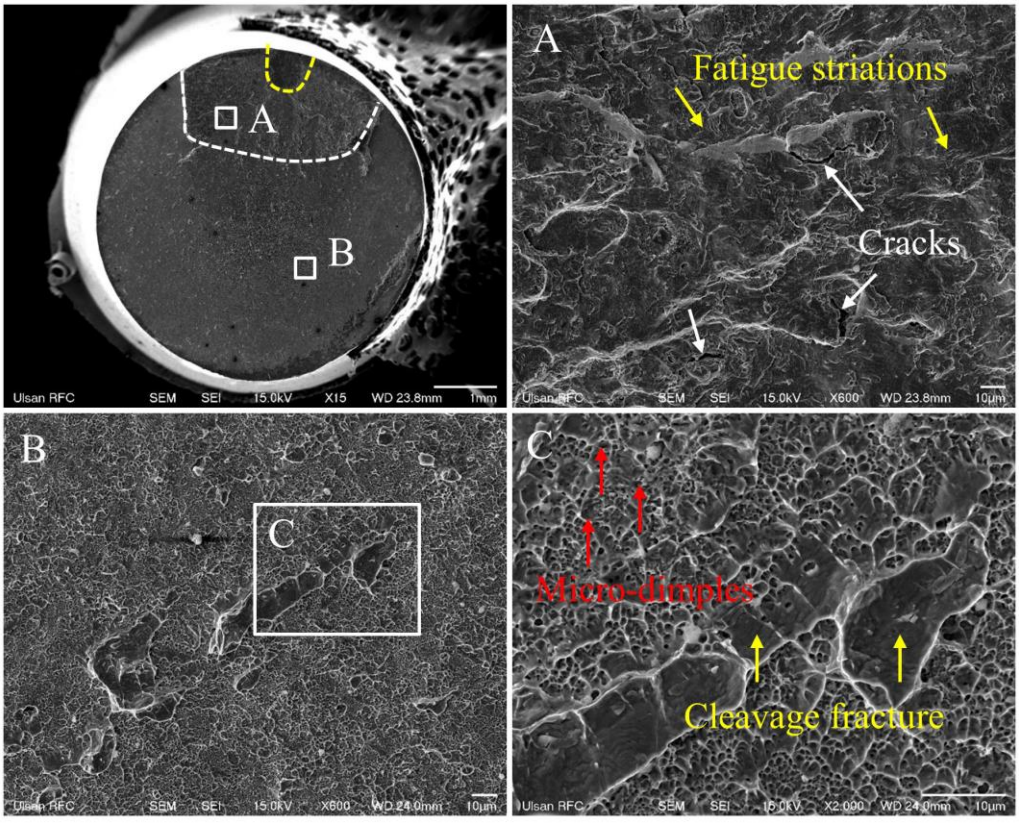

Fig. 6.20. Fracture appearance of the failed specimen under 567 MPa

6.4 CONCLUSIONS

In the present study, cylindrical SUS316L and SUS410 were solid state joined by electrically assisted pressure joining. It was determined by EDS line scan that the diffusion thickness could be significantly enhanced by increasing the electric current density up to a certain threshold value. Electric current density above the threshold does not further increase the diffusion to a greater extent. The microstructure analysis confirmed that the refined and equiaxed grains, including some amount of martensite grains, were generated by recrystallization during EAPJ as a combined result of large deformation, resistance heating, and athermal effects.

In the quasi-static tensile test, the interface fracture was changed to BM fracture with the increase of current density, which significantly increased the diffusion thickness. The different BM fracture modes can be explained by the competition of mechanical properties of the unaffected SUS410 BM and the heat-affected SUS316L. While the statistical analysis of the fatigue life was successfully conducted for the dissimilar EAPJ joints, the fracture appearance of the fatigue failure suggests that the fatigue behavior of the dissimilar EAPJ joint can vary significantly, depending on not only the property of the joint interface, but also the given cyclic stress level and the property of the heat-affected region near the joint interface. The result of the present study is expected to contribute to the development of an efficient solid-state joining process for dissimilar materials in structural applications.

REFERENCES

[1] K. Martinsen, S.J. Hu, B.E. Carlson, Joining of dissimilar materials, CIRP Annals, 64 (2015) 679-699.

[2] R. Casati, J. Lemke, M. Vedani, Microstructure and Fracture Behavior of 316L Austenitic Stainless Steel Produced by Selective Laser Melting, Journal of Materials Science & Technology, 32 (2016) 738-744.

[3] J. Zhang, Z. Liu, J. Sun, H. Zhao, Q. Shi, D. Ma, Microstructure and mechanical property of electropulsing tempered ultrafine grained 42CrMo steel, Materials Science and Engineering: A 782 (2020).

[4] B. Vamsi Krishna, A. Bandyopadhyay, Surface modification of AISI 410 stainless steel using laser engineered net shaping (LENSTM), Materials & Design 30(5) (2009) 1490-1496.

[5] S. Celik, I. Ersozlu, Investigation of the mechanical properties and microstructure of friction welded joints between AISI 4140 and AISI 1050 steels, Materials & Design, 30 (2009) 970-976.

[6] S. Mercan, S. Aydin, N. Özdemir, Effect of welding parameters on the fatigue properties of dissimilar AISI 2205–AISI 1020 joined by friction welding, International Journal of Fatigue, 81 (2015) 78-90.

[7] L. Peng, Z. Xu, X. Lai, An investigation of electrical-assisted solid-state welding/bonding process for thin metallic sheets: Experiments and modeling, Proceedings of the Institution of Mechanical Engineers, Part B: Journal of Engineering Manufacture, 228 (2013) 582-594.

[8] P. Eslami, A. Karimi Taheri, M. Zebardast, A Comparison Between Cold-Welded and Diffusion-Bonded Al/Cu Bimetallic Rods Produced by ECAE Process, Journal of Materials Engineering and Performance, 22 (2013) 3014-3023.

[9] A. Lilleby, Ø. Grong, H. Hemmer, Cold pressure welding of severely plastically deformed aluminium by divergent extrusion, Materials Science and Engineering: A, 527 (2010) 1351-1360.

[10] M. Pawlicki, T. Drenger, M. Pieszak, J. Borowski, Cold upset forging joining of ultra-fine-grained aluminium and copper, Journal of Materials Processing Technology, 223 (2015) 193-202.

[11] Z. Huang, J. Yanagimoto, Dissimilar joining of aluminum alloy and stainless steel thin sheets by thermally assisted plastic deformation, Journal of Materials Processing Technology, 225 (2015) 393-404.

[12] N. Bay, Mechanisms producing metallic bonds in cold welding, WELDING J., 62 (1983) 137.

[13] N.J. Peter, C. Gerlitzky, A. Altin, S. Wohletz, W. Krieger, T.H. Tran, C.H. Liebscher, C. Scheu, G. Dehm, P. Groche, A. Erbe, Atomic level bonding mechanism in steel/aluminum joints produced by cold pressure welding, Materialia, 7 (2019).

[14] H.-J. Jeong, J.-W. Park, K.J. Jeong, N.M. Hwang, S.-T. Hong, H.N. Han, Effect of Pulsed Electric Current on TRIP-Aided Steel, International Journal of Precision Engineering and Manufacturing-Green Technology 6(2) (2019) 315-327.

[15] M.-J. Kim, M.-G. Lee, K. Hariharan, S.-T. Hong, I.-S. Choi, D. Kim, K.H. Oh, H.N. Han, Electric current–assisted deformation behavior of Al-Mg-Si alloy under uniaxial tension, International Journal of Plasticity, 94 (2017) 148-170.

[16] J.-W. Park, H.-J. Jeong, S.-W. Jin, M.-J. Kim, K. Lee, J.J. Kim, S.-T. Hong, H.N. Han, Effect of electric current on recrystallization kinetics in interstitial free steel and AZ31 magnesium alloy. Materials Characterization 133 (2017) 70-76.

[17] H.-J. Jeong, M.-J. Kim, S.-J. Choi, J.-W. Park, H. Choi, V.-T. Luu, S.-T. Hong, H.N. Han, Microstructure reset-based self-healing method using sub-second electric pulsing for metallic materials. Applied Materials Today 20 (2020) 100755.

[18] M.-J. Kim, S. Yoon, S. Park, H.-J. Jeong, J.-W. Park, K. Kim, J. Jo, T. Heo, S.-T. Hong, S.H. Cho, Y.-K. Kwon, I.-S. Choi, M. Kim, H.N. Han, Elucidating the origin of electroplasticity in metallic materials, Applied Materials Today 21 (2020).

[19] S.-T. Hong, Y.-F. Li, J.-W. Park, H.N. Han, Effectiveness of electrically assisted solid-state pressure joining using an additive manufactured porous interlayer, CIRP Annals, 67 (2018) 297-300.

[20] Y.-F. Li, S.-T. Hong, H. Choi, H.N. Han, Solid-state dissimilar joining of stainless steel 316L and Inconel 718 alloys by electrically assisted pressure joining, Materials Characterization, 154 (2019) 161-168.

[21] S. Zhang, K. Gao, S.-T. Hong, H. Ahn, Y. Choi, S. Lee, H.N. Han, Electrically assisted solid state lap joining of dissimilar steel S45C and aluminum 6061-T6 alloy, Journal of Materials Research and Technology, 12 (2021) 271-282.

[22] Y. Kim, W. Hwang, Effect of weld seam orientation and welding process on fatigue fracture behaviors of HSLA steel weld joints, International Journal of Fatigue, 137 (2020).

[23] M. Wu, C. Wu, S. Gao, Effect of ultrasonic vibration on fatigue performance of AA 2024-T3 friction stir weld joints, Journal of Manufacturing Processes, 29 (2017) 85-95.

[24] S. Mohd, M.S. Bhuiyan, D. Nie, Y. Otsuka, Y. Mutoh, Fatigue strength scatter characteristics of JIS SUS630 stainless steel with duplex S–N curve, International Journal of Fatigue, 82 (2016) 371-378.

[25] H. Geng, L. Sun, G. Li, J. Cui, L. Huang, Z. Xu, Fatigue fracture properties of magnetic pulse welded dissimilar Al-Fe lap joints, International Journal of Fatigue, 121 (2019) 146-154.

[26] P.S. Effertz, V. Infante, L. Quintino, U. Suhuddin, S. Hanke, J.F. dos Santos, Fatigue life assessment of friction spot welded 7050-T76 aluminium alloy using Weibull distribution, International Journal of Fatigue, 87 (2016) 381-390.

[27] I.J. Davies, Unbiased estimation of the Weibull scale parameter using linear least squares analysis, Journal of the European Ceramic Society, 37 (2017) 2973-2981.

[28] R. Sakin, İ. Ay, Statistical analysis of bending fatigue life data using Weibull distribution in glass-fiber reinforced polyester composites, Materials & Design, 29 (2008) 1170-1181.

[29] S.-T. Hong, Y.-H. Jeong, M.N. Chowdhury, D.-M. Chun, M.-J. Kim, H.N. Han, Feasibility of electrically assisted progressive forging of aluminum 6061-T6 alloy, CIRP Annals, 64 (2015) 277-280.

[30] Y. Shi, M. Yuan, Z. Li, P. La, Two-step rolling and annealing makes nanoscale 316L austenite stainless steel with high ductility, Materials Science and Engineering: A, 759 (2019) 391-395.

[31] V. Tsisar, M. Kondo, T. Muroga, T. Nagasaka, I. Matushita, Morphological and compositional features of corrosion behavior of SUS410–SUS410, SUS316–SUS316 and SUS410–SUS316 TIG welded joints in Li, Fusion Engineering and Design, 87 (2012) 363-368.

[32] G. Chakraborty, C.R. Das, S.K. Albert, A.K. Bhaduri, V. Thomas Paul, G. Panneerselvam, A. Dasgupta, Study on tempering behaviour of AISI 410 stainless steel, Materials Characterization, 100 (2015) 81-87.

[33] M. Tsai, C. Chiou, J. Du, J.J.M.S. Yang, E. A, Phase transformation in AISI 410 stainless steel, 332 (2002) 1-10.

[34] S.Y. Anaman, S. Ansah, Y.-F. Li, H.-H. Cho, J.-S. Lee, H.N. Han, S.-T. Hong, Experimental and numerical studies on the electrochemical properties of an electrically assisted pressure joint of austenitic stainless steel and Ni-based superalloy, Materials Characterization, 165 (2020).

[35] M.F. McGuire, Stainless Steels for Design Engineers, ASM International, 2008, 162-166.

[36] M.-J. Kim, K. Lee, K.H. Oh, I.-S. Choi, H.-H. Yu, S.-T. Hong, H.N. Han, Electric current-induced annealing during uniaxial tension of aluminum alloy, Scripta Materialia, 75 (2014) 58-61.

[37] A.K. Pramanick, H. Das, J.-W. Lee, Y. Jung, H.-H. Cho, S.-T. Hong, M. Shome, A.K. Pramanick, Texture analysis and joint performance of laser-welded similar and dissimilar dual-phase and complex-phase ultra-high-strength steels, Materials Characterization, 174 (2021).

[38] A. Ramazani, P.T. Pinard, S. Richter, A. Schwedt, U. Prahl, Characterisation of microstructure and modelling of flow behaviour of bainite-aided dual-phase steel, Computational Materials Science, 80 (2013) 134-141.

[39] K. Radwański, Structural characterization of low-carbon multiphase steels merging advanced research methods with light optical microscopy, Archives of Civil and Mechanical Engineering, 16 (2016) 282-293.

[40] S.A.J. Jahromi, A. Khajeh, B. Mahmoudi, Effect of different pre-heat treatment processes on the hardness of AISI 410 martensitic stainless steels surface-treated using pulsed neodymium-doped yttrium aluminum garnet laser, Materials & Design, 34 (2012) 857-862.

CHAPTER VII

CONCLUSIONS

Electric pulse was applied to metallic materials to realize rapid heat treatment and damage healing of the fatigued ACS, which verified the advantages of the EAM technology in processing of laminated metal sheets. In EA rapid heat treatment, the intermetallic evolution and mechanical properties of the CRBed ACS sheet were significantly altered by EA rapid heat treatment. The results showed that an electric pulse can efficiently adjust the intermetallic compound, which in turn affects the strength and ductility of the ACS sheet, depending on the applied current density. The fracture modes of the matrix-dominated fracture and interfacial IMC-dominated fracture were determined based on observations from DIC tests and SEM fracture surfaces. The U-shape forming test confirmed that the desired formability can be achieved by properly designing the process parameters of the EA rapid heat treatment, rather than simply using a higher current density. Also, the fatigue life of the ACS sheet was significantly prolonged by applying an electric pulse with subsecond duration. The significantly prolonged fatigue life is found to be the result of a combination of diminished dislocation density and retardation of microcrack formation. The present investigation on the laminated ACS sheet with a subsecond duration proved that electropulsing treatment is an effective method to prolong the fatigue life of the ACS sheet and balance the strength and ductility of the ACS sheet.

Additionally, solid-state joints of various combinations of dissimilar metal alloys, S45C and Al661-T6, additively manufactured AMMS1 and conventional SUS410, and SUS316L and SUS410, are successfully fabricated by EAPJ technique. In lap joining of

dissimilar steel S45C and aluminum 6061-T6 alloy, it clearly confirmed the feasibility of EAPJ for the selected dissimilar combination of S45C and Al6061-T6 and be expected to contribute to the development of cost-effective and energy-efficient solid state joining processes for steel and aluminum alloys. In the meantime, EAPJ of AMed MS1 and conventional SUS410 clearly demonstrates the benefits of using a porous layer during EAPJ of a dissimilar material combination. First, the temperature can be more effectively and locally controlled, thus the material flow can be more properly controlled at the expected local area to achieve more asymmetric deformation with respect to the interface. The control of material flow is especially crucial in solid-state joining of a dissimilar material combination with highly different mechanical properties. Additionally, the joining load can be dramatically decreased, which reduces the required capacity of the joining facility in practical applications. Finally, the fatigue performance for the material combination of SUS316L and SUS410 joints, it is evaluated by a P-S-N curve using two-parameter Weibull distribution. The present study demonstrates that EAPJ is an efficient method in bulk and lap joining of dissimilar metal alloys combinations.